1) A PROOF-OF-CONCEPT EXPERIMENT TO INVESTIGATE FAST CHARGING TRANSIENTS BY SCANNING KELVIN PROBE MICROSCOPY AND 2) STUDIES ON BRIDGED RUTHENIUM COMPLEXES

A Dissertation

Presented to the Faculty of the Graduate School

of Cornell University

in Partial Fulfillment of the Requirements for the Degree of

Doctor of Philosophy

by

Sarah Ruth Nathan

May 2018

1) A PROOF-OF-CONCEPT EXPERIMENT TO INVESTIGATE FAST CHARGING TRANSIENTS BY SCANNING KELVIN PROBE MICROSCOPY AND 2) STUDIES ON BRIDGED RUTHENIUM COMPLEXES

Sarah Ruth Nathan, Ph.D.

Cornell University 2018

Scanning kelvin probe microscopy has been to used to understand the operation of, and optimize the performance of both organic and inorganic photovolataic materials on the 10's of nm scale. Most studies have only examined the spatial distribution of the electronic phenomena – including potential, photopotential, capacitance, photocapacitance, current, and photocurrent – however, there is much to be learned by measuring and mapping the time-dependence of these characteristics. In organic bulk heterojunction solar cells, Ginger and coworkers have shown by time-resolved electrostatic force microscopy (tr-EFM) that the microscopic photocapacitance charging rate in a film is directly proportional to the external quantum efficiency (EQE) of a photovoltaic device. Transients with sub-microsecond time resolution have been collected, but acquiring these transients required long signal-averaging times. Building on the previous work of Moore, Marohn, and co-workers, we developed a method to rapidly acquire transients of capacitance, frequency and phase indirectly, in a stepped-time, stepped-voltage experiment, by encoding and measuring the capacitance as a change in the phase of a vibrating cantilever. In a proof-of-concept experiment we show that this new method is viable for observing transients down to 100 μsec. This approach represents an exciting new route to understanding geminate recombination in photovoltaic materials.

Mitochondrial calcium plays a critical role in regulating cell survival, apoptotic pathways, and cellular energetics. Acute overload of mitochondrial calcium will induce cell death and

is implicated in the damage caused by lethal reperfusion injury. Inhibitors of mitochondrial calcium uptake minimize the harm caused by such conditions. The most well characterized mitochondrial calcium uptake inhibitor is Ru360, a μ-oxo-bridged dinuclear ruthenium complex. Its synthesis and purification is challenged by extremely low yielding reactions and purification by tedious cation exchange chromatography. Furthermore, this compound is not cell permeable, a feature that significantly limits its biological use. With the goal of preparing potent mitochondrial calcium uptake inhibitors that are biologically available, we investigated the synthesis and characterization of six dinuclear ruthenium species. One complex is a structural analog of Ru360, and five are structurally similar dinuclear ruthenium μ-nitrido complexes. These compounds were characterized by NMR spectroscopy, EPR spectroscopy, UV-vis spectroscopy, infrared spectroscopy, cyclic voltammetry, conductivity, and small-molecule crystallography. Mitochondrial calcium uptake inhibitory activity in permeabilized and unpermeabilized cells are described. Cellular uptake of the complexes and cytotoxicity are presented and discussed in the context of molecular structure. One of these complexes shows 10$\times$ better MCU-inhibitory activity, low cytotoxicity, and enhanced cellular uptake compared to Ru360.

BIOGRAPHICAL SKETCH

Sarah Ruth Nathan was born on March 10, 1989 at home in a small North Carolinian town. At age two, Sarah, her brother and her parents moved across the country to Hailey, Idaho. Sarah was homeschooled and received her high school equivalency certificate from the State of Idaho in 2007. Her interest in science began with the desire to become of a medical physician and her parents' encouragement to learn and study. One day in the local college's bookstore a very detailed periodic table sparked Sarah's interest in chemistry and she decided to pursue that as her major in college. Sarah also was very involved in music growing up, taking violin lessons until she was 10 and then piano lessons. On May 5, 2007 she showcased her work a one hour senior recital.

Sarah went to Idaho State University in Pocatello, Idaho, to study chemistry and prepare for applying to medical school. She also took a number of music classes and continued with piano lessons for several years. In the fall semester of her sophomore year, she started doing research for Professor Joshua Pak, investigating the synthesis of organic ligands used for dye sensitized solar cells. After a year, she switched to the laboratory of Professor Byron Bennett, looking at the synthesis of bipyridine and pyridine ligands for platinum-based anticancer agents. During a summer internship after her junior year at the University of Massachusetts medical school in Worchester, MA, Sarah discovered her passion lay in chemical research, not biomedical research. After the internship, she focused on her studies in chemistry with the plan of entering graduate school; during this time she also decided to double major in biochemistry. Sarah graduated with high honors on May 5, 2012 with a Bachelor of Science in Chemistry and Biochemistry. During her time at Idaho State she was a member of the Sigma Xi research society, Golden Key honor society, American Chemical Society, and was the treasurer of the Idaho State University Gamma Beta Phi honor society.

Sarah began her graduate studies at Cornell University in August 2012 and joined the lab of John Marohn that fall. She was awarded the National Science Foundation Graduate

Research Fellowship that supported her research from Fall 2013 to Fall 2016. Sarah passed her PhD candidacy exam on August 22, 2014. After this time studying physical chemistry and instrumental experiment development, Sarah wanted to return to bench chemistry, and focus more on the synthesis and characterization of interesting materials. She joined the lab of Justin Wilson and began working on ruthenium complexes as potential heart-attack therapeutics. At Sarah's first international conference, the 2014 Gordon Research Conference on Hybrid Electronic Photonic Materials and Phenomena in Hong Kong, she presented a poster on her research in the Marohn group and earned an outstanding poster award. Sarah then went on to give multiple poster and oral presentations, the latest being an oral presentation at the August 2017 American Chemical Society meeting in Washington DC, receiving the Division of Inorganic Chemistry travel award to attend the conference. Sarah plans to continue to pursue her passion for chemical research and studying interesting scientific questions.

...may my mind stroll about hungry

and fearless and thirsty and supple

and even if it's sunday may i be wrong

for whenever men are right they are not young...[1]

[1] e.e. cummings

ACKNOWLEDGEMENTS

Funding

Many thanks to the National Science Foundation Graduate Research Fellowship program for support (#DGE-1650441). Additional thanks to the National Science Foundation for research funding (#DMR-1309540) and the Cornell Center for Materials Research facilities, supported by the National Science Foundation (#DMR-1120296).

Professional

First, many thanks to my advisors, Professor John A. Marohn and Professor Justin J. Wilson. You have both have taught me an incredible amount, not only raw information, but also how to interpret and utilize that information. It is difficult to parse what contribution can be attributed to whom. Without the support of both I would not be the scientist, writer, communicator, analyst or person I am today.

Professor John Marohn has an amazing group to work with. Louisa, thank you for teaching me so much and for always being patient and understanding. Ryan, I will always be impressed by your ability to understand theory and to explain it, thank you. You took my project further than I ever could have. Thank you to everyone else who listened to me and answered questions.

Professor Justin Wilson built a wonderful group and will continue to inspire many graduate students. Josh, I know you'll do amazing; good luck with osmium and thanks for many excellent conversations. Jesse, best of luck with this project. I hope it goes smoother for you than it did for me. Thank you to Jazmin, Nick, Julie and Santiago; I learned how to be a mentor and I hope you learned something about research from me. Thanks to everyone else, thanks for making this group a fun and inspiring workplace - don't forget to keep it that way.

Thanks to Brandon Wenning and Pamela Nasr for helping me make samples to put in the

microscope. Many thanks to Daniela Arduino in the lab of Professor Fabiana Perocchi for testing all the different compounds I sent her. Many thanks to Santhanam Shanmughapriya and Neeharika Nemani in the group of Professor Madesh Muniswamy for performing a variety of biological assays on my complexes. Of course, a huge thank you Dr. Samantha MacMillan for figuring out all my crystal structures, teaching me about crystallography and generally listening to me when I needed an ear to bend. Thank you to Dr. David Holowka for helping me with the fluorescence assays and Boris Dzikovski for helping me run and analyze my EPR spectra.

Thanks to my first committee members, Professor David Muller and Professor Tobias Hanrath for their time and suggestions at my A-exam. Many thanks to Professor Kyle Lancaster for being on my committee with John and Justin.

Personal

I'd like to first thank my family for their continued and unquestioning support. I would not be a chemist today if my parents had not encouraged me learn and explore the world around me. Thanks to my brother Paul for helping me dissect old computer code and listening to me even though you know very little about chemistry and for all the fascinating discussions. I look forward to more. Many warm thanks to my friends who have supported me and stood by me. There isn't enough space to thank all of you by name. Michelle, you're my longest friend and I know we always will be friends. You have always inspired and challenged me and probably always will. Estella, thank you for sending silly stickers, always being there when I needed you and when I didn't. Beth, you're a wonderful hiking partner and an amazing friend. I look forward to future backpacking trips. Kristina, Steve, Jenny, Johan and everyone else, thank you for always supporting and encouraging and challenging me in everything.

TABLE OF CONTENTS

LIST OF TABLES

LIST OF FIGURES

CHAPTER 1

PROOF-OF-CONCEPT EXPERIMENTS ON MICROSECOND CHARGING TRANSIENTS VIA SCANNING KELVIN PROBE MICROSCOPY

1.1 Introduction

When a solar cell is irradiated, charge is generated and thus electrical current. The dynamics of charge generation is a subject of ongoing research to new photovoltaic materials. The motivation for this work is to couple the high spatial resolution of scanned probe microscopy with local temporal information to understand the spatially-dependent dynamics of a solar-cell material. The focus for this discussion is organic-based photovoltaics, however temporal related studies of materials are universally relevant.

Organic-based photovoltaics use conjugated small molecules and polymers to convert photons into free charges. The blend of two or more polymers will form a bulk heterojunction (BHJ) film.[1–4] One of the polymers acts an electron donor, or n-type material, while the other is the electron acceptor, or p-type material; the interface of the two materials forms a junction at which charge is generated.[5–7] In general even simple blended systems are advantageous because they have a many junctions, and can easily be prepared and studied.[1,8–12] Organic-based photovoltaic systems are useful because their properties can be tuned *via* a plethora of synthetic and processing methods.[13] These types of solar cells have developed significantly over recent years, with the highest efficiency device to date reported at 11-12%, compared to crystalline silicon at 28%.[14–16] A variety of factors can affect device performance including composition, polymer molecular weight, thickness, and annealing.[17–26] In contrast to silicon solar cells that produce charge immediately upon irradiation, light absorption in organic photovoltaics forms neutral excitons. Upon migration to a junction, the exciton splits into an electron and hole.[10,13,27] Any recombination between the electrons and holes, as well

as the mobility of the exciton and the generated charges, will affect the overall efficiency of the device. Additionally, the aforementioned factors will also affect these microscopic phenomena.[9,25,26,28–30]

Upon photogeneration of excitons and thus charge carriers in a film (or device), several fates are possible. The charges can be "trapped", effectively not going anywhere for a time; they can diffuse and be extracted; or they can recombine producing heat or light.[13] Recombination represents, effectively, nonproductive work; typical time constants range for recombination in the hundreds of nanoseconds to microseconds.[30–33] The rate at which these processes happen is highly variable, largely dependent on device composition.[9,25,34–37] Many devices have an almost 100% internal quantum efficiency, or how well the incident photons produce charge (photon-to-charge-carrier yield). However, these devices often have an extremely low power-conversion efficiencies.[38,39] This dichotomy is puzzling as it reveals that a number of the charges produced are not contributing to device current. Understanding the fate of the generated excitons, electrons, and holes will provide information about the physical mechanisms controlling device efficacies. Thus, studies of the dynamics of these systems on the nanosecond to microsecond time scale, with high spatial resolution, will provide understanding to the governing limitations and processes.

To assess phenomena such as charge carrier generation, mobility, and recombination, in the time-domain a variety of time-dependent instrumental techniques have been developed, including transient absorption spectroscopy, time-resolved photoluminescence and time-resolved microwave conductivity.[13] Briefly, transient absorption spectroscopy probes the absorption of photons over time in a thin film. The change in absorption is stimulated by an ultrafast laser and measured over time. This technique has a wide temporal range, with examples ranging from picoseconds to microseconds.[25,27,28,30,34,40–43] The observed time-dependent absorption spectrum provides information about crystallinity, annealing effects,

photogeneration, and recombination. However, the technique is not spatially resolved and spectral features can be complicated by overlapping absorption bands.[27] Time-resolved photoluminescence tracks the decay in luminescence after stimulation of the sample with a laser pulse. Typically this technique probes time scales between picoseconds to nanoseconds.[29,37,44] The decay is generally associated with the radiative decay of charge-transfer states within an organic polymer film.[4,9,29,37,45–48] While photoluminescence measurements can be spatially resolved, scanned probe microscopy has ∼100-fold better spatial resolution.[49–55] Time-resolved microwave conductivity (TRMC) has been used to study trapping and recombination in photoactive samples in the nanosecond to second time regime.[16,35,36,44,56] The formation of charge-transfer excitons in these films typically occurs on the femtosecond time scale, however charge generation, recombination, and trapping and detrapping times are orders of magnitude slower and more directly effect device performance. Microwave conductivity, as a general technique, measures the mobility of charges in a sample (specifically the free carriers' mobility-charge density product). As mobile charges are generated they interact with the electric field of the incident microwaves.[16,57] The resulting change in transmitted or reflected power reveals information about the nature of the charges and their lifetimes. However, the technique cannot distinguish between positive and negative charges and no spatial information can be obtained.

Scanning Kelvin probe force microscopy (SKPFM), or electrostatic force microscopy (EFM), is a scanned probe technique similar to atomic force microscopy (AFM); it measures the forces between charges (for EFM) within the sample and a charged microcantilever rather than the neutral van der Waals forces (for AFM) between two close objects.[58–64] It can be used to measure the surface potential of a material, to visualize trapped charge locations, or to investigate the kinetics of charging or trapping on a surface[65,66]. EFM/SKPFM[1] provides a method to visualize charge at high spatial resolution – 10s of nanometers.[66] Time-resolved

[1]For the rest of this discussion EFM will be used for simplicity

EFM has been explored, but only in a limited sense. One report used photoluminescence to show the photogenerated exciton in highly-ordered closely-linked quantum dot arrays was quenched on the nanosecond time regime; EFM indicated that free charge was still present for seconds.[67] Application of time-resolved EFM to a polymer blend photovoltaic showed that the *rate* of charging in a film prepared without a top contact correlated well with the device external quantum efficiency (the ratio of charge carriers produced to photons absorbed in a complete device), as well as overall device efficiency.[68] These experiments tracked the photo-induced change in the cantilever frequency and obtained millisecond time resolution. Further experiments increased the time resolution down to ∼100 nanoseconds, where directly tracking the frequency change required a high number of scan averages.[69,70] A 2D scan of a polymer blend films showed, on average, a sub-30 microsecond charging rate with generally high spatial uniformity. This method is slow, and is limited by the inverse relationship between time resolution and photodetector bandwidth ($t_r = 1/bw$), thus requiring excessive averaging times, as explained below ($\sim$ 14 h for single nanosecond resolution). Other types of KPFM methods have been used to measure change down to the picosecond time regime, however these exploit the nonlinear dependence of the photovoltage on light intensity and or the cantilever frequency.[71–75] However, these methods are less applicable to organic donor acceptor blends as the photocapacitance between the tip and the sample is *linearly* dependent on the light intensity.[76] We propose to utilize an alternative method to determine rate of charge carrier generation on the microseconds time scale with high spatial resolution and low signal averaging times using EFM.

1.2 Theory

In EFM, an extremely sensitive oscillating cantilever is brought close to the sample surface with a bias applied to the tip or the sample (Figure 1.1). The oscillating microcantilever

can be modeled as a damped driven harmonic oscillator with a corresponding frequency, phase, and amplitude. Over a surface, the tip and sample charge to first approximation can be modeled as a parallel plate capacitor. Corrections for the conical shape are possible if a more exact tip-charge estimate is desired.[77–79]

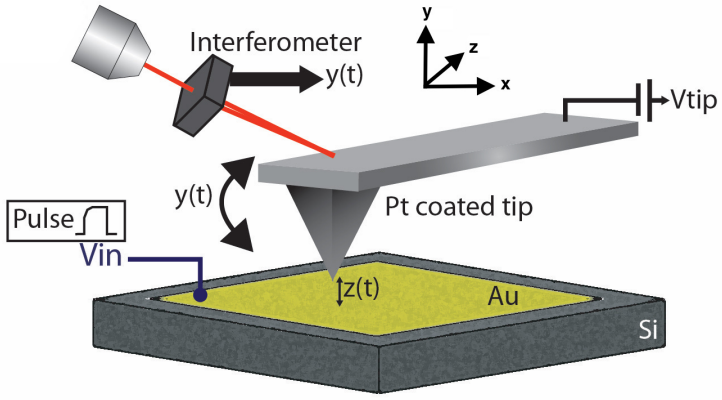

Figure 1.1: Setup for time-resolved electrostatic force microscopy over a simple gold sample.

A perturbation in the interaction between the oscillating cantilever and the sample will subsequently result in a change in the phase and frequency of the cantilever oscillation (Figure 1.2).[58,63,68,69] Any change in the sample charge will produce a change in the tip-sample capacitance, as well as the first and second height derivative of this capacitance (Equation 1.1). The frequency (f) can be related to the cantilever tip voltage (V_{tip}), the unperturbed cantilever frequency (f_0), the cantilever spring constant (k), the surface potential of the sample ($\phi(x)$) and the capacitance second height derivative (C'').[63,79]

$$f(V) \simeq f_0 - \frac{f_0}{4k} C''(V_{\text{tip}} - \phi(x))^2 \tag{1.1}$$

The resulting frequency shift of the cantilever is related to the charge dynamics in the sample: a time-dependent change in the charge state of the sample or tip (C'', V_{tip} or $\phi(x)$) will change the time-dependent cantilever frequency. The cantilever oscillation traces out a sine wave; the instantaneous frequency and phase can be determined via mathematical

demodulation of the displacement *versus* time data.[80] The steady-state motion of a driven, oscillating cantilever has the form

$$y(t) = A\sin(\phi(t)). \tag{1.2}$$

Demodulation of the cantilever position oscillation data will yield the time dependent phase, $\phi(t)$, frequency, $f(t)$ and amplitude, $A(t)$. Experimentally, the position y is measured versus time, t. Via signal demodulation, a signal processing method of finding the phase and frequency from the analytic signal, *z(t)*, the desired A, ϕ, and f can be found as a function of time. The analytic signal is defined as

$$z(t) = y(t) + iH[y(t)] \tag{1.3a}$$

$$= a(t)e^{i\phi(t)} \tag{1.3b}$$

where $H[y(t)]$ is the Hilbert transform, and *a(t)* is the time dependent amplitude.[81,82] Therefore, the amplitude is the argument of $z(t)$ and the phase is the angle of $z(t)$ (Equation 1.3b).[80] Functionally, this process is done by (1) taking the Fourier transform of the position data and baseline correcting it, (2) inverting the negative frequency components in the Fourier domain, (3) adding (1) and (2) together to effectively zero the negative frequency portions and double the positive frequency components, and (4) taking the inverse Fourier transform, revealing the time-dependent phase and time-dependent amplitude.[81,82] The frequency is defined as the time derivative of phase and thus can be calculated as follows:

$$\phi(t) = 2\pi \int_0^t f(t')dt' + \phi_0. \tag{1.4a}$$

$$f(t) = \frac{1}{2\pi}\frac{\partial\phi}{\partial t} \tag{1.4b}$$

As such, the area under a time-dependent frequency trace is equivalent to the phase. If the change in photocapacitane is controlled by a time constant (τ), then the frequency and

phase must also contain that same information. Using

$$f = \Delta f e^{-t/\tau}$$

as an example for the frequency we obtain

$$\phi = 2\pi\Delta f\tau(1 - e^{-t/\tau})$$

via equation 1.4b.[68,69] We seen then that τ, the the photocapacitance lifetime associated with a single process, can be determined from the phase or the frequency.

Determining τ via a phase or frequency transient will produce identical values, however the experimental noise will be different. The main contributors for cantilever noise at low frequencies (<100 Hz) is thermal noise and at high frequencies (>1000 Hz) is detector noise.[81] The detector noise increases quadratically with frequency. Consequently fast time experiment (which incorporate noise covering a large bandwidth) will inherently have a lot of noise. The application of a filter will reduce noise levels, however, the associated filter bandwidth (bw) will stipulate the time resolution (t_r) (bw = $1/t_\mathrm{r}$). Therefore the analysis of data on short time scales will require very large bandwidths: for example, microsecond time resolution will require a bandwidth of 1 MHz. To determine how the frequency noise scales with bandwidth we look at the power spectrum of position fluctuations ($P_{\delta x}^{\mathrm{det}}$) and the power spectrum of frequency fluctuations ($P_{\delta f}(f)$), starting with the rms position ($\delta x_{\mathrm{rms}}^2$). Integrating across frequency determines the rms frequency noise.

$$P_{\delta f}(f) \backsimeq \frac{P_{\delta x}^{\mathrm{det}}}{x_{\mathrm{rms}}^2} f^2 \tag{1.5a}$$

$$\delta f_{\mathrm{rms}}^2 = \int_{-\mathrm{bw}}^{\mathrm{bw}} \frac{P_{\delta x}^{\mathrm{det}}}{x_{\mathrm{rms}}^2} f^2 df \tag{1.5b}$$

$$\Rightarrow \delta f_{\mathrm{rms}}^2 = \frac{P_{\delta x}^{\mathrm{det}}}{x_{\mathrm{rms}}^2} \frac{1}{12} \mathrm{bw}^3 \tag{1.5c}$$

$$\therefore \delta f_{\mathrm{rms}} \sim \mathrm{bw}^{3/2} \tag{1.5d}$$

The rms frequency noise has a 3/2 power dependence on the bandwidth and thus a 3/2 power dependence on the time resolution. In comparison, the bandwidth dependence on the phase noise is significantly less. An analogous integration gives the rms phase noise.

$$P_{\delta\phi}(f) = \frac{P_{\delta f}(f)}{x_{\mathrm{rms}}^2} \tag{1.6a}$$

$$\delta\phi_{\mathrm{rms}}^2 = 2\pi \int_{-\mathrm{bw}}^{\mathrm{bw}} \frac{P_{\delta x}^{\mathrm{det}}}{x_{\mathrm{rms}}^2} df \tag{1.6b}$$

$$\Rightarrow \delta\phi_{\mathrm{rms}}^2 = 4\pi \frac{P_{\delta x}^{\mathrm{det}}}{x_{\mathrm{rms}}^2} \mathrm{bw} \tag{1.6c}$$

$$\therefore \delta\phi_{\mathrm{rms}} \sim \mathrm{bw}^{1/2} \tag{1.6d}$$

This analysis reveals that the rms phase noise has only a square root dependence on the bandwidth instead of a 3/2 dependence, thus a 1/2 power dependence on time resolution.

The common solution to the high frequency noise problem is signal averaging for frustratingly long times. However, by converting the photocapacitance transient experiment to a phase measurement we can exploit the noise difference and obtain more time resolution with less signal averaging.[69,83] The change in sample capacitance upon photoirradiation can be modeled as an exponential rise and decay (instead of a single τ as illustrated above), with time constants associated with each portion (τ_{r} and τ_{d}, respectively), (Figure 1.2a). According to Equation 1.1, the change in frequency will also rise and decay; the rate of photo-capacitance change can be measured by tracking the cantilever frequency shift over an illuminated sample (Figure 1.2b). The frequency will track with the capacitance linearly in the experiment, with both τ_{r} and τ_{d} accessible. However considering both of these simultaneously is more complex as the generation of charge (exciton splitting) most likely does not occur at the same rate as de-charging (recombination, trapping). To access only a single time constant, only the frequency shift for the rise (or decay) is desired. This selection can be done by applying a voltage to the cantilever tip: the frequency shift can be returned to zero (Equation 1.7, Figure 1.2c). By varying the length of time (t_p) the cantilever tip is biased, the length of time the frequency shift evolves can be varied in a systematic way.

The photo-induced of the frequency transient effectively causes a shift in the cantilever phase, where the shift is equal to $\Delta\phi$ (Figure 1.2d). By varying the voltage pulse time (t_p), we vary the length of time that frequency transient occurs and therefore also the size of the phase shift ($\Delta\phi$). Integrating each portion of the frequency transient, equation 1.7, and adding the two pieces together produces an equation for the phase shift which depends on τ_r, pulse time (t_p) and the steady state frequency shift (δf_{ss}) (Equation 1.8). The steady state frequency shift is equal to the maximum shift when the transient rises to its steady state value.

$$f(t) = \delta f_{ss} \begin{cases} 1 - e^{-t/\tau_r} & t \in (0, t_p) \\ 0 & t \in (t_p, \infty) \end{cases} \tag{1.7}$$

$$\Delta\phi = \delta f_{ss}((e^{-t_p/\tau_r} - 1)\tau + t_p) \tag{1.8}$$

In equation 1.8 at short times the exponential term dominates, while at long times the linear term dominates.

1.3 Methods

All experiments were performed under vacuum (8×10^{-7} mbar) in a custom-built scanning Kelvin probe microscope.[59] The cantilever (MikroMasch HQ:NSC18/Pt conductive probe) had resonance frequency $f_0 = 62{,}000$ kHz, spring constant $k_0 = 6.9$ N m^{-1}, and quality factor $Q = 32{,}000$. Cantilever motion was detected using a fiber interferometer operating at 1310 nm (Corning SMF-28 fiber). The laser diode's (QPhotonics laser diode QFLD1490-1490-5S) dc current was set using a precision current source (ILX Lightwave LDX-3620), and the current was modulated at radio frequencies using the input on the laser diode mount (ILX Lightwave LDM 4984, temperature-controlled with ILX Lightwave LDT-5910B).[84] The interferometer light was detected with a 200-kHz bandwidth photodetector (New Focus model

2011, built-in high-pass filter set to 300 Hz) and digitized at 1.25 MHz (National Instruments, PCI-6259). The cantilever was driven using a commercial PLL cantilever controller (RHK Technology, PLLPro2 Universal AFM controller), with PLL loop bandwidth of 1.2 kHz (PLL feedback loop integral gain I = 2.5 Hz^{-1}, proportional gain P = -12°/Hz).

At the beginning of the experiment the cantilever tip was biased at 6 V, to achieve linearity between the frequency shift and applied voltage.[63] The frequency shift is dependent on the capacitance change (Figure 1.2a, Equation 1.1). For a proof-of-concept experiment, instead of illuminating a photoactive sample, a single voltage pulse of known duration and shape following Equation 1.7 was applied to a 200 nm gold sample on silicon [2] (240 nm tip-sample height). The cantilever tip remained biased through the whole experiment to achieve the desired linear relationship between the size of the voltage pulse and the frequency shift. The voltage pulse was stepped (t_{pulse}) as shown in Figure 1.2c. The data acquisition was triggered on a rising zero crossing of the cantilever oscillation using the square wave copy of the cantilever signal. After acquiring 50 ms of data, a voltage pulse was triggered, starting on the rising edge of the square wave copy of the cantilever signal. The voltage pulse was returned to zero after the transient developed for t_{pulse} (Figure 1.2b, Equation 1.7). The experiment was then repeated while varying the time that the frequency (and thus phase) shift accumulates. The data was processed in Python using the demodulation scheme outlined above. The demodulation bandwidth was set at the minimum possible as to not introduce unnecessary noise. For example, for a one millisecond time constant, a bandwidth of one kilohertz was used. The filter utilized was based on the Blackman filter with minor modifications:

$$b(n) = 0.42 - 0.50\cos(\frac{2\pi n}{\text{bw}}) + 0.08\cos(\frac{4\pi n}{\text{bw}}). \tag{1.9}$$

The edges of the filter were set to zero to ensure that no artifacts were introduced.

[2] Thanks to Pamela Nasr for preparing the samples.

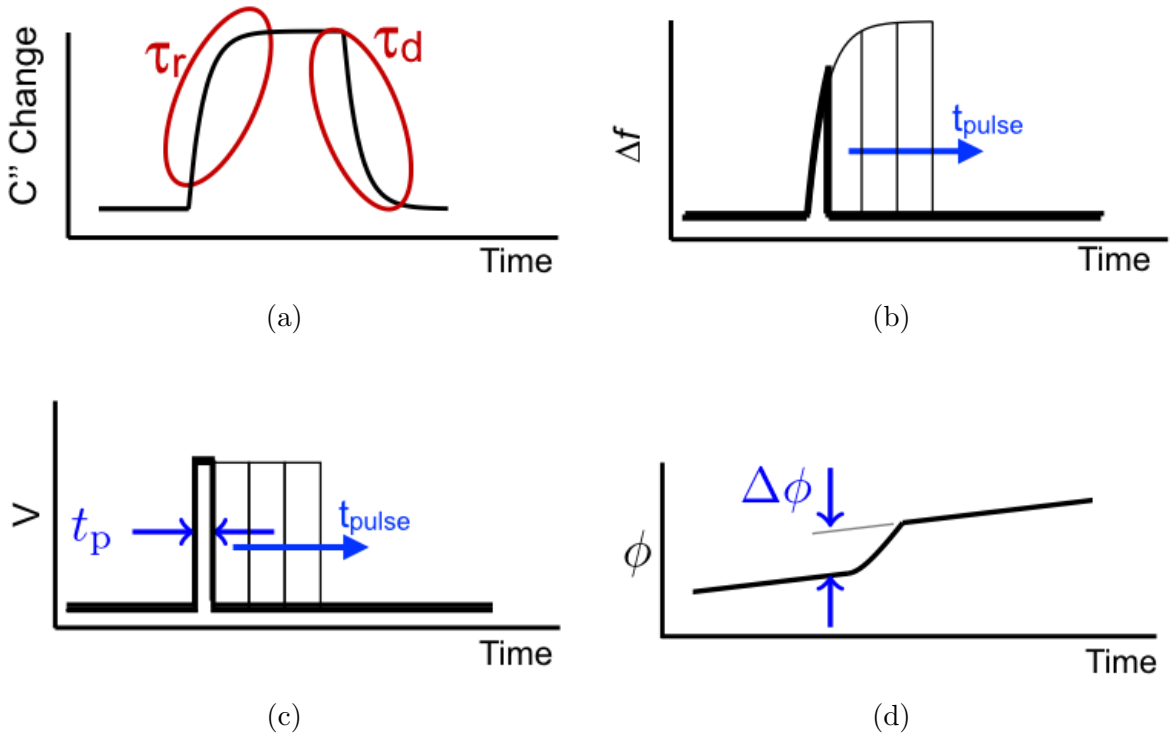

Figure 1.2: (a) The model of the second derivative of the cantilever rising and decaying with different time constants. (b) The frequency change observed as the result of multiplying the tip voltage (c) and the modeled capacitive change (a). (c) The modulation of the tip voltage to access each piece of the changing capacitive. (d) The phase jump associated with a single frequency trace, equivalent to the area under the frequency transient. As the tip voltage is stepped in time, the frequency transient increases, and the phase jump also increases.

.

To determine $\Delta\phi$, five milliseconds of the phase data was fitted directly before and after after the pulse. The experiment was repeated sixteen times for each pulse time, with a total of ten milliseconds of data for the workup of each pulse. The linear portions are extrapolated to a common time and the phase shift difference determined (Figure 1.2d). The phase shift will be different for each pulse length and will follow equation 1.8. The trace of phase shift versus pulse time was then fitted to determine τ_r. The data was fitted using MagicPlot Pro v. 2.7.2.

1.4 Results and discussion

The phase shift exhibited a sub-linear dependence on pulse time, as expected from equation 1.8. At short times the exponential portion could be observed while at longer times the rise was largely linear. Fitting successfully obtained the known time constant τ_r of the applied voltage pulse (Table 1.1, Figure 1.3). In each case the applied transient could be redetermined from the fit, within 2σ error bars. A ringing in the phase was observed after the phase shift with an oscillating frequency of 400 Hz, equal to the bandwidth of the positive feedback circuit used to drive the cantilever; while not applied to this experiment, turning off the cantilever drive just before the voltage pulse would remove this artifact.[76] A slow oscillation could be seen in the 800 μsec data (Figure 1.3d); this is attributed to slow drifting in the phase over the time span of the voltage pulse. Removing the last (longest t_p) five data points greatly improves the fit of the data (see 800^b entry).

Applied τ_r (μsec)	Calculated τ_r (μsec)	δf_{ss} (Hz)
100	73 ± 35	0.56 ± 0.017
250	282 ± 34.0	0.50 ± 0.0066
400	429 ± 78.0	0.25 ± 0.0054
800[a]	715 ± 85.0	0.31 ± 0.0037
800[b]	811 ± 57.0 (1σ)	0.33 ± 0.0063

Table 1.1: The fitted results for δf_{ss} and τ compared to the τ of the voltage applied. For 800 μsec, the removal of the last five data points greatly enhanced the quality of the fit.

The theory derived here assumes the sample is is evolving only under a single time constant, although the same experiment could be performed with a biexponential capacitance.[76] This analysis may be more realistic to donor-acceptor blend dynamics, as they frequently show complex time evolution.

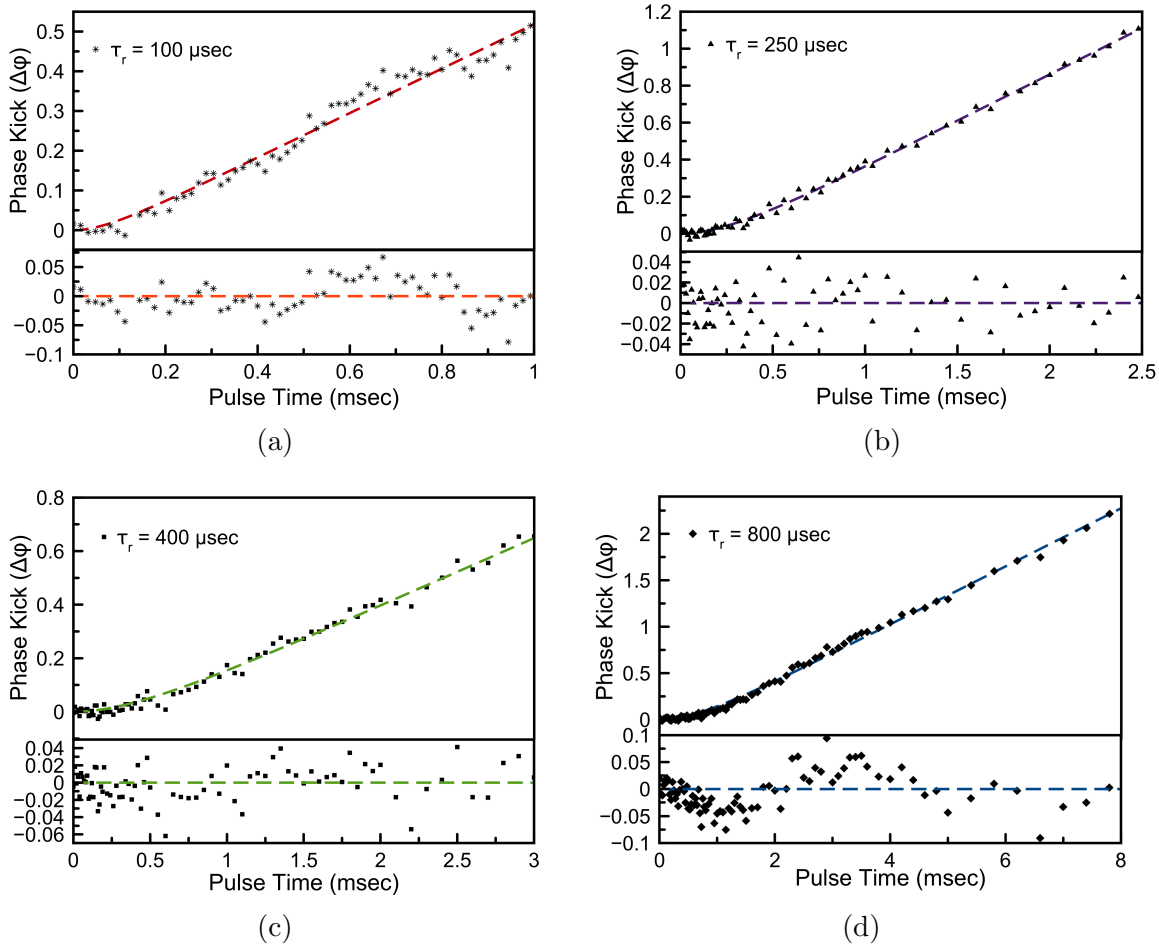

Figure 1.3: Raw data with fits (Table 1.1) for four different applied time constants with residuals shown for each.

1.5 Conclusion

A proven way to observe capacitance transients in a sample is by tracking the frequency shift of a cantilever in real time. However, this method introduces increasing amounts of noise with increasingly fast transients. By exploiting the inherent relationship between frequency and phase it is possible to observe the net effect of a capacitance transient on a sample in cantilever phase. The new method does not rely on watching the transient in real time, as

with frequency, but instead is observed after the transient has occurred. By stepping the length of time the cantilever voltage is applied to the tip the "amount" of frequency transient evolved is also stepped. This resulting frequency step is associated with corresponding shift in the phase containing the same information as the frequency transient. As the length of the tip voltage is moved forward the phase transient is measured. Thus, the frequency transient is also determined.

As a proof-of-concept experiment voltage pulses were applied to a conductive sample to induce a frequency shift and phase jump in an oscillating microcantilever. The voltage pulses contained an exponential rise; the relationship between the time length of the pulse, t_p and the phase jump, $\Delta\phi$, was derived. For each $\Delta\phi$ vs t_p plot the time constant (τ_r) was determined to be within error of what was applied. Further experiments employed the phase-kick technique introduced here to model donor/acceptor blends, as well as exploring the time resolution limits of the technique.[76]

CHAPTER 2

INTRODUCTION TO MITOCHONDRIAL CALCIUM AND INHIBITORS

2.1 Mitochondrial calcium

Calcium (Ca^{2+}) is a critical ion that regulates cellular homeostasis by mediating cellular signaling, electrochemical gradients, and cell death processes. As such, the disruption of proteins that regulate calcium levels, particularly mitochondrial calcium levels, can severely affect cellular health.[85–88] Thus, understanding the affect of mitochondrial calcium levels on specific pathologies remains an ongoing research objective. Within a cellular environment metal ions perform critical roles in a variety of functions including cell signaling, electrochemical gradients and tonicity within organelles.[89–92] Of the biologically relevant metal ions, calcium ions have been implicated in both diseases and healthy cell processes.[88,93–101] The typical concentration of calcium in a healthy mammalian cell is, on average, 100 nM.[102] Two organelles are effective buffers for calcium levels: the mitochondria and the endoplasmic reticulum.[96,103–106] Several transmembrane ion channel proteins have been identified as concentration-sensitive controls for calcium levels within the mitochondrial matrix. Two of these, the sodium/calcium exchanger and the mitochondrial calcium uniporter complex, have received a considerable level of attention and will be discussed in more detail below. This discussion is relevant as focus of later discussions (Chapters 3-5) are the synthesis, characterization, and biological activity of new mitochondrial calcium inhibitors.

2.1.1 Methods to measure mitochondrial calcium

To understand calcium levels and flux within the mitochondria and cellular environments, a number of calcium sensors have been developed. The main methods to measure

mitochondrial calcium are calcium-sensitive fluorescent probes, such as the rhodamine dyes, or recombinant expression of calcium-sensitive mitochondrial-localized fluorescent proteins. Each of these is useful for specific applications, but has limitations for a holistic understanding of calcium movement. The fluorescent dyes are the most commonly utilized, due to general ease of use and the extensive use of confocal microscopy.[107,108]

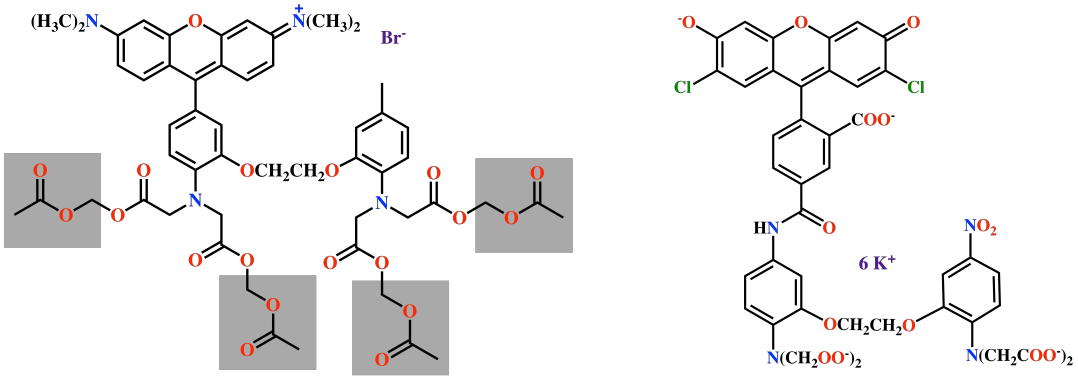

Figure 2.1: a) The structure of Rhod-2 AM in the cell-permeable acetoxymethyl (AM) ester form. The ester is cleaved intracellularly (greyed portion) which renders the dye cell-impermeable. b) The structure of Calcium Green-5N in the cell-impermeable, hexapotassium salt form.

The most common mitochondria-targeted fluorescent dye is rhod-2, which contains a positively charged imine (Figure 2.1a).[109–113] In the acetoxymethyl (AM) ester form, the dye will be taken into cells. The positively charge imine targets the dye to the mitochondrial matrix due to the electrochemical gradient existing across the inner mitochondrial membrane.[108,114] The esters will then be cleaved by mitochondrial esterases, rendering the dye impermeant and trapping it inside the mitochondria.[108,114,115] The BAPTA (1,2-bis(*o*-aminophenoxy)ethane-N,N,N',N'-tetraacetic acid) group forms the calcium binding moiety; subtle changes on this moiety will change the binding constant significantly. In the presence of calcium ions, rhod-2 will increase in fluorescence; it has a binding constant (K_d) for calcium of 570 nM.[109,110,116] Several additional analogs of Rhod-2 have been developed, tuning

the binding constant between 570 nM and 320 μM.

Many different molecular probes have been developed for calcium imaging in the cytosol.[109,112,116,117] By subtle changes in the molecular structure, different binding affinities, excitation and emissions wavelengths, and quantum yields have been accessed. Fluo-4 is one of the most common probes, with a K_d of 350 nM.[117] Other probes include the Calcium Green series, the Calcium Orange series, the Oregon Green series, Fura Red, and Fura-2.[116] Many of these are used as probes in confocal microscopy or flow cytometry. However, they can also be used in cuvette-style assay to assess mitochondrial calcium uptake. In this system the cells are incubated with a dye and suspended in a media-like buffer. One of the dyes commonly used in the these types assays is Calcium Green-5N (Figure 2.1b).[111,112,118–120] Calcium Green-5N is a relatively weak binder (K_d = 14 μM), and therefore easily releases calcium as the mitochondria uptakes the ions. The cell cocktail also typically includes a cell permeabilization agent, such as digitonin. For mitochondrial assays, permeabilization allows for the organelle to be relatively directly accessed by calcium boluses and inhibitors. The assay, although easy and quick, is highly sensitive to the number of cells - more is better.[110,111] This can be a disadvantage for cells that grow very slowly, or are very difficult to culture. In addition, these types of assays require the cell membrane to be permeabilized, usually with digitonin. While much information about inhibitors and calcium movement has been discovered with this experiment, it is not directly relevant to an *in vivo* system.

The other method to measure calcium levels is utilizing a genetically encoded luminescent or fluorescent protein.[102] These approaches are advantageous due to highly specific organelle localization via peptide targeting sequences. The aequorin protein, a luminescent protein isolated from *Aequorea victoria* is activated by calcium ions and will oxidize the aromatic substrate coelenterazine.[121–123] Using a mitochondrial targeting sequence, this luminescent probe quickly became an important tool for studying mitochondrial calcium.[124,125] Aequorin

is advantageous because it can be genetically expressed in standard transgenic models, folds properly in most cell types to form active protein, can be targeted to specific organelles within a cell, can be modified to accommodate different calcium levels, and circumvents the autofluorescence background problems found with fluorescent dyes.[126–130] However, some experimental conditions, such as the application of permeabilizing agents, will induce leakage of the probe into the cytosol leading to inaccurate data analysis.[131] In addition, the photon production was reported as relatively low, therefore single cell studies were not possible.[110,131] The mitochondria-targeted aqueorin probe is frequently used for studies with the mitochondrial calcium uniporter in yeast (discussed later).

Genetically encoded fluorescent probes have many of the same advantages as the bioluminescent probe aequorin: genetic encoding, organelle targeting and active protein expression.[132–135] These probes have the advantage over the luminescent probes due to the higher photon output of fluorescence.[110] One of the common types used are a cameleon FRET based systems, which comprise of two fluorescent protein domains joined by the calmodulin calcium binding moiety.[136,137] For example, one side will contain a blue fluorescent protein (BFP) that excites at 370 nm and emits at 440 nm. In a low calcium environment only the 440 nm emission will be observed. Upon the addition of calcium, the tertiary structure changes, and the 440 nm emission will excite a green FP (GFP), emitting now at 510 nm. Tracking both the emission of the donor (BFP) at 440 nm and the acceptor (GFP) at 510 nm allows for the observation of precise changes in calcium ion concentration.[136] Other types developed include cAMP and GMP probes, pericams, and camgaroo.[138–143] Many of these probes also contain the calmodulin moiety as the calcium binding unit. One potential disadvantage would be interference with the cellular calmodulin and its regulatory pathways, however this has not been significantly prohibitory to application.[102,110,111]

2.1.2 The sodium/calcium exchanger

Mitochondrial calcium influx and efflux is carefully regulated because of the critical role that these ions play in the maintenance of the mitochondrial membrane polarization, the control of cytosolic calcium fluctuations and general cellular homeostatis.[86,87,144,145] The mitochondrial sodium calcium lithium exchanger (NCLX) resides in the inner mitochondrial membrane and is one of several sodium/calcium exchangers discovered. The NCLX is one of the key proteins implicated in the influx of sodium ions into the mitochondrial matrix and efflux of calcium ions. The mitochondrial NCLX is unique in its ability to also transport lithium ions.[146–154] Several cellular mechanisms are present for the control of calcium and sodium ion levels in the cytosol and organelles, one of which is the NCLX.[149] The ratio of ion exchange is a subject of investigation; there is evidence for both one Ca^{2+} for either two or three Na^{+}. This ion exchange could possibly also play a role in the electrochemical potential of the cell.[155–161] The total charge ratio is 2:3 if a 1:3 ion ratio (electrogenic exchange), but a charge ratio of 2:2 if a 1:2 ion ratio (electroneutral exchange). Careful studies indicate that under low cytosolic calcium levels, the NCLX performs the 1:2 Ca^{2+}/Na^{+} electroneutral exchange. Additionally, under certain conditions, the direction of ion flux will change. For example, in myocardial ischemia the lowering of the pH will stimulate the sodium/proton pump, increasing the amount of sodium outside mitochondria.[162] The overload of sodium ions will reverse the direction of the NCLX, pumping calcium *inside* and sodium *outside*. Upon restoration of the internal pH, the NCLX will return to "normal" operating conditions: pumping calcium outside and sodium inside. At high enough cytosolic Na^{+} levels, the protein will saturate, reaching a steady state of Ca^{2+} efflux.[152–154,163]

The NCLX protein has two different active isoforms, a 70 kDa monomer and a 50 kDa monomer, isolated both from brain and heart tissue.[148] Immunoblot assays also revealed a ~100 kDa dimer isolated from HEK293 (epithelial kidney cells) mitochondria.[150] Based on

analysis of the crystal structure of a NCLX homolog, there are three Na^+ and one Ca^{2+} binding sites, consistent with studies determining that the protein was electrogenic (Figure 2.2). The structure revelas a membrane bound protein with ten transmembrane domains that appears as sets of two helices (α1 and α2).[154,164,165] The Na^+ and Ca^{2+} binding site regions are highly conserved through the NCX protein superfamily, and are maintained although the NCLX was found to diverge evolutionarily relatively early on.[149]

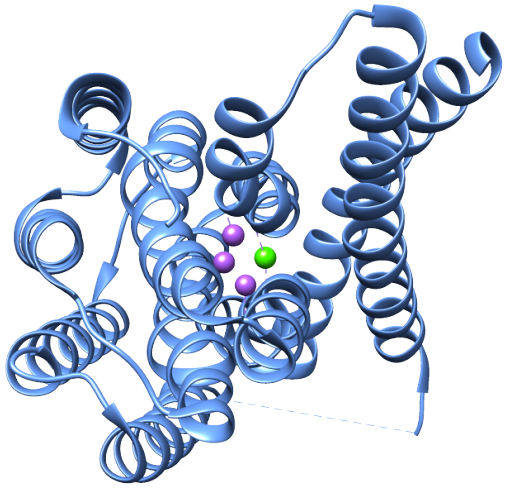

Figure 2.2: Crystal structure of the sodium calcium exchanger homolog crystallized from *Methanococcus jannaschii*. The purple atoms are Na^+ and the green atom is Ca^{2+}. PDB 3V5U.[164]

In cardiac ischemia and reperfusion, the deleterious outcome is substantially caused by high mitochondrial Ca^{2+} levels. The controlled efflux of Ca^{2+} is critical to prevent the formation of the mitochondrial permeability transition pore. The mitochondrial permeability transition pore is a set of proteins that forms under high calcium ion conditions, and begins the signal cascade leading to apoptosis. Thus, the balance of the mitochondrial calcium uniporter and NCLX proteins is critical for ionic homeostatis between the mitochondria and the cytosol.

2.1.3 The mitochondrial calcium uniporter complex

The mitochondrial calcium uniporter (MCU) was first posited to explain the observed regulated increase of calcium ions into the mitochondria.[166] However, it was unknown if it was a single protein, or a set of proteins. The complete mitochondrial protein inventory (MitoCarta) was determined in 2008.[167] This inventory led to the identification of MICU1, a protein associated with mitochondrial Ca^{2+} influx.[168] Soon afterwards, MICU2, MCUb and MCU were also identified, with the MCU determined to only be the pore-forming protein.[169–172] MCUb is a paralog of MCU and also assists in regulation, although there is limited knowledge of the precise function.[173,174] The last piece was the EMRE, a small regulatory subunit that was found to be critical for MCU function and calcium uptake (Figure 2.3).[174,175]

Although the MCU is the protein that forms the transmembrane pore (Figures 2.4a and 2.4b), the other components are critical for function. MICU1 and MICU2 both contain EF hand domains (Ca^{2+} binding domain) and reside in the intermembrane space of the mitochondria. Specifically, the EF hand domain in MICU1 was observed in the crystal structure and was shown to be critical to MCU function.[176,177] These two proteins are thought to act as "gatekeepers" through their association with each other and the MCU – a double knockout of the MICU1 significantly decreases the mitochondrial calcium influx.[174,178–182] The EMRE is a 10 kDa protein with a predicted transmembrane domain and a mitochondrial targeting sequence.[174] Knockout studies showed that loss of the EMRE had the same effect as loss of MICU1, suggesting that EMRE mediates interactions between the MCU and MICU1. Two recent studies indicate that one of the functions of the EMRE is to stabilize the MCU complex and raise the kinetic barrier to proteolysis.[183,184] However, this is not universal as the EMRE is primarily expressed in metazoa; the regulatory subunits are not necessary for function of the non-metazoan derived MCU.[174] Only the non-metazoan *Dictyostelium dis-*

coideum MCU was required for calcium influx, however both the EMRE and MCU were required for the human homolog.[175] *Sacharomyces cerevisiae* does not have an MCU. This was taken advantage of to express the MCU and EMRE in *S. cerevisiae* along with the mitochondrial-targeted aqueorin luminescent probe. The ability to express this protein system in yeast has opened up avenues of research into the mechanisms and inhibitors of the MCU.[185–187]

The proteins form a complex residing the inner mitochondrial membrane, with the MICU1 and MICU2 primarily in the intermembrane space (Figure 2.3). The voltage-dependent anion channel (VDAC) forms the ion pore between the cytosol and the intermembrane space and allows calcium to pass through uninhibited.[188] In low calcium-concentration conditions the MCU pore will remain closed as little to no calcium ions will be bound to MICU1 and MICU2. However, under high calcium concentrations the opening of the MCU pore will be exposed to allow calcium to move into the mitochondrial matrix.[87]

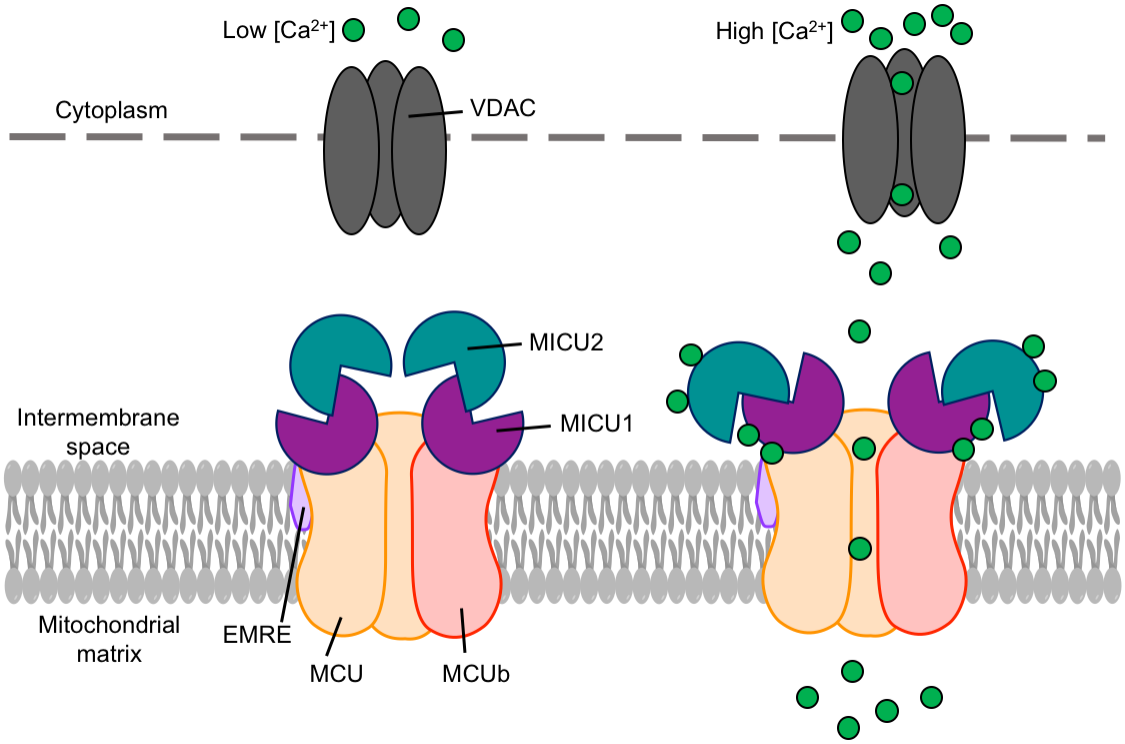

Figure 2.3: Schematic of the assembly required for mitochondrial calcium uptake suggested by Mammucari et al.[87]

The MCU in *C. elegans* was found to be expressed well in *E. coli* (designated cMCU).[189] Using a combination of cryo-electron microscopy and 2D NMR spectroscopy, the structure of cMCU was determined to be pentameric, with each subunit identical (Figures 2.4a and 2.4b).[189] Each subunit consisted of a set of α-helices connected by a short disordered loop in the intermembrane space and a disordered bulge about halfway through the trans-membrane section (Figure 2.4b). The disordered loop had an amino acid sequence designated as the DIME loop (Figure 2.4c). This loop was found to be well conserved across different homologues of the protein – specifically the aspartic acid (D) and the glutamic acid (E) did not change, while the isoleucine and methionine could vary.

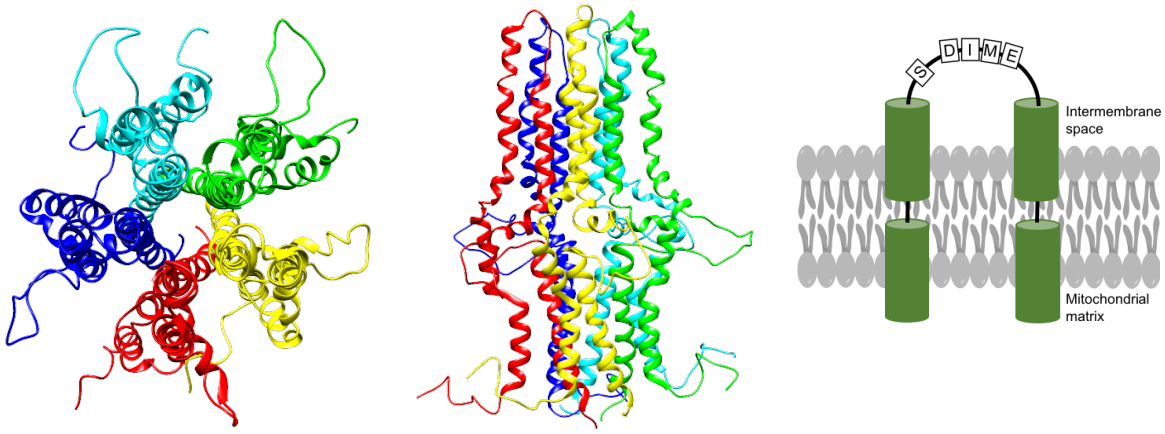

(a) (b) (c)

Figure 2.4: (a) Head-on structure of the cMCU from mitochondrial intermembrane space, showing the transmembrane pore. Each color represents a subunit of the pentameric structure. (b) Side view of the cMCU, showing the transmembrane helices. (c) Schematic showing the location of the conserved serine (S) and DIME loop. PDB 5id3.[189]

Adjacent to the DIME loop is a conserved serine residue. A point mutation of this serine to alanine had no effect on protein function. However, the most common inhibitor for the MCU, Ru360, was found to be less effective in this mutant.[169] In contrast, mutation of aspartic acid attenuated protein function significantly.[185,189] Comparison with the human homolog of the MCU by key amino acid mutations showed that the structure and function was the same as in the cMCU.[189] With the structure of the MCU solved several molecular docking studies have been performed to analyze the molecular interactions of inhibitors.[185,186]

2.1.4 Ischemia reperfusion injury

In a heart attack, or myocardial infarction (MI) episode, a myocardial infarct (artery blockage) forms constricting blood flow and reducing oxygen levels in tissue. As blood flow is restricted, oxygen levels diminish and the heart enters a state of hypoxia. This process stimulates anaerobic metabolism, producing high levels of lactic acid and lowering the cellular

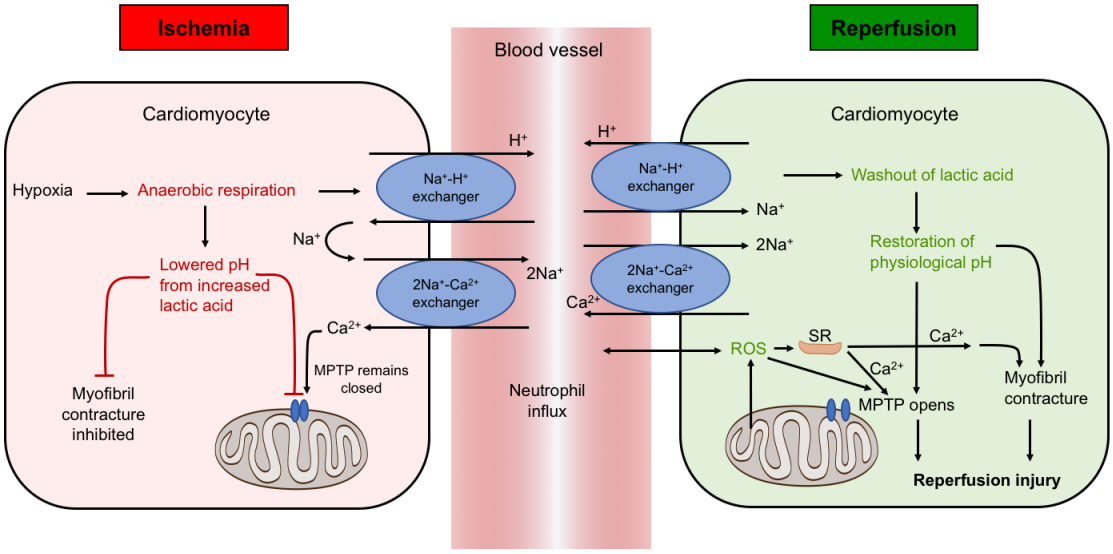

Figure 2.5: A schematic of ischemia and reperfusion. Under hypoxia, anaerobic respiration is activated which lowers the pH via production of lactic acid and pumps calcium into the cardiomyocte. The mitochondrial permeability transition pore (MPTP) remains closed and myofibril contracture is inhibited. Upon return to the normoxic environment the lactic acid buildup is flushed, restoring physiological pH. Calcium is pumped out of the myocytes by the directional switching of the sodium calcium pump. ROS levels increase after restoration of the electron transport change mechanism which will in turn stimulate the saroplasmic reticulum to release more calcium, and inducing the opening of the MPTP. Additionally, due to the restoration of the mitochondrial membrane potential, calcium will flood into the mitochondria also leading to MPTP opening. This, as well as myofibril hypercontracture, will result in tissue-level reperfusion injury. Schematic as suggested by Yellon et. al.[190]

pH (Figure 2.5, left).[162,190] The mitochondrial permeability transition pore (MPTP, a channel through the inner membrane within the mitochondria) will remain closed due to the low pH. The excess H^+ ions are removed by exchange with sodium ions via the sodium/proton exchanger. The excess sodium ions in turn induce the sodium/calcium exchange protein to remove sodium ions and bring excess calcium in. The acidic environment also inhibits the electron transport chain, reducing the amount of ATP produced.

After the arterial blockage is cleared, the oxygen levels are restored (reperfusion) and the lactic acid is flushed from the cell. The sodium-proton and the sodium-calcium pumps

are stimulated, raising the intracellular sodium ion concentration and removing some of the excess intracellular calcium (Figure 2.5, right). The restoration of neutral pH restores the inner mitochondrial membrane potential, usually around -180 mV. Calcium will flood the mitochondria upon this restoration. The electron transport chain reactivates and ATP synthesis is restored. Reactive oxygen species (ROS) are a byproduct the electron transport chain mechanism. As the ROS levels rapidly increase the sarcoplasmic reticulum releases additional calcium. The sudden increase in mitochondrial calcium stimulates the opening of the MPTP several minutes after reperfusion. The opening of the MPTP is key as it is associated with the onset of apoptosis due to the decoupling (setting to 0 mV) of the inner mitochondrial membrane potential and results in ATP depletion.[191] The increase in calcium levels will also induce myofibril contrature (contraction of the heart muscle), increasing reperfusion injury. *In vivo* experiments inhibiting the sodium-calcium pumps, mitochondrial calcium uniporter, and sodium-proton pumps show decrease in infarct size; however corresponding clinical studies are less promising.[145,162,190,192–194]

With short ischemic time periods reperfusion can be beneficial but if the ischemic timespan is excessive reperfusion injury occurs. Inhibition of reperfusion injury accounts for 50% reduction of infarct size, suggesting that reperfusion is responsible for infarct formation. Several different types of reperfusion injury have been shown to be possible; lethal reperfusion injury is the method with the fewest therapeutic options and the most severe.[162,195,196] The other types of injury generally have therapeutic options or can be recovered from: reperfusion arrhythmias, myocardial stunning, and the microvascular obstruction, discussed below.

Reperfusion arrhythmia (RA) was described over 30 years ago; it is the irregular rhythm of the heart upon reperfusion.[197] While this type of injury is undesirable on the long term, the early evidence of RA can be considered therapeutically beneficial, particularly in STEMI, the most severe form of myocardial infarctions. A number of therapeutics and treatment

methods are well established for RA.[198] Myocardial stunning, a second type of reperfusion injury, is a form of mechanical dysfunction that persists in spite of blood flow restoration and the apparent absence of irreversible damage.[199–202] Although there are no established therapeutic avenues, it is typically minor and does not greatly impact the quality of life.[203] A variety of hypotheses have been posited about the mechanism, however none have been conclusively confirmed.[200,204–206] Another form of reperfusion injury is microvascular obstruction (MVO): the "inability to reperfuse a previously ischemic region".[207] This is an irreversible form of injury which will result in the death of the myocardial tissue. In patients with STEMI, MVO is associated with larger infarct sizes and poorer short-term and long-term prognoses.[190,202,208–210] The fourth type is lethal myocardial reperfusion injury. This type is characterized by the presence of viable myocytes at the end of ischemia, but subsequently die during reperfusion.[190,202] During this process contributions to myocyte death include (but are not limited to) oxidative stress, calcium overload, and mitochondrial permability transition pore opening. There are limited therapeutic options currently, but lethal reperfusion injury is considered a viable target.[190]

2.2 Inhibitors of the mitochondrial calcium uniporter

As mitochondrial calcium uptake is critically related to reperfusion injury, the inhibition the MCU is a potential therapeutic target. A small number of inhibitors of the MCU have been discovered, starting with ruthenium red (RuRed), and most recently, a few organic inhibitors. The mechanism of action for effective inhibition is currently unknown, and new inhibitor discoveries are infrequent. Two docking studies report that hydrogen bonding to the amino acids at the opening of the MCU are critical. However, only one of these reports systematically studied the structure-activity relationship of a number of potential inhibitors.[185,186]

2.2.1 Organic inhibitors

Several organic inhibitors of mitochondrial calcium uptake have been recently discovered[185,211–214]. They are all relatively polar compounds containing number of hereoatoms and a mix of aromatic and aliphatic regions (Fig. 2.6).

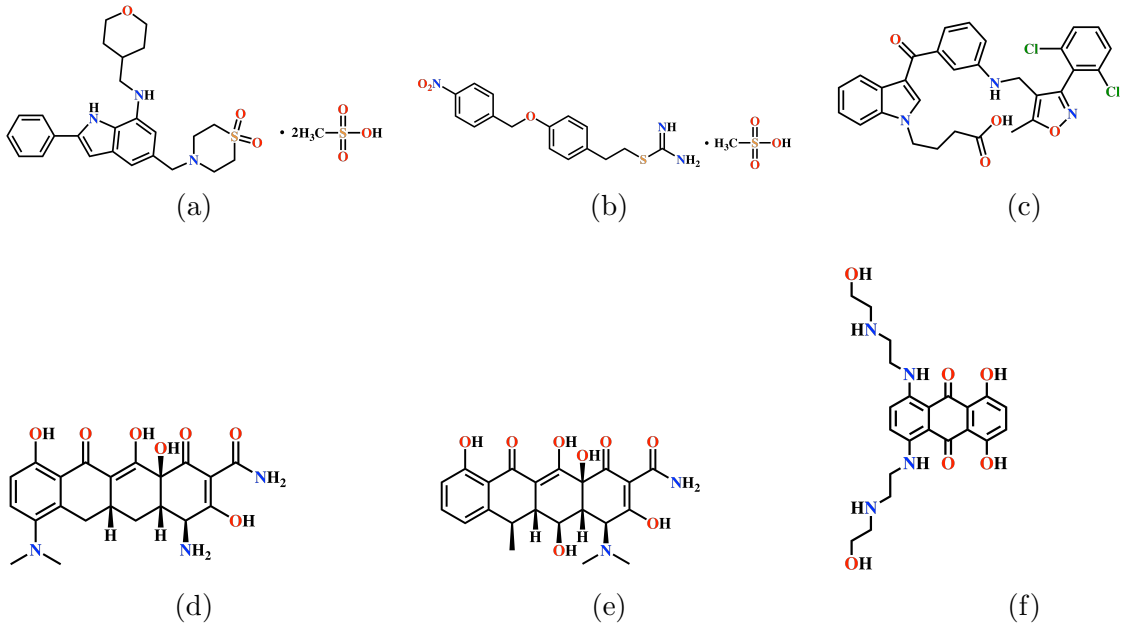

Figure 2.6: The organic inhibitors of the MCU investigated: (a) Necrox-5[215], (b) KB-R7943[211], (c) DS16570511[213], (d) minocycline[216], (e) doxycycline[216] and (f) mitoxantrone[185].

The similarity of these structures suggests they operate by similar mechanisms of action. However, each has been studied using different methods. Many experiments used whole cell or tissue experiments, such as membrane polarization, ROS levels or Ca^{2+} levels within the mitochondria to draw conclusions. A number of these experiments compared the potential inhibitors to ruthenium red and Ru360, the commercially available and best studied MCU inhibitors.

NecroX-5 is one of the members of the NecroX family of cell-permeable necrosis-inhibiting drugs (Figure 2.6a).[212,215,217] The NecroX family primarily localizes into the mitochondria,

and is reported to have antioxidant activity. NecroX-5 was found to decrease mitochondrial ROS generation and mitochondrial Ca^{2+} uptake, suggesting it inhibited the MCU. To determine the inhibitory activity, whole rats hearts or isolated myocytes were perfused first with a hypoxic ischemic solution and then reperfused with normoxic solution with or without NecroX-5 or ruthenium red. Infarct size, mitochondrial membrane potential, and mitochondrial calcium levels were determined. Treatment with ouabain, a Na^+/K^+ ATPase inhibitor which induces mitochondrial Ca^{2+} overload, or histamine, a stimulant for calcium release from the endoplasmic reticulum, with NecroX-5 suppressed the uptake of calcium into the mitochondria. This suggests that NecroX-5 is a specific inhibitor of the MCU; no affect on the Na^+/Ca^{2+} ion channel was observed. No additional studies with NecroX-5 as an MCU inhibitor have been published to date.

Another organic inhibitor of the MCU is KB-R7943 (Figure 2.6b).[211] This compound was initially discovered as a Na^+/Ca^{2+} ion channel inhibitor, and was shown to also protect against ischemia/reperfusion. Using the calcium dependent mitochondrial targeted photoluminescent protein aequorin, the levels of calcium within the mitochondria were analyzed under various inhibitor concentrations. Via this method, the 50% inhibition constant of calcium uptake (IC_{50}) for KB-R7943 was found to be 5.5 μM in permeabilized HeLa cells.

Minocycline and doxycycline (Figures 2.6d and 2.6e) are two members of the tetracycline family, a group of compounds used as antibiotics for many years.[214,218,219] However, a few of these compounds were found to have additional therapeutic value. One mode of action was protection against reperfusion injury.[216,220–222] When given to freshly isolated hepatocytes, both minocycline and doxycycline block mitochondrial calcium uptake and protect against cell death induced by ischemia/reperfusion, with doxycycline being more effective. These compounds also inhibited the mitochondrial permeability transition pore opening. In comparison with Ru360, both of these compounds were less effective and appeared to be

acting on the MCU. Full dose response curves were not determined, however from a 3-dose study minocycline and doxycycline had 50% inhibition constants of about 20 μM and 5 μM, respectively.

The aforementioned MCU inhibitors were all therapeutics initially utilized for specific pathologies. Following this concept, recent work to discover additional inhibitors has focused on high-throughput screenings of known small drug molecules. The first study discovered one compound, DS16570511 (Figure 2.6c), out of a screen of 120,000 compounds using HEK293A cells (healthy endothelial kidney cells).[213] Although the assay was not discussed in detail, the criteria for a positive result required an IC_{50} of 10 μM or below for the cell-based calcium inhibition, a sevenfold lower IC_{50} for the isolated mitochondrial inhibition, a reproducible inhibitory activity, and inhibition must be present in human cells, and both small and large animals. The IC_{50} with isolated mitochondria was found to be 860 nM, compared with their experimental value of 20 nM for Ru360. In permeabilized cells, the IC_{50} was significantly larger: 7 μM.

The second example using high-throughput screening discovered mitoxantrone (Figure 2.6f) out of 70,000 compounds.[185] The authors developed a high-throughput assay using isolated yeast mitochondria expressing the mitochondrial-targeted aequorin luminescent protein as a calcium probe. Since yeast do not express the MCU naturally, this method of screening of potential MCU inhibitors is relatively straightforward. Additionally, the generation of MCU mutants to probe the precise mechanism of inhibition is utilized. The authors expressed the D261A MCU mutant — the D261 conserved residue shown previously to be necessary for inhibition. This aspartate residue is key for Ca^{2+} uptake; mutation to alanine reduces protein function by about 4-fold. Inhibition of calcium uptake by ruthenium red was also greatly attenuated, compared to the wild-type protein. However, mitoxantrone inhibition was not significantly reduced by the D261A mutant, consistent with the MCU

molecular docking studies. Significant hydrogen bonding occurred with the long side chains, and the structure had a more flexible bonding mode due to binding via the ring and the dual "arms" (Figure 2.6f). Modifications of those arms showed that the both chain length and hydrogen bonding ability was critical for inhibition, Tests with the structural analog containing $CH_2CH_2NH_2$ arms (pixantrone) inhibited, but much more poorly. These studies 1) showed the difficulty in discovering new MCU inhibitors and 2) revealed clues into the mechanism of action for effective inhibition.

2.2.2 Inorganic inhibitors

Ruthenium-based MCU inhibitors have been more extensively studied than the aforementioned organic inhibitors. Additionally, some studies have considered other metal ions, specifically La^{3+} and Co^{3+}. To date, the most effective inhibitor is still ruthenium based[223] and these types of complexes are the most commonly used.

Lanthanum and cobalt

La^{3+}, along with ruthenium red (discussed below), was one of the first MCU inhibitors discovered.[224] At the initial discovery of the inhibitor action of RuRed and La^{3+}, the proteins responsible for calcium transport into the mitochondria were still unknown, although the phenomenon of calcium transport was known and a subject a much research. Several lanthanide ions were tested — lanthanum, europium, terbium, and neodymuium. La^{3+} was found to inhibit calcium uptake, however over time the inhibitory ability decreased within the sample, suggesting the La^{3+} ions were being taken up into the mitochondria. This decrease was attributed to the mitochondria actually uptaking the La^{3+}, albeit slower than Ca^{2+}. The other lanthanide ions were found to behave in a similar manner. In addition,

the inhibition leveled out without fully inhibiting calcium uptake. La^{3+} was found to bind to additional sites on the mitochondria, termed "low affinity binding sites". An additional study found that lanthanum did not inhibit calcium movement, but seemed to localize the in the mitochondrial membranes.[225] Overall, these findings indicated that lanthanum was not an effective inhibitor of calcium transport.

Two examples in the literature utilized cobalt complexes as MCU inhibitors. Four cobalt candidates were considered: $[(NH_2(CH_2)_5NH_2)Co(NH_3)_5]^{3+}$, $[Co(H_2O)(NH_3)_5]^{3+}$, $[Co(NH_3)_6{}^{3+}$, and $[Co(Ala)(NH_3)_5]^{3+}$. Dose-response curves were determined, and the best inhibitor was found to be $[(NH_2(CH_2)_5NH_2)Co(NH_3)_5]^{3+}$ with an IC_{50} of 140 nM on isolated mitochondria from rat liver tissue.[226] The second report investigated a number of metal tris(ethylenediamine) complexes, including the metals Co(III), Rh(III), Cr(III), Ru(II), Fe(III) and Cu(II).[227] Of these, the Co(III) complex had the lowest IC_{50} at 53 nM, again on isolated mitochondria. Co(III) hexaammine was tested with an IC_{50} at 550 nM. These results indicate that relatively simple complexes are effective inhibitors, and was one of the first examples showing that basic structural tuning may provide insight into the necessary structure-activity relationship for MCU inhibition.

Ruthenium red and Ru360

Ruthenium red (RuRed) is a tri-ruthenium +6 cation that has been used for many years as a histological stain (Figure 2.7a).[228] Due to the high charge of RuRed, it binds very effectively to mucopolysaccarides and has been reported to bind to nucleic acids. Additionally, it has a very large extinction coefficient (68,000 $M^{-1}cm^{-1}$ at 532 nm) enabling easy microscopic visualization.[228–231]

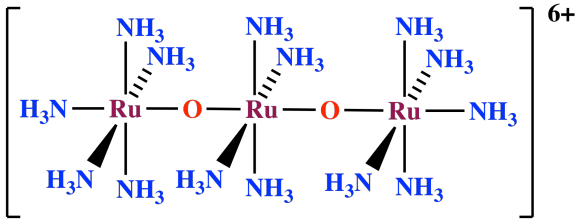

(a) Ruthenium Red (RuRed)

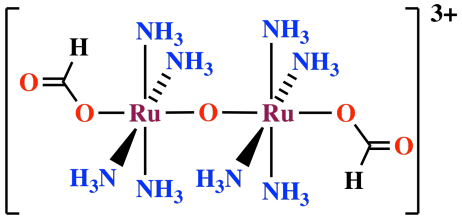

(b) Ru360

Figure 2.7: The chemical structures of the two common ruthenium based MCU inhibitors, (a) ruthenium red (RuRed) and (b) Ru360.[232,233]

It had been observed that ruthenium red also stained mitochondria.[234] Mucopolysaccarides present on the mitochondrial membrane were known to be good calcium ion binders.[234,235] Thus, RuRed was considered as a candidate for altering the calcium binding of mitochondria.[234] This study showed that 1) RuRed bound to rat liver mitochondria on the same order of magnitude as Ca^{2+} binding and 2) RuRed inhibited Ca^{2+} uptake into the mitochondria.[234] The overall effect was complete inhibition of calcium-dependent respiration, without effecting ADP phosporylation.[224,236,237] At the time of these early studies, two types of mitochondrial calcium binding sites were known, "high-affinity" and "low-affinity", although the proteins involved were not known. Both types of sites were inhibited by RuRed, with the "high-affinity" sites more effectively inhibited.[224] RuRed was determined to inhibit calcium transport into the mitochondria, but had little effect on the efflux mechanism.[238] Voltage-sensitive calcium channels, such as those found in neurotransmitters, were also inhibited by RuRed, although it was found to be cytotoxic, decreasing cell viability.[237,239,240] These seminal studies established RuRed as an inhibitor of calcium transport into the mitochondria, even though the exact mechanism of transport and the key proteins had yet to be determined.

Although RuRed was used as a tool for many additional investigations, it was noticed that the yield of preparation were low, typically 20% or less. It was suggested that a "colorless contaminant" with a strong absorbance around 355 nm also had inhibitory properties, at

a much higher activity per Ru atom than RuRed.[241] An additional study showed that upon repeated purification of RuRed, the activity actually *decreased*.[242] These observations led to the discovery of Ru360, a dinuclear oxo-bridged +3 cation, as a potent calcium ion inhibitor (Figure 2.7b).[233,243] In whole cardiomyocytes, both RuRed and Ru360 showed calcium uptake inhibitory properties.[119,244] As the different proteins involved in mitochondrial calcium uptake were discovered and their mechanisms elucidated, both RuRed and Ru360 were extensively used.[169,185,186,189,192,214,245–248] The most potent commercial inhibitors, Ru360 and RuRed are often compared to other inhibitors.[185,212,213,223,226,227] Mechanistically, few studies have been done. As mentioned above, early experiments established "high-affinity" and "low-affinity" calcium binding sites, with the high-affinity sites more strongly inhibited than the low-affinity sites. The high-affinity site could be the MCU whereas the low-affinity site is likely the anionic phospholipid membranes. A molecular docking study of Ru360 into the MCU pore showed a number of hydrogen bonding interactions with the conserved aspartate of the DIME loop, similar to the docking study with mitoxantrone.[185,186] Mutations of the conserved aspartate (D261A) significantly decreased the calculated binding of Ru360. This finding corroborated the experimental studies that showed the D261A mutant of the MCU was significantly less sensitive to Ru360 inhibition.[185,186,189]

Of relevance for this discussion is the effect RuRed and Ru360 have on ischemic reperfusion injury (IRI). Since this is a calcium-dependent pathology, any potent inhibitor of mitochondrial calcium may be therapeutically useful. The initial study using RuRed as an IRI protective agent used adult rabbits, treating the hearts with 1 μM complex during reperfusion. Afterwards, the rabbits were sacrificed and the hearts harvested for additional studies. It was determined that the total tissue had an increase in calcium, however RuRed was able to attenuate the levels of mitochondrial calcium.[249] Additional studies found similar affects in rat hearts; overall, RuRed had a larger effect on reperfusion injury with minimal affect on ischemia.[250,251] This is consistent with the expected mitochondrial calcium levels

in ischemic conditions *vs.* reperfusion conditions (Figure 2.5). Another study considered the effect of RuRed as a protective agent on cold ischemia — or the ischemia generated when a transplant organ is kept in cold storage.[252] Calcium levels do increase under ischemic conditions, and this is exacerbated when a tissue is chilled due to the disruption of ATP production. In this case, there was an attenuation of cold ischemic conditions with treatment of RuRed.

In the case of Ru360, a few studies also considered the protective effects. A common compound that is frequently used to protect against IRI is cyclosporin A.[190] Rather than inhibiting calcium uptake into the mitochondria, cyclosporin A inhibits the opening of the mitochondrial permeability transition pore.[193,253–257] Already in clinical trials, cylcosporin A is frequently used as the lead compound to compare potential IRI protective agents.[258] In isolated cardiomyocytes, Ru360 reduced the amplitude of pathological calcium ion oscillations associated with reperfusion injury, with similar efficacy as cyclosporin A.[255] Several studies showed that Ru360 protected against IRI by limiting the level of mitochondrial calcium during ischemia and reperfusion.[259,260] Ru360 was also found to accumulate in cells in a biphasic manner, the first, quicker binding, associated with cell membrane binding and the second, slower accumulation, with intracellular uptake.[119] An *in vivo* study was consistent with the aforementioned *in vitro* findings. Only 2.1 pmol Ru360/mg protein from myocardial tissue was detected - much lower than the IC_{50} of Ru360, thus implying that less than complete inhibition would occur. Ventricular tachycardia (VT) and ventricullar fibrillation (VF) are two pathologies observed in reperfused hearts. In spite of the low levels of Ru360 accumulation, in treated hearts VT and VF were both completely absent. In addition, Ru360 significantly protected against reperfusion induced oxidative damage.[261] These studies indicate the great therapeutic potential of ruthenium-based MCU inhibitors. One limitation has been lack of effective cellular uptake; another has been characterization of off-target inhibition. Although Ru360 has been touted as a highly selective inhibitor, no studies have attempted to consider

other protein targets. This opens up the possibility of many research avenues, including molecular tuning and structure-activity relationships, as well as extensive molecular biology investigations. We have explored a few examples of structure-activity relationships and the effects of small molecular changes on the biological activity.

CHAPTER 3

SYNTHESIS AND CHARACTERIZATION OF A RU360 ANALOG

3.1 Introduction[1].

The trinuclear oxo-bridged ruthenium complex, ruthenium red (RuRed, Figure 3.1a) is a commercially available inhibitor of the mitochondrial calcium uniporter (see Chapter 2 for more detail). The use of RuRed, however, is limited by its poor selectivity for the MCU, as well as by the large number of impurities found in commercial sources of this compound.[224,242] The history of this complex is of interest due to its relationship to Ru360, the most commonly used inhibitor today. RuRed was initially discovered in the late 1800s and has since been used as a cellular stain due to its intense magenta-red color and high positive charge.[228,231,262] RuRed can be prepared by treating $RuCl_3$ with concentrated aqueous ammonia.[230,263] A single report used $[Ru(NH_3)_5Cl]Cl_2$ in the presence of aqueous ammonia and 10% oxygen to produce a compound reported as RuRed. However, the only reported characterization was a resonance Raman spectrum consistent with RuRed.[264] The reaction starting with $RuCl_3$ did not produce pure product: Fletcher et al. reported an impurity visible by UV-vis spectroscopy at 725 nm.[230] Luft purified RuRed by recrystallization and isolated the 725 nm fraction, dubbing it "ruthenium violet".[228,230] The reaction to synthesize RuRed was quite low yielding (20% or less) suggesting that other compounds were present. A contaminant with a strong absorbance around 355 nm contained high levels of ruthenium, leading to the discovery of Ru360, a dinuclear ruthenium oxo-bridged complex.[233,241,243]

The structure of the RuRed was not solved for almost 100 years after the initial synthetic report.[230,232,262,263,265] The first attempt solved the X-ray crystal structure as a "chloroxy"

[1]Chapter reproduced in part with permission from *Inorg. Chem.*, **2017**, 56(6), pp 3123 - 3126. Copyright 2017, American Chemical Society

complex without a clear bridging system between the metal centers.[266] This structure was proven incorrect by the formation and subsequent X-ray structure determination of the thiosulfate salt, suggesting the initial structure reported was of an impurity.[232] Substitution of the four ammines for two ethylenediamine ligands on the center ruthenium of RuRed produced a complex that contained two μ-oxo moieties (Figure 3.1a)[267]. This simple substitution corroborated the existence of three ruthenium atoms and two μ-oxos as the backbone of RuRed. Spectroscopically, comparison with a previously discovered μ-oxo bridged ruthenium system, $K_4[Ru_2OCl_{10}]$, assisted in determining the RuRed structure. The Ru-O-Ru vibration is characteristic in the infrared spectrum; $K_4[Ru_2OCl_{10}]$ RuRed have a Ru-O-Ru stretches at 888 cm^{-1} and 813 cm^{-1}, respectively.[268,269]

Charge balance necessitates that the ruthenium atoms exist in different oxidation states, the outer two in the +3 state and center atom in the +4 state. Upon a 1-electron oxidation the oxidation states of the outer ruthenium atoms each increase to a formal +4 while the inner decreases to +3; this oxidized product is called "ruthenium brown".[230] Ruthenium-99 Mössbauer spectroscopy was used to probe the valence delocalization of the ruthenium centers.[270,271] Although the acquired Mössbauer results for RuRed were consistent with a Ru^{III}-Ru^{IV}-Ru^{III}backbone, this hypothesis was not compatible upon oxidation to ruthenium brown. The expected spectral features for ruthenium brown were similar to RuRed: the same isomer shifts but a 2:1 Ru^{IV}:Ru^{III} pattern for ruthenium brown. However, the isomer shifts were larger than expected and the Ru^{IV}:Ru^{III} patterns were not what was expected. Wagner and co-workers attribute this discrepancy to the 1-electron oxidation not coming from a distinct center, but "smeared" over the entire backbone.[271] Thus the interpretation is that RuRed and ruthenium brown are valence-delocalized across the μ-oxo backbone and the ruthenium metal centers do not have discrete oxidation states.

Commercially available RuRed preparations are still notoriously impure, which inhibits

its use as a precise therapeutic (see Chapter 2 for therapeutic applications of RuRed).[242] One of the impurities found in formulations of RuRed is a dinuclear oxo-bridged compound, $[(HCO_2)(NH_3)_4Ru(\mu\text{–}O)Ru(NH_3)_4(O_2CH)]^{3+}$ (Figure 3.1b).[233,243] This compound was selectively synthesized from $RuCl_3$ and aqueous ammonia. Purification of Ru360 was accomplished with cellulose-based, weakly acidic cation exchange chromatography using Whatman CM-52 resin and ammonium formate (NH_4HCO_2) buffer as the mobile phase. This gave Ru360 as the formate-capped form, $[(HCO_2)(NH_3)_4Ru(\mu\text{–}O)Ru(NH_3)_4(O_2CH)]^{3+}$ in low yield.

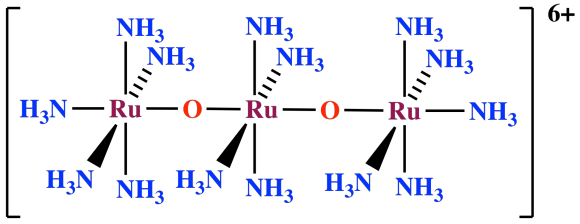

(a) Ruthenium Red (RuRed)

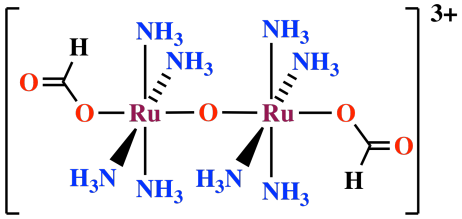

(b) Ru360

Figure 3.1: The chemical structures of the two common ruthenium-based MCU inhibitors, (a) ruthenium red (RuRed) and (b) Ru360.[232,233]

Through our investigations of Ru360, we synthesized and characterized a functional analogue. This analogue, $[(OH_2)(NH_3)_4Ru(\mu\text{–}O)Ru(NH_3)_4(OH_2)]^{5+}$ (**3.1**), is a simple variation of Ru360 where the axial formate ligands are replaced by water molecules. Three distinct synthetic methods for its isolation and detailed physical characterization are reported. Additionally, the potent inhibition of mitochondrial calcium uptake in both permeabilized human cells and isolated yeast mitochondria expressing the human MCU and its essential regulator EMRE is demonstrated in Chapter 5.

3.2 Synthesis and purification[2]

In our initial efforts we followed the previously reported synthesis for Ru360.[233,243] Briefly, $RuCl_3 \cdot n\,H_2O$ was treated with 6 M HCl containing 12% ethanol and heated at 90 °C to reduce any Ru(IV) and nitrosyl impurities (Figure 3.2). Concentrated NH_4OH was added to precipitate a solid material, which was then re-suspended in additional concentrated NH_4OH and heated at 40 °C overnight. Notably, this step of the reaction required a sealed reaction vessel; heating in an open container did not produce the desired compound (**3.1**). The reaction mixture was centrifuged to isolate the final crude solid. The desired product was readily identified by a UV-vis absorbance band centered at 360 nm. The formation of RuRed as a byproduct was also evident in the crude mixture from a broad absorbance band centered at 530 nm. Due to the unavailability of the Whatman CM-52 resin, the resin used in the published preparation, we investigated alternative solid-phase supports for purification. A column packed with the strongly acidic cation exchange resin, Dowex® 50WX2, and a mobile phase of HCl was found to be effective for purification, as these were previously used for isolating a chloride-capped analogue of Ru360. The column was prepared and packed with 0.1 M HCl and eluted starting at 1 M HCl. At 2 M HCl, a byproduct of this reaction, confirmed to be $[Ru(NH_3)_5Cl]Cl_2$ by single-crystal X-ray diffraction (Figure 3.3a and Table 3.1), eluted as a yellow band. Upon increasing the HCl concentration to 2.5 M and then 3 M, pure compound **3.1** came off the column as a green-brown solution. At higher HCl concentrations (>4 M), RuRed and its oxidized form, ruthenium brown, could also be eluted, as evidenced by the red-brown color in the fractions. Fractions were tested by UV-vis for purity, checking for the diagnostic 360 nm band. These fractions were evaporated to afford a green-brown solid, which elemental analysis formulates to be $[(OH_2)(NH_3)_4Ru(\mu\text{–}O)Ru(NH_3)_4(OH_2)]Cl_5{\cdot}1.5\,H_2O$, in typical yields of 10 to 20 mg (1.7 to 3.4%) starting from 250 mg of $RuCl_3 \cdot n\,H_2O$. The low yields can likely be accounted for due

[2]Additional details for all syntheses can be found in appendix A.

the limited solubility of the crude compound in acid when it was loaded on the column. The low yields and tedious purification prompted us to search for alternative synthetic methods for preparing compound **3.1**.

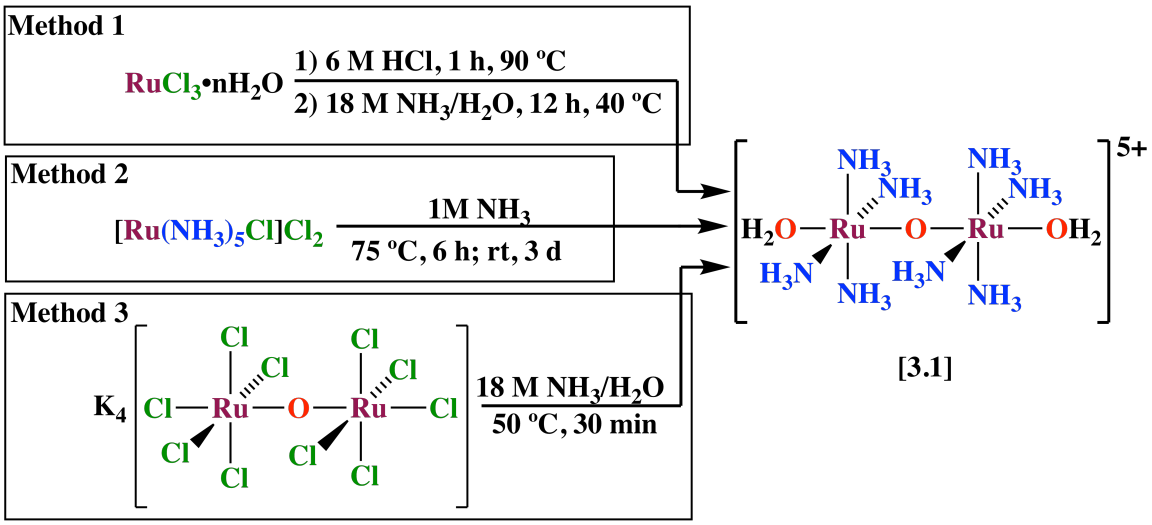

Figure 3.2: The three methods used to synthesize the Ru360 analog $[(OH_2)(NH_3)_4Ru(\mu{-}O)Ru(NH_3)_4(OH_2)]^{5+}$ (**3.1**).

$[Ru(NH_3)_5Cl]Cl_2$ was synthesized following previously reported procedures and characterized by IR spectroscopy (Table 3.4). We found that heating $[Ru(NH_3)_5Cl]Cl_2$ in 1 M NH_3 in a capped reaction vessel at 75 °C for 6 h followed by stirring at room temperature for 3 days gave rise to a dark green solution with an intense absorbance band at 360 nm, an indicator of a Ru360-like complex (see Figure 3.2, Method 2). When the reaction vessel was capped, no formation of RuRed is observed. Performing the same purification by ion-exchange chromatography with Dowex® 50WX2 resin, as described above, afforded **3.1**, also as a green-brown solid. The typical yields for this method were on the range of 10 to 20% starting from $[Ru(NH_3)_5Cl]Cl_2$. While the yield was significantly increased for this method, it was still quite low. As some starting material was isolated during the purification, it is likely the reaction does not go 100% to completion. Increasing the reaction time, or tuning the conditions further may alleviate the problem.

We also explored the utility of $[Ru_2OCl_{10}]^{4-}$ as a synthon for these complexes containing the Ru(μ-O)Ru core. The compound $K_4[Ru_2OCl_{10}]$ was prepared as described previously and characterized by single-crystal and powder X-ray diffraction (Figures 3.3b and A.1 and Table 3.1). Accordingly, the reaction of $[Ru_2OCl_{10}]^{4-}$ with concentrated NH_4OH at 50 °C for 30 min produced $[(OH_2)(NH_3)_4Ru(\mu{-}O)Ru(NH_3)_4(OH_2)]^{5+}$ as the major product detected by UV-vis spectroscopy (Figure 3.2, Method 3). After purification by cation exchange chromatography, the complex was isolated in typical yields of 4 to 8%. Longer or higher temperature reaction conditions were found to favor an unknown purple colored side product and significantly reduced the yield. Shorter and lower temperature conditions were found to inhibit the reaction substantially. The product obtained from each of the three methods was fully characterized by UV-visible, infrared, and electron paramagnetic spectroscopies, cyclic voltammetry, and X-ray crystallography.

3.3 Characterization results and discussion

3.3.1 X-ray crystallography[3]

Diffraction quality crystals of $[Ru(NH_3)_5Cl]Cl_2$ were grown from slow evaporation of 2 M HCl solutions obtained from the cation exchange chromatography. $[Ru(NH_3)_5Cl]Cl_2$ crystallized into yellow blocks in the orthorhombic space group P*nma* (Table 3.1). The dichloride salt X-ray structure has only been recently published by this author; the analogous copper oxalate salt was published in 2014 by Martynova and co-workers.[223,272] The Ru–N and Ru–Cl bond distances are comparable for both compounds, as expected, although the space groups were not the same. A crystallographic mirror plane bisects the N3-Ru-Cl plane; positional disorder is apparent in the hydrogens on N1, N2, and N3 (Figure 3.3a).

[3]Thanks to Samantha N. MacMillan for all crystal structure data collection and refinement.

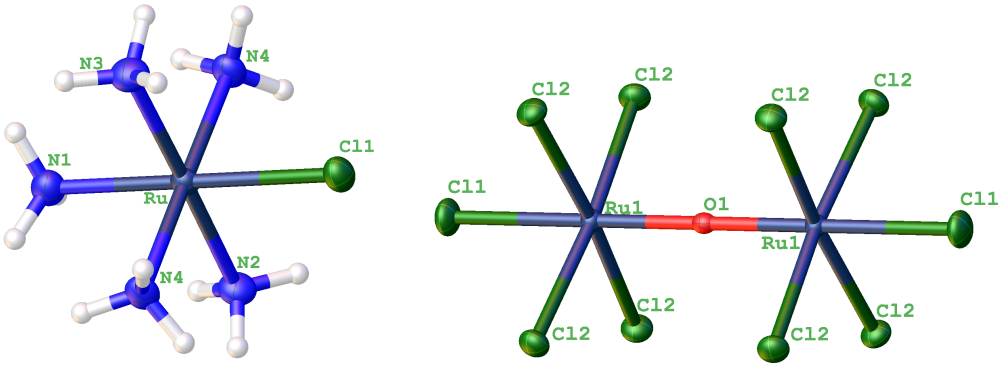

(a) (b)

Figure 3.3: The X-ray crystallographic structures of (a) $[Ru(NH_3)_5Cl]Cl_2$ and (b) $[Ru_2OCl_{10}]^{4-}$ grown from slow evaporation of 2 M and 2.5 M HCl solutions at room temperature and elevated temperature, respectively. Thermal ellipsoids are at the 50% probability level. Reproduced with permission from *Inorg. Chem.*, **2017**, 56(6), pp 3123 - 3126. Copyright 2017, American Chemical Society.

The synthesis and X-ray structure of $[Ru_2OCl_{10}]^{4-}$ has been reported previously.[268] Due to limited methods for characterization we obtained the X-ray crystal structure and powder X-ray diffraction to verify identity and purity (Figure 3.3b and A.1). Slow evaporation at 50 °C of a 2.5 M HCl solution of $[Ru_2OCl_{10}]^{4-}$ produced red blocks of good quality in the highly symmetric tetragonal space group $I4/mmm$. The space group and bond lengths and angles matched those of the previously reported crystal structure.[268] The Ru-O-Ru bond is bisected by two perpendicular mirror planes and a third mirror plane sits through the oxygen, generating the exactly 180° Ru-O-Ru bond. The simulated powder diffraction was calculated using Mercury based on the crystal structure and compared to the experimental data — good agreement indicated that the bulk sample was pure (Figure A.1).

Crystals grown from solutions of **3.1** exhibited two different polymorphic forms. The vapor diffusion of ethanol into aqueous solutions yielded dark red prisms (see Figure 3.4a), whereas the slow evaporation of 3 M HCl solutions gave rise to green dichroic needles (see Figure 3.4b). Analysis of the red prisms revealed an oxo-bridged dinuclear Ru structure of

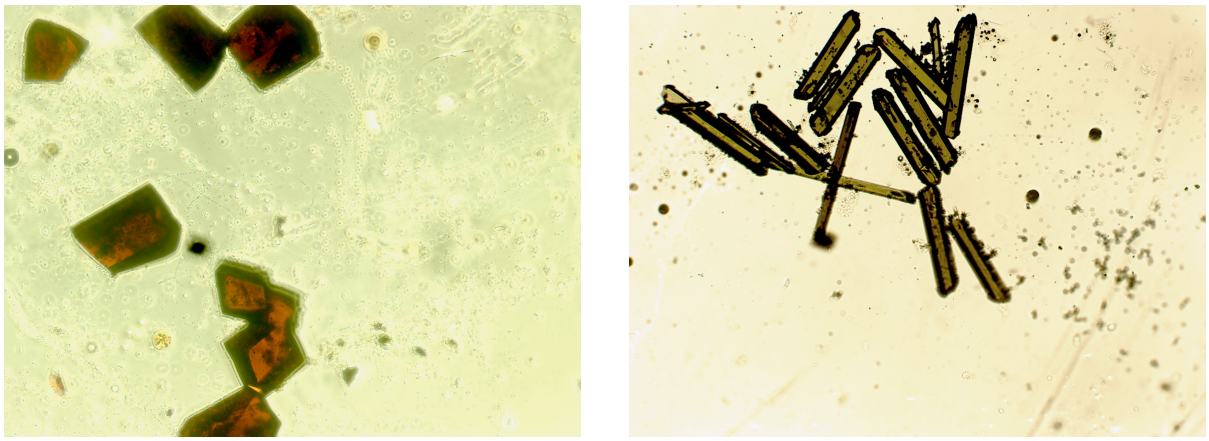

(a) (b)

Figure 3.4: (a) The red polymorph grown from ethanol diffusion into aqueous solutions of **3.1**. (b) Green polymorph obtained from slow evaporation of 3 M HCl solutions of **3.1**

the formula $[(OH)(NH_3)_4Ru(\mu-O)Ru(NH_3)_4(OH_2)]^{4+}$ (Figure 3.5, Table 3.1[4]). This formula differs from that of $[(OH_2)(NH_3)_4Ru(\mu-O)Ru(NH_3)_4(OH_2)]^{5+}$ by the loss of one equivalent of HCl to give a mixed aqua-hydroxo compound. The bridging μ-oxo-ligand sits on a crystallographic inversion center. Thus, the ammine ligands assume an eclipsed conformation, and the Ru-O-Ru angle is exactly 180°.

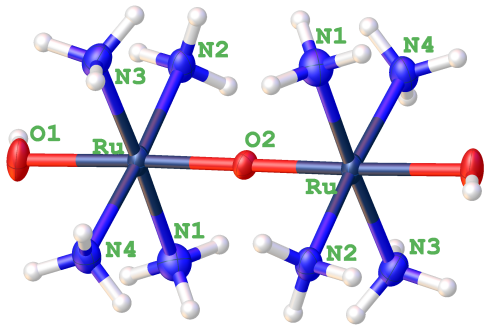

Figure 3.5: The solid state structure of $[(OH)(NH_3)_4Ru(\mu-O)Ru(NH_3)_4(OH_2)]^{4+}$, grown from ethanol diffusion into aqueous solutions. Thermal ellipsoids are at the 50% probability level. Reproduced with permission from *Inorg. Chem.*, **2017**, 56(6), pp 3123 - 3126. Copyright 2017, American Chemical Society.

[4]Relevant bond distances and angles in Appendix A.

Such geometric features are also present in the formate-capped Ru360 ion, which lies on both a crystallographic inversion center and mirror plane[119,233]. Based on hydrogen-bonding patterns in the lattice (*vide infra*), we assign the axial ligands as water and hydroxide. However, only one hydrogen atom could be conclusively identified in the difference Fourier map. Inspection of intermolecular interactions between axial oxygen ligands on neighboring cations reveals the presence of a close contact of 2.446 Å (Figure 3.6). These two oxygen atoms are related by a crystallographic inversion center; in addition, the distance between atoms is too short to constitute a normal hydrogen bonding interaction. We hypothesize that this situation represents a symmetric hydrogen bond where the hydrogen atom is shared equally between both donor oxygen atoms.

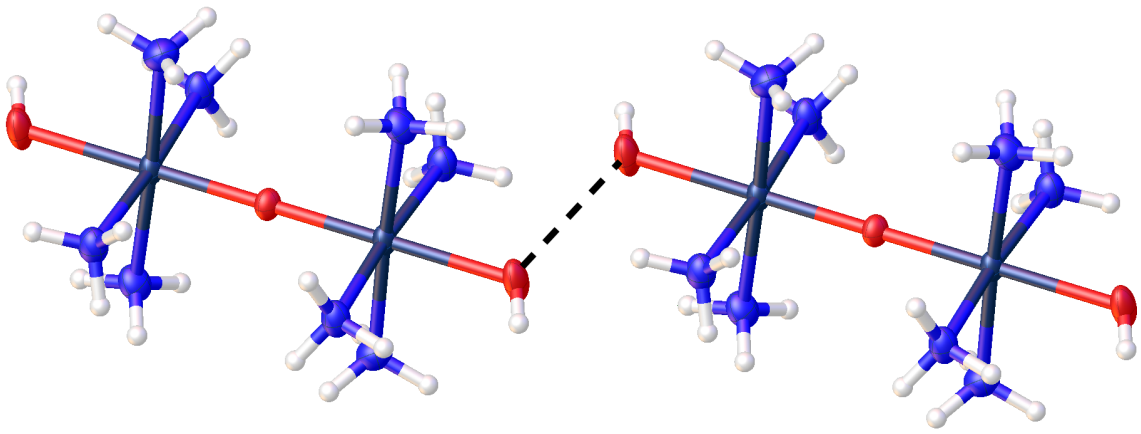

Figure 3.6: Intermolecular symmetric hydrogen bond interaction between axial ligands of $[(OH)(NH_3)_4Ru(\mu-O)Ru(NH_3)_4(OH_2)]^{4+}$. Thermal ellipsoids are at the 50% probability level. Reproduced with permission from *Inorg. Chem.*, **2017**, 56(6), pp 3123 - 3126. Copyright 2017, American Chemical Society

This hydrogen atom, which could not be located in the difference Fourier map, is inferred to lie on the crystallographic inversion center at the midpoint of the symmetric hydrogen bond. Accounting for this shared hydrogen atom, the net formula for the complex cation in the solid state is $[(OH)(NH_3)_4Ru(\mu-O)Ru(NH_3)_4(OH_2)]^{4+}$. Four outer-sphere chloride ions are also present (not shown in figures). The net balance of the charge, accounting for

the hydrogen atom on the inversion center, results in the expected mixed-valent Ru^{III}/Ru^{IV} oxidation state, which is well characterized for Ru360.[233]

Table 3.1: X-ray Crystallographic Data Collection and Refinement Parameters for $[Ru(NH_3)_5Cl]Cl_2$, $K_4[Ru_2OCl_{10}]$ and $[(OH)(NH_3)_4Ru(\mu-O)Ru(NH_3)_4(OH_2)]Cl_4$

Crystal Data	$[Ru(NH_3)_5Cl]Cl_2$	$K_4[Ru_2OCl_{10}]$	$[(HO)(NH_3)_4Ru(\mu-O)Ru(NH_3)_4(OH_2)]Cl_4$
Formula Weight	292.59	729.04	530.23
Temperature/K	223	223	223
Crystal System	Orthorhombic	Tetragonal	Monoclinic
Space Group	Pnma	I4/mmm	P$2_1/n$
a/Å	13.3791(12)	7.0951(13)	8.2808(5)
b/Å	10.5086(8)	7.0951(13)	11.7183(7)
c/Å	6.7456(6)	17.034(4)	9.0833(5)
$\alpha/^\circ$	90	90	90
$\beta/^\circ$	90	90	96.612(3)
$\gamma/^\circ$	90	90	90
Volume (Å^3)	948.40(14)	857.5(4)	875.55(9)
Z	4	2	2
D, g cm^{-1}	2.049	2.824	2.011
μ (mm^{-1})	2.438	4.266	2.334
Observed reflections	1288	462	2171
Parameters	53	20	86
R1 (I $>2\sigma$)^a	0.0241(1166)	0.0228(408)	0.0265(1995)
wR2 (I$>2\sigma$)^b	0.0608(1288)	0.0547(462)	0.0655(2171)
GOF^c	1.099	1.124	1.091

^{a}R1 $= \Sigma||F_o|-|F_c||/\Sigma|F_o|$. ^{b}wR2 $= \{\Sigma[w(F_o^2 - F_c^2)^2]/\Sigma[w(F_o^2)^2]\}^{1/2}$.
^{c}GOF $= \{\Sigma[w(F_o^2 - F_c^2)^2]/(n-p)\}^{1/2}$.

The green needle polymorph (Figure 3.4b, Table 3.2) of this compound gave data that appeared suitable for X-ray diffraction. Although initial structure solution was successful, full refinement of the structure was hindered by unresolved twinning issues.

Table 3.2: Unit Cell Parameters and Tentative Space Group Assignment for the Green Polymorph

	Crystal Data
Morphology	Needle
Crystal System	Monoclinic
Space Group	$P2_1/c$
Volume/ Å^3	3464
a/Å	14.51
b/Å	9.23
c/Å	26.40
$\alpha/^\circ$	90
$\beta/^\circ$	101.72
γ°	90

Basic atomic connectivity obtained from this data, however, revealed a structure largely similar to that of the red polymorph. Namely, a linear Ru-O-Ru complex with axial ligands believed to be oxygen-atom donors based on the electron density contributions of the difference map and the interatomic distances. This structure suggests that even in 3 M HCl, chloride ions do not bind directly to the axial sites.

3.3.2 UV-visible and infrared spectroscopy

Compound **3.1** was further characterized by UV-visible (UV-vis) and infrared (IR) spectroscopy. The UV-vis absorption spectrum revealed a diagnostic absorbance band centered at 360 nm, a feature which gives Ru360 its name (Figure 3.7 and Table 3.3). A lower energy transition centered at 600 nm gives rise to the observed green color of these compounds in solution. The intensity of this transition varied slightly depending on the synthetic method used to prepare the complex. The variance between the different preparations is tentatively attributed to the presence of small quantities of the RuRed ion, which has a large molar absorptivity (68,000 M^{-1} cm^{-1}) at 530 nm. The UV-vis spectrum is pH dependent, presum-

Table 3.3: Extinction coefficients for the three synthetic methods taken in pH 7.4 phosphate-buffered saline (PBS)

Absorption wavelength	Method 1	Method 2	Method 3
360 nm [$M^{-1}cm^{-1}$]	27000 ± 6000	26000 ± 3000	28000 ± 4000
600 nm [$M^{-1}cm^{-1}$]	430 ± 310	850 ± 90	780 ± 100
1180 nm [$M^{-1}cm^{-1}$]	180 ± 10	99 ± 14	125 ± 14

ably due to the degree of protonation of the axial aquo ligands. For the previously prepared aqua- and hydroxo-capped analogues, the absorbance maxima are at 335 and 593 nm at pH 2, and 360 and 612 nm at pH 9, respectively.[233] We found at pH 7.4 the axial ligands are most like fully protonated (aqua-capped), based on the similarity between the acquired spectra and the previously reported spectra.[233]

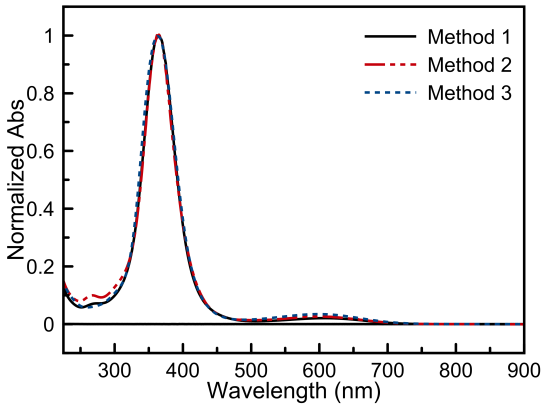

Figure 3.7: The UV-vis spectrum of all three preparations methods for compound **3.1**. Reproduced with permission from *Inorg. Chem.*, **2017**, 56(6), pp 3123 - 3126. Copyright 2017, American Chemical Society.

Consideration of the molecular orbital diagram and DFT analysis clarifies the mixed-valence character of the system and the transitions observed in the UV-vis spectrum. The molecular orbital (MO) diagram for dinuclear ruthenium μ-oxo bridged species was originally developed using $K_4[Ru_2OCl_{10}]$, and further adapted to study the blue dimer, ($[Ru_2O(bpy)_4](PF_6)_2$), $[Ru_2O(NH_3)_{10}]^{4+/5+}$, as well as other mixed-valent compounds.[273–277]

Following the example laid down by Orgel and co-workers, the ruthenium centers each can be considered C_{4v} symmetry and will transform as $3a_1+a_1+a_2+2a$.[273] The ammines and aquo ligands are sigma donors, and therefore will transform as $2a_1+a_1+a$ and the μ-oxo σ-bond will transform as A_1. This leaves a_2 and a as the orbitals to form the π-bonds. Considering the entire molecule ($C_{4v} \times i = D_{4h}$), this leads to an energy level ordering of $(e_u^b)(b_{2g})(b_{2u}(e_g)(e_u^a)$ (Figure 3.8a). The total number of electrons is 13: 9 from the two ruthenium atoms and 4 from the x and y orbitals of the oxygen. Filling up the MO diagram leaves one electron unpaired in the e_u^a orbital. The molecular orbital generation, and the energy level ordering is corroborated by DFT calculations (Figure 3.8a).

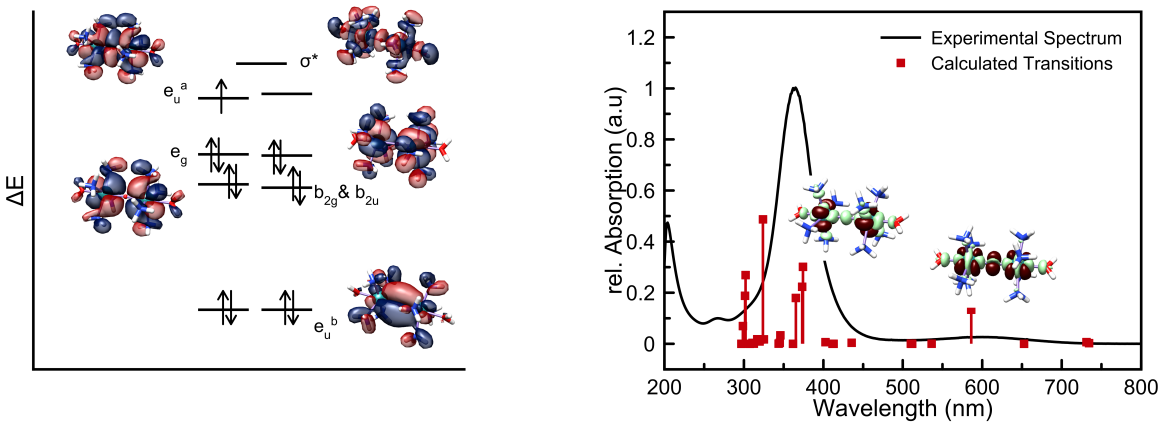

(a) (b)

Figure 3.8: (a) The MO diagram (π system only) with symmetry assignments and DFT calculated density orbitals. Energy levels from DFT calculations. (b) The calculated UV-vis transitions by TDDFT analysis compared with the experimental. Electronic transitions illustrated as going from dark red to light green.

Thus, a III/IV system will be paramagnetic, a III/III system will be paramagnetic and a IV/IV system will be diamagnetic (Figure 3.8a). TDDFT analysis of **3.1** revealed the 360 nm band to be a LMCT with charge density going from the ammine and aquo ligands to the ruthenium metal centers. The 600 nm band is the HOMO π^* (e_u^a) to σ^* electronic transition (Figure 3.8b).

In the infrared spectrum, the ammine N–H vibrational modes dominate, visible at 3200, 1618, and 1313 cm^{-1} (Figure 3.9a and Table 3.4).

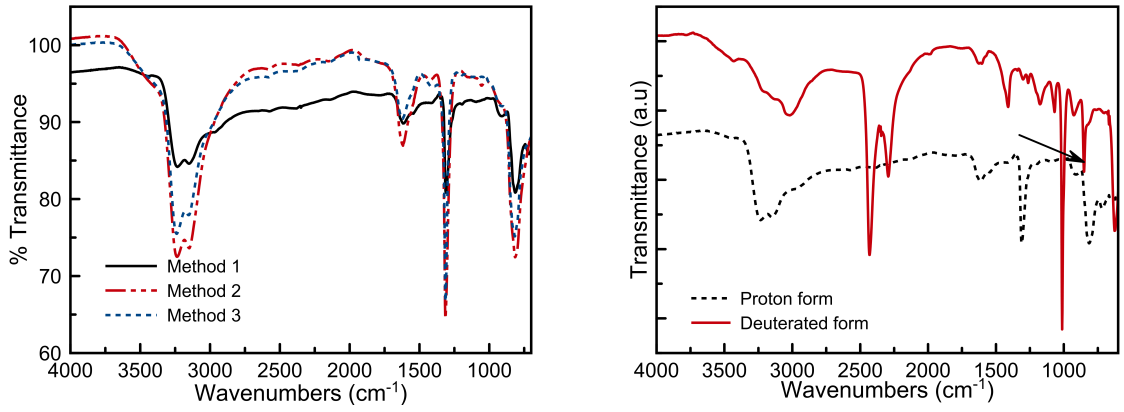

(a) (b)

Figure 3.9: The IR (a) of all three preparations methods for compound **3.1**. The IR spectra from deuterated **3.1** (b) showing the Ru-O-Ru vibrational mode (black arrow). Reproduced with permission from *Inorg. Chem.*, **2017**, 56(6), pp 3123 - 3126. Copyright 2017, American Chemical Society.

The Ru-O-Ru stretching mode resonates at 850 cm^{-1}; this mode was identified by deuterium isotopic labeling of the NH_3 ligands to shift these vibrational frequencies to lower energies (Figure 3.9b). The isotopic labeling was accomplished by dissolving compound **3.1** in D_2O to exchange the ammine and aquo protons for deuterium and then lyophilizing the solvent. The Ru-O-Ru value (850 cm^{-1}) differs only slightly from that for $K_4[Ru_2OCl_{10}]$, which is reported at 888 cm^{-1}.[278–280]

Table 3.4: Infrared spectroscopy vibrational frequencies for $[Ru(NH_3)_5Cl]Cl_2$ and compound **3.1**, in proton form and deuteron form. Qualitative assignments: s = strong, m = medium, w = weak, sh = shoulder, bd = broad.

$[Ru(NH_3)_5Cl]Cl_2$	$[Ru_2O(NH_3)_8(H_2O)_2]Cl_5$	$[Ru_2O(ND_3)_8(D_2O)_2]Cl_5$
3213 (m)	3500 (sh)	
1608 (m)	3234 (m)	
1298 (s)	3149 (m)	3016 (m, bd)
798 (s)		2432 (s)
		2293 (m)
	1618 (w)	1625 (w)
	1313 (s)	1409 (w)
		1176 (w)
		1068 (w)
		1012 (s)
		927 (w)
	815 (s, bd)	850 (m)
		626 (m)

The $[(OH_2)(NH_3)_4Ru(\mu-O)Ru(NH_3)_4(OH_2)]^{5+}$ symmetric and asymmetric N-H stretches (3300 to 3100 cm^{-1}) shift to lower frequencies as expected (2450 to 2300 cm^{-1}).[264,269,276] The shoulder at ~3500 cm^{-1} shifts to 3016 cm^{-1} and can be assigned as the coordinated H_2O. The bending vibration occurs at 1313 cm^{-1} and shifts to 1012 cm^{-1}. The small vibrational modes between 1200 and 900 cm^{-1} are most likely due to incomplete deuteration. The vibration at 1618 cm^{-1} shifts to 1409 cm^{-1} and can be assigned as another N-H bending mode.

3.3.3 Cyclic voltammetry, electron paramagnetic resonance and near-infrared spectroscopy

To further explore the mixed-valent character of this complex we employed cyclic voltammetry (CV), electron paramagnetic resonance (EPR), and near-infrared (NIR) spec-

troscopies. Cyclic voltammetry of $[(OH_2)(NH_3)_4Ru(\mu-O)Ru(NH_3)_4(OH_2)]^{5+}$ in 0.10 M, pH 7.6 NH_4HCO_2 buffer afforded two electrochemical processes (Figure 3.10a). Two sequential quasi-reversible reductions, representing transitions to the [IV,IV]/[III,IV] and [III,IV]/[III,III] couples, are present at $E_{1/2}$ = +0.12 V and $E_{1/2}$ = –0.42 V, respectively. The assignments are based on the resting potential of the complex, assigned as the mixed valent [III/IV]. The [IV,IV]/[III,IV] and [III,IV]/[III,III] potentials fall between those measured previously for the aqua- and hydroxo-capped analogues, which were measured at pHs of 2 and 8.15[233]. The comproportionation constant, K_c, which reflects the stability of the mixed-valent state, is calculated to be 3.0×10^{10} for the [III,IV] state based on the 620 mV separation between the [IV,IV]/[III,IV] and [III,IV]/[III,III] couples.[281]

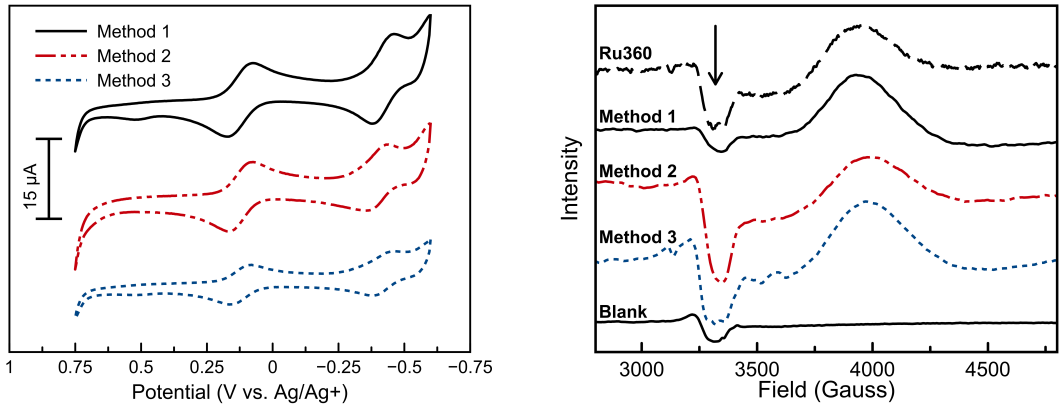

(a) (b)

Figure 3.10: The (a) CV of all three preparation methods for compound **3.1** in pH 7.6, 0.10 M NH_4HCO_2 buffer. (b) EPR spectra of all three preparations for compound **3.1** at 77 K. The arrow indicates an intensity dip due to paramagnetic impurities in the instrumental cavity. Reproduced in part with permission from *Inorg. Chem.*, **2017**, 56(6), pp 3123 - 3126. Copyright 2017, American Chemical Society.

X-band EPR spectroscopy of $[(OH_2)(NH_3)_4Ru(\mu-O)Ru(NH_3)_4(OH_2)]^{5+}$ (Figure 3.10b) at 77 K reveals a broad signal at g = 1.69, consistent with a paramagnetic Ru^{III}/Ru^{IV} mixed-valent ground state. Although the Ru^{III}/Ru^{III} is also paramagnetic, previous work on the Ru^{III}/Ru^{III} blue dimer revealed that this oxidation state is EPR silent. A Loretnzian

fit of the signal gives a width of 136 G; the classic EPR derivative lineshape was not observed. The broad line shape was likely due to a shorter than normal relaxation times.[282] The width of the signal is consistent with other reported diruthenium bridged systems. The Creutz-Taube ion contains a bridging pyrazine and has a temperature dependent linewidth ranging from 120 G at 2 K to 350 G at 200 K.[283] Mixed-valent oxo-bridged Ru^{III}/Ru^{IV} complexes bearing polypyridyl ligands display broad signals ranging from g = 1.39 to 1.79 (no line widths reported), which are also consistent with our observation for $[(OH_2)(NH_3)_4Ru(\mu{-}O)Ru(NH_3)_4(OH_2)]^{5+}$.[284–286] Oddly, the EPR signal of Ru360 reported by Emerson and co-workers was reported to be an absorption at g = 2.06.[283] $RuCl_3$ has an EPR signal at g = 2.09, potentially indicating a contamination in the reported spectra.

A NIR transition, centered at 1180 nm (8480 cm^{-1}), arises from the intervalence charge transfer (IVCT) associated with this mixed-valent complex.[287] The high comporportionation constant determined from the CV, would suggest a Class III, fully delocalized, system based on the Robin and Day classifications, however more precise analysis can be done.[231] The reorganization energy, λ can be calculate using the full-width half-max of the transition. (Equation 3.1).[287,288] This is a term describing the free energy difference between DBA and ABD, where DBA is the donor state and ABD is the acceptor state.[287]

$$\Delta\overline{\nu}_{1/2} = [2310\lambda]^{1/2} \tag{3.1}$$

The degree of delocalization can be established by calculating H_{ab} for the transition. H_{ab} is a parameter describing the electronic interaction between the donor and acceptor states. It can be calculated using the extinction coefficient of the transition (ϵ), the distance between the donor and acceptor atom (r_{ab}), the transition maximum and full-width half-max:

$$H_{ab}^2 = \frac{\epsilon_{\max}\nu_{\max}\Delta\overline{\nu}_{1/2}}{2.36\times10^3 r_{\mathrm{ab}}^2}. \tag{3.2}$$

Comparison between λ and H_{ab} gives an easy way to establish the class of the IVCT transi-

tion. Using

$$\Gamma = 1/2 - (\lambda - 2H_{ab})/\Delta\overline{\nu}_{1/2},$$

between $0 < \Gamma < 0.1$ is Class I, $0.1 < \Gamma < 0.5$ is Class II, and $\Gamma > 0.5$ is Class III (Table 3.5).

Table 3.5: Near-IR calculations to determine the extent of delocalization for compound **3.1**, all three synthetic methods.

	FWHM [cm^{-1}]	λ [cm^{-1}]	H_{ab} [cm^{-1}]	Γ [cm^{-1}]
Method 1	1069	494	229	0.47
Method 2	1165	587	177	0.30
Method 3	1146	568	197	0.35

Based on this analysis the compound has a Class II assignment; this is also corroborated by the low extinction coefficients of the complex.

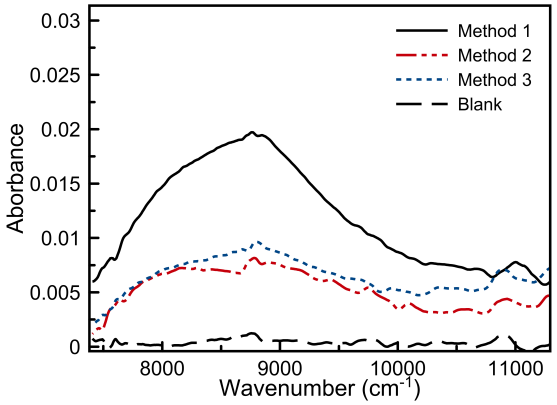

Figure 3.11: The near-IR spectra of all three preparation methods.

3.3.4 Aqueous stability

The biological activity of compound **3.1** will be discussed in Chapter 5. However, previous reports suggest lack of aqueous stability for Ru360 and RuRed[233,243,263]. To ensure aqueous

stability under the working conditions of our aqueous stock solution, the freeze-thaw stability and long-term stability was analyzed by UV-vis spectroscopy.

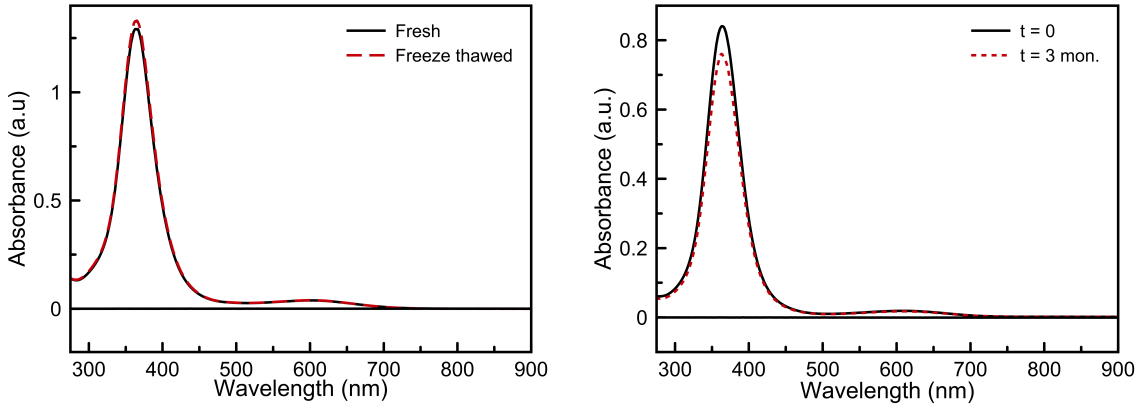

(a) (b)

Figure 3.12: The freeze-thaw stability (a) over several cycles and the long term frozen stability (b) of the Ru360 analog. Reproduced with permission from *Inorg. Chem.*, **2017**, 56(6), pp 3123 - 3126. Copyright 2017, American Chemical Society

The spectra did not significantly change after five freeze-thaw cycles over five days, with a freezer temperature of -20 °C and stock solutions prepared in MilliQ 18 MΩ·cm water. Additionally, a stock solution that was kept at -80 °C for three months was determined to be greater than 90% pure.

In addition, the stability in the biologically relevant reducing agent, glutathione, and the stability in cell growth media (DMEM with 10% FBS) was probed by EPR spectroscopy. Compound **3.1** was incubated at 37 °C for 24 hours in either 5 mol equivalents of glutathione, or in cell growth media for 24 hours. The change in the presence of glutathione was significant (Figure 3.13a). Compound **3.1** (evident as the broad signal at ∼4000 G, t = 0) was no longer observed after 24 hours. The reaction also proceeded quickly, as the peaks at 2500 Gauss at t = 0 began to form in the time needed to prepare the sample. The absorptions below 3500 Gauss are consistent with Ru^{III} EPR signals.[289–291] Similarly, in cell growth media an absorption grows in at ∼ 2500 Gauss, most likely a Ru^{III} species (Figure 3.13b). These

two studies indicate that compound **3.1** was not significantly stable in biologically relevant solutions.

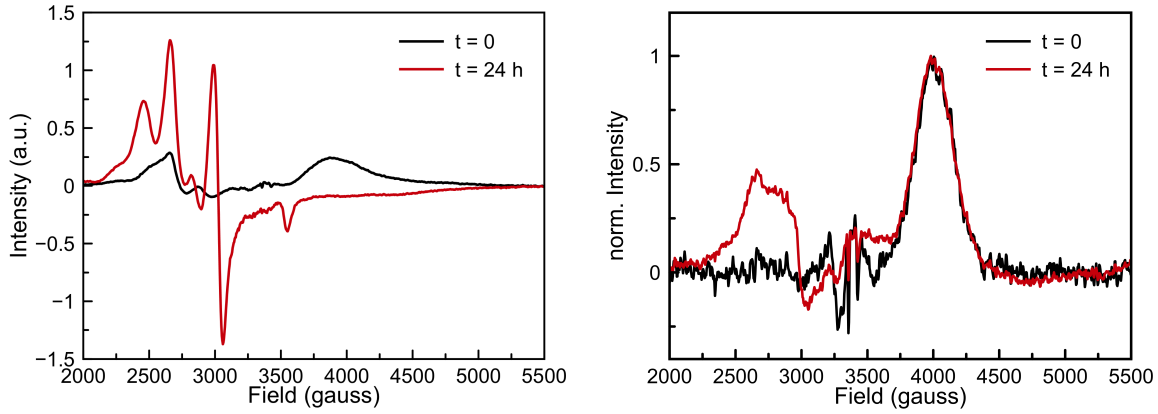

(a) (b)

Figure 3.13: (a) The stability of compound **3.1** in 5 mol equivalents glutathione after 24 h incubation. (b) The stability of compound **3.1** in DMEM containing 10% fetal bovine serum after 24 h incubation.

3.4 Conclusion

In summary, the synthesis and characterization of a structural and functional analogue of Ru360 is described. This compound was prepared via three different synthetic routes and characterized by UV-vis spectroscopy, IR spectroscopy and X-ray crystallography. The two newly developed synthetic methods may be more broadly applicable for the preparation of new complexes with the Ru-O-Ru core, facilitating the discovery of new potent inhibitors of the MCU based on ruthenium. This system is consistent with a delocalized mixed-valent species, based on EPR spectroscopy, cyclic voltammetry and near-IR spectroscopy. Analysis of the near-IR data establishes the compound as a Class II complex. DFT calculations revealed additional insight into the molecular orbital diagram and the nature of the UV-vis transitions. This species was found to be stable under long-term cold storage, but was unstable in biologically relevant solutions. Future directions for this compound include

exploring axial ligand substitutions as well as different equatorial ligands to build a library of complexes.

CHAPTER 4

SYNTHESIS AND CHARACTERIZATION OF μ-NITRIDO RUTHENIUM COMPLEXES

4.1 Introduction

The best-characterized inhibitor of the MCU is the dinuclear oxo-bridged ruthenium complex Ru360, $[(HCO_2)(NH_3)_4Ru(\mu\text{-}O)Ru(NH_3)_4(O_2CH)]^{3+}$.[119,233,243] The mechanism by which this compound inhibits the MCU, however, is not well understood, and therefore the structural features that give rise to its MCU-inhibitory properties are still under investigation. Studies of MCU inhibitors frequently use of Ruthenium Red (RuRed) or Ru360 as discussed in Chapters 2 and 5. We showed that substitution of the axial formate groups on Ru360 with axial waters greatly enhanced the inhibitory efficacy (see Chapter 3).[223] This finding suggests that the ligand environment around the Ru-O-Ru core has a significant effect on the compound's activity. Additionally, a relatively unique structural feature of Ru360 that may contribute to its biological activity is its linear Ru-O-Ru core. A similar albeit less common motif is the linear bridging nitrido core, Ru-N-Ru, which is observed in a smaller subset of compounds.[292–305] However, the biological activity for this class of compounds has not been explored. Due to the structural similarity to Ru360, and therefore the possibility of biological activity, we set out to synthesize and characterize dinuclear ruthenium complexes with the bridging nitrido motif.

Two major synthetic methods have been used to access μ-nitrido diruthenium complexes. The first involves the well characterized compound, $K_3[Ru_2NCl_8(H_2O)_2]$ (**4.SM2**) as a general synthon, which is can be transformed via direct ligand substitution of the chlorides.[293–295] Previously explored ligands using this method include dithiocarbamates, bipyridines, and ammines. The second method utilized ruthenium azide complexes with the ligands already

installed and are decomposed to release N_2, forming the μ-nitrido complex. This method was applicable for the synthesis of a variety of ligand substitutions, including *o*-benzoquinone, porphyrin and mercapto-phenylthio complexes.[300–305] The ammine, ethylenediamine (en), and 2,2'-bipyridine (bpy) substitutions were synthesized in the initial reports of Ru-N-Ru complexes[293,294]; however, they were only characterized using infrared spectroscopy and elemental analysis. A later report provided the X-ray crystal structure of the en substituted complex, which revealed a bridging en group between the two ruthenium atoms.[295]

Herein we report the syntheses of the ammine (**4.1**), en (**4.2**), bpy (**4.3**), 4,4'-dimethyl-2,2'-bipyridine (**4.4**) and 4,4'-dimethoxy-2,2'-bipyridine (**4.5**) complexes starting from **4.SM2** with full characterization by UV-vis, infrared, nuclear magnetic resonance spectroscopies, and small-molecule X-ray crystallography. **4.1** and **4.2** were also characterized by conductivity[1]; this could not be performed on compounds **4.3**, **4.4** and **4.5** due to lack of aqueous solubility. The kinetics of aquation for compounds **4.1** and **4.2** are also reported. The corresponding biological activity of these complexes is reported in Chapter 5.

4.2 Synthesis and purification[2]

We utilized previously reported syntheses for compounds **4.SM1**[306] and **4.SM2**[293,307] with minor modifications (Scheme 4.1). Synthesis of $K_2[RuCl_5NO]$(**4.SM1**) was achieved by refluxing $RuCl_3 \cdot n\,H_2O$ with K_2NO_2 in 0.5 M HCl, followed by addition of KCl and additional refluxing. Pure dark pink-purple microcrystalline product was obtained (48% yield) after evaporation of the solvent. $K_3[(H_2O)Cl_4Ru(\mu\text{-}N)RuCl_4(H_2O)]$ (**4.SM2**) was obtained by treatment of the aforementioned ruthenium nitrosyl with $SnCl_2$ in HCl at reflux for an hour.

[1]This is the electrolytic conductivity, and is also referred to sometimes as the specific conductance. However, for ease of this discussion it will simply be referred to as conductivity.

[2]Experimental details can be found in Appendix B.

Evaporation of the solvent afforded the product as red-brown crystals (38% yield).

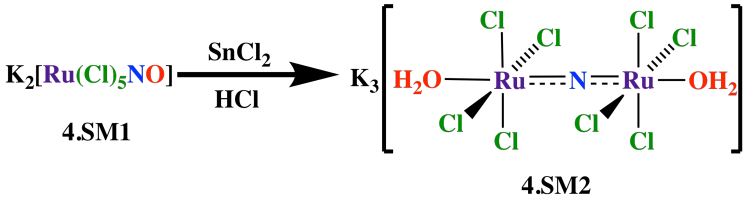

Figure 4.1: Synthetic scheme for the formation of **4.SM2** from **4.SM1**. Compound **4.SM1** was generated from $RuCl_3 \cdot n\,H_2O$ in the presence of acidic KNO_2.

For characterization of these two products, the diagnostic IR spectroscopy and X-ray crystal structure data was used. Crystals of **4.SM1** were obtained by slow evaporation of an aqueous solution; the unit cell matched the previously reported structure.[308] Compound **4.SM2** formed diffraction quality crystals by HCl diffusion into an aqueous solution; all X-ray crystallographic parameters matched those previously reported (Figure 4.2a, Table 4.1, Table B.2)).[309,310] IR spectroscopy of the ammonium salt of **4.SM1** contained the diagnostic NO stretch at 1894 cm^{-1} (Figure 4.2b).[306] In addition, IR spectroscopy of **4.SM2** showed the diagnostic asymmetric Ru-N-Ru stretch at 1078 cm^{-1} (Figure 4.2b), consistent with previously reported values.[294] IR spectroscopy proved to be a useful tool for the characterization of these complexes because of the characteristic Ru-N-Ru IR stretch. These values typically range between 1000 and 1100 cm^{-1}.[297,310,311]

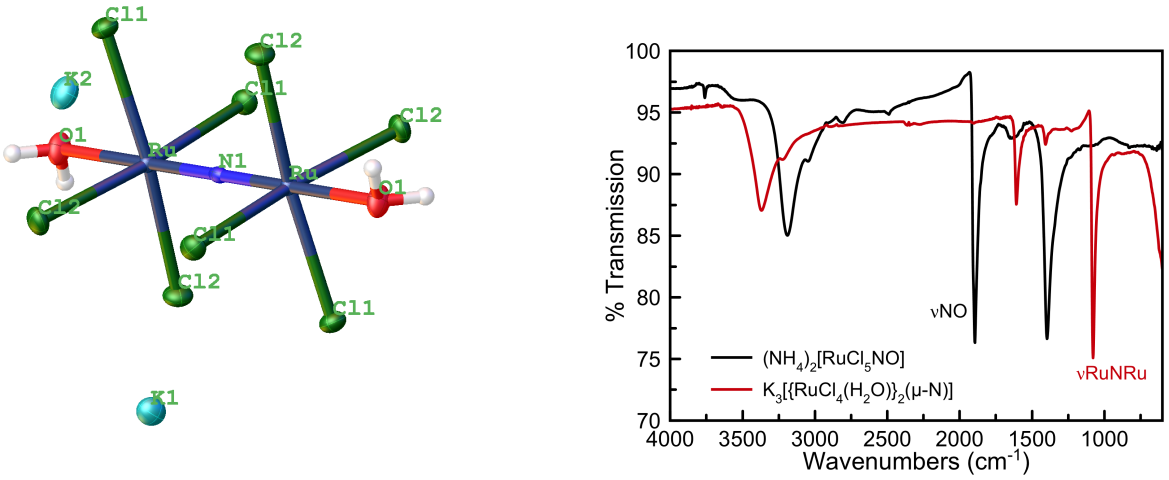

(a) (b)

Figure 4.2: The X-ray crystal structure of (a) **4.SM2** and (b) infrared spectra of **4.SM1** and **4.SM2**.

Heating **4.SM2** in concentrated ammonia (d = 0.88) for six hours resulted in the substitution of the equatorial chlorides with NH_3 afforded an orange solution (Scheme 4.3). After rotary evaporation, the addition of concentrated HCl to an aqueous solution of the crude compound yielded a pale orange compound after cooling the solution overnight. Recrystallization of this crude material by acetone diffusion into aqueous solutions yielded pure **4.1** with elemental composition consistent with 8 NH_3, 2 Ru, 5 Cl, 1 N and 1.5 H_2O. This procedure varied slightly from the previously reported synthesis; the reaction is heated for a longer period of time and was recrystallized from acetone after the initial HCl precipitation. Compound **4.1** was found to be somewhat soluble in water and poorly soluble in DMSO; gentle heating and sonication facilitated dissolution.

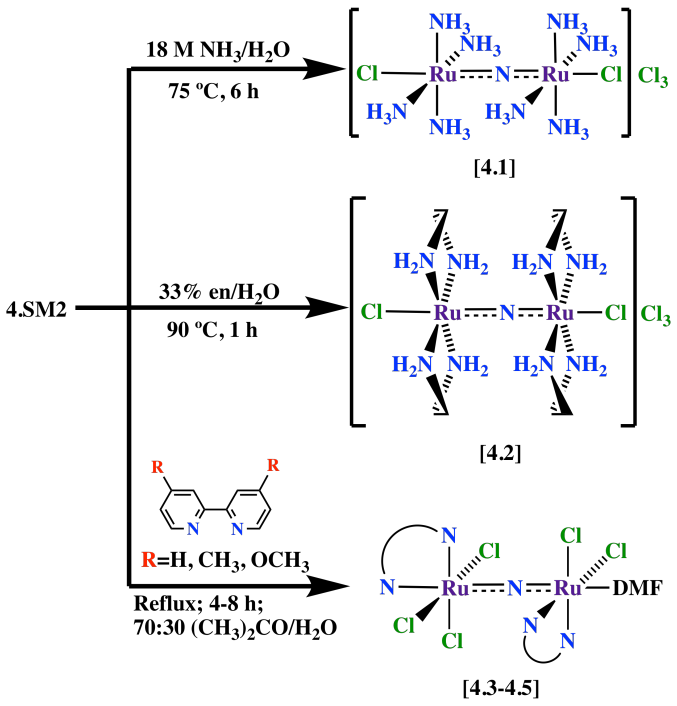

Figure 4.3: Synthetic scheme for **4.1**-**4.5** from **4.SM2**.

Similarly, dissolving **4.SM2** in 33% aqueous ethylenediamine (en) for one hour results in the substitution of the equatorial chlorides with four en ligands to form compound **4.2** (Scheme 4.3). Isolation of the complex was achieved by precipitation with copious ethanol, centrifugation, reconstitution with water and recrystallization with the addition of concentrated HCl to form the pure product in 28% yield. Compound **4.2** was found to be poorly soluble in water and insoluble in organic solvents. Single crystals as needles were grown from diffusion of HCl vapors into aqueous solutions of **4.2**.

A previously described reaction of **4.SM2** with bpy reportedly gave the cation $[Ru_2N(bpy)_4(Cl)_2]^{3+}$, which was characterized only by IR spectroscopy and elemental analysis.[294] [3]Substitution with 2,2'-bipyridines was affected by treatment with an excess of 2,2'-bipyridine (bpy), 4,4'-dimethyl-2,2'-bipyridine (dmbpy), and 4,4'-dimethoxy-2,2'-bipyridine (dmobpy) in an acetone-water mixture to form crude compounds **4.3**, **4.4** and **4.5**, respec-

[3]Thanks to Julie Urgiles for performing the synthesis and characterization of these complexes.

tively. Upon recrystallization of the crude products from *N,N*-dimethylformamide (DMF), red crystals of each compound were isolated in 16%, 3.5% and 5.3% yield, respectively. The low yields are attributed to the low solubility of the complexes in DMF and a variety of side products that could not be isolated in pure form. Yields could be increased by additional extraction from the crude DMF mixture as discussed in the experimental section in Appendix B.

4.3 Characterization results and discussion[4]

4.3.1 X-ray crystallography

Single crystals of **4.1** suitable for X-ray diffraction were extremely difficult to grow; the complex is only minimally soluble in water and DMSO. Crystallization attempts from many different solvent systems yielded either microcrystals or powders. Initial formation of diffraction quality crystals was achieved by treatment of the complex with excess $AgBF_4$ to form the $BF_4{}^-$ salt. After filtration to remove AgCl, ethanol diffusion into the solution afforded single crystals. However, the X-ray structure indicated the counterion was the octahedral $SiF_6{}^{2-}$, as apposed to the expected tetrahedral $BF_4{}^-$. This unexpected counterion swap has been previously reported for a platinum complex.[312] The $BF_4{}^-$ anion can hydrolyze to form HF, which then can further react with SiO_2 in the glass reaction vessel to form $SiF_6{}^{2-}$. The intentional treatment of an aqueous solution of **4.1** with $(NH_4)_2SiF_6$ followed by ethanol diffusion afforded crystals (**4.1SiF6**, Figure 4.4a), with the same structure as the "accidental" formation, confirming the identity of the $SiF_6{}^{2-}$ counterions.

[4]Relevant bond distances and angles in Appendix B.

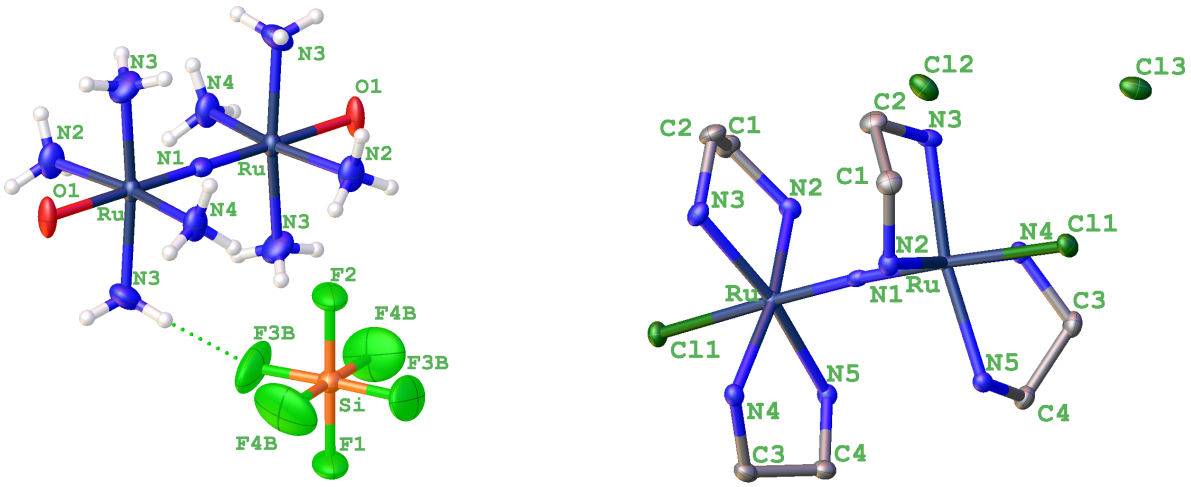

Figure 4.4: The X-ray crystallographic structures of (a) $[(H_2O)(NH_3)_4Ru(\mu\text{-}N)Ru(NH_3)_4(HO)](SiF_6)_2$ and (b) $[Cl(en)_2Ru(\mu\text{-}N)Ru(en)_2Cl]$ grown from diffusion of ethanol into water containing NH_4SiF_6 and deionized water solutions at room temperature, respectively. Thermal ellipsoids are at the 50% probability level.

Compound **4.1SiF6** crystallized into the monoclinic space group $I2/m$. The μ-nitrido nitrogen is located on $2/m$ special position. Thus the equatorial ammine ligands are eclipsed and the Ru-N-Ru bond angle is exactly 180° (Table 4.1). A mirror plane bisects the molecule along the Ru-N-Ru bond. Rotational disorder is observed in the ammines that sit on the mirror plane, as well as the fluorines of the SiF_6^{2-} counterions. Analysis of the bond angles of the equatorial positions shows that the ammines bend slightly away from the μ-nitrido, with the μ-N–Ru–NH_3 angle averaging 94.6°. The ruthenium–μ–nitrido distance is 1.737 Å, whereas the ruthenium-ammine distance is 2.102 Å. Inspection of the intermolecular interactions between neighboring cations show a close contact between axial oxygens of neighboring molecules of 2.538 Å by expansion of the hydrogen bonding network in the lattice. The two oxygens are related via a crystallographic inversion center; moreover, the distance is too short to constitute normal hydrogen bonding interactions. We hypothesize this is a symmetric hydrogen bond, where the atom is shared between the donating oxygen

atoms. The second hydrogen could not be found in the electron difference map. However based on the complex charge balance we assign the axial ligands as mixed hydroxide and water. This is similar to our previous work (see Chapter 3) on an analog of Ru360 which had a similar hydrogen bonding network and a mixed hydroxide/water axial ligand system.[223]

Table 4.1: X-ray crystallographic data collection and refinement parameters for $K_3[Ru_2NCl_8(H_2O)_2]$, $[(OH)(NH_3)_4Ru(\mu{-}N)Ru(NH_3)_4(OH_2)](SiF_6)_2$ and $[Cl(en)_2Ru(\mu{-}N)Ru(en)_2Cl]Cl_3$.

Crystal Data	$K_3[Ru_2NCl_8(H_2O)_2]$	$[(OH)(NH_3)_4Ru(\mu{-}N)Ru(NH_3)_4(OH_2)](SiF_6)_2$	$[Cl(en)_2Ru(\mu{-}N)Ru(en)_2Cl]Cl_3$
Formula Weight	653.08	668.6	649.82
Temperature/K	223	223	100
Crystal System	Monoclinic	Monoclinic	Hexagonal
Space Group	C $2/m$	I $2/m$	P6_522
a/Å	15.8583(16)	7.5926(7)	10.0036 (1)
b/Å	7.4075(5)	15.6754(14)	10.0036 (1)
c/Å	8.1957(6)	9.5465(12)	37.9277(3)
$\alpha/^\circ$	90	90	90
$\beta/^\circ$	121.115(2)	98.780(4)	90
$\gamma/^\circ$	90	90	120
Volume (Å^3)	824.24(12)	1122.9(2)	3287.00(8)
Z	2	2	6
D, g cm^{-1}	2.632	1.977	1.97
μ (mm^{-1})	3.868	1.563	16.94
Observed reflections	1185	6861	2088
Parameters	48	93	119
R1 (I $>2\sigma$))^a	0.0163(1129)	0.0229(1560)	0.0168(2069)
wR2 (I$>2\sigma$)^b	0.0349(1178)	0.0603(1709)	0.043(2088)
GOF^c	1.089	1.114	1.07
Wavelength	0.71073	0.71073	1.54184

^{a}R1 $= \Sigma||F_o|\text{-}|F_c||/\Sigma|F_o|$. ^{b}wR2 $= \{\Sigma[w(F_o^2 - F_c^2)^2]/\Sigma[w(F_o^2)^2]\}^{1/2}$.
^{c}GOF $= \{\Sigma[w(F_o^2 - F_c^2)^2]/(n-p)\}^{1/2}$.

Complex **4.2** crystallized as orange needles in the hexagonal space group P6_522 (Figure 4.4b). The ethylenediamine ligands show the canting typical for a 5-membered nonplanar chelate ring. This canting can be characterized by δ or λ configurations (Figure 4.5).[313,314]

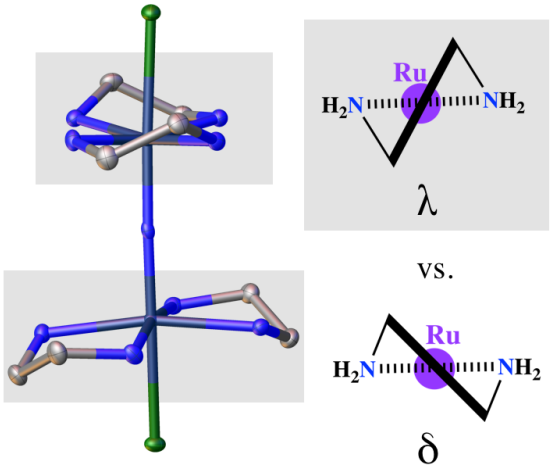

Figure 4.5: The ethylenediamine ligand orientation of compound **4.2**. δ or λ configuration possibilities are shown, with the assignment of λ in grey.

Complex **4.2** crystallized with both ruthenium centers in the λ configuration.

The ethylenediamine ligands are staggered in the equatorial positions and chlorides are on the axial positions (Figure 4.4b). The staggered conformation is different than the crystal structure of **4.1SiF6** and **4.SM2**; both of these compounds show an eclipsed conformation. The substitution of ethylenediamine ligands on $K_3[Ru_2NCl_8(H_2O)_2]$ has been previously reported.[294,295] The reported X-ray crystal structure has five en ligands, with one of the ligands bridging between the two ruthenium centers. In contrast to this reported structure, we observe a symmetric system around each ruthenium with *four* en ligands instead of *five* en ligands. The Ru-N-Ru bond angle is slightly bent, 176.36°, and is comparable to the reported en substituted complex with a Ru-N-Ru bond angle of 174.6° (Table B.4). A two-fold axis through the Ru-μ-N-Ru relates the ethylenediame ligands. Similar to compound **4.1SiF6**, the ligands are slightly pushed away from the bridging center, ~95° on average and the Ru-N μ-nitrido distance is 1.759 Å, whereas the Ru-N en-nitrogen distance is 2.105 Å. In the five-en reported complex, the Ru-N μ-nitrido distances was 1.742 Å and the Ru-N en-nitrogen equatorial distance was 2.113 Å.

Table 4.2: X-ray crystallographic data collection and refinement parameters for $[Ru_2N(bpy)_2Cl_5(DMF)]$ and $[Ru_2N(dmobpy)_2Cl_5(DMF)]$

Crystal Data	$[Ru_2N(bpy)_2Cl_5(DMF)]$	$[Ru_2N(dmobpy)_2Cl_5(DMF)]$
Formula Weight	778.86	898.97
Temperature/K	100.00(10)	100.01(10)
Crystal System	Triclinic	Triclinic
Space Group	$P\bar{1}$	$P\bar{1}$
a/Å	9.79250(10)	12.2823(3)
b/Å	11.28330(10)	12.5160(2)
c/Å	15.4471(2)	15.2094(2)
$\alpha/^\circ$	77.1190(10)	98.4980(10)
$\beta/^\circ$	84.0320(10)	106.815(2)
$\gamma/^\circ$	71.1160(10)	111.247(2)
Volume (Å^3)	1573.34(3)	2000.61(7)
Z	2	2
D, g cm^{-1}	1.644	1.492
μ (Mo Kα), mm^{-1}	1.411	
μ (Cu Kα), mm^{-1}		9.518
Observed reflections	5961	7570
Parameters	336	412
R1 (I $>2\sigma^a$	0.0170	0.0257
wR2 (I$>2\sigma$)^b	0.0407	0.0698
GOF^c	1.015	1.075
Wavelength	0.71073	1.54184

^{a}R1 $= \Sigma||F_o|-|F_c||/\Sigma|F_o|$. ^{b}wR2 $= \{\Sigma[w(F_o^2 - F_c^2)^2]/\Sigma[w(F_o^2)^2]\}^{1/2}$.
^{c}GOF $= \{\Sigma[w(F_o^2 - F_c^2)^2]/(n-p)\}^{1/2}$.

Single-crystals of **4.3** were grown from a DMF solution and analyzed analyzed by X-ray diffraction. The crystal structure of **4.3** conclusively reveals it to be $[Ru_2N(bpy)_2Cl_5(DMF)]$ (Figure 4.6a) with the linear Ru-N-Ru moiety intact. The complex is asymmetric; one ruthenium possesses an octahedral coordination geometry fulfilled by a bpy ligand, three chlorides, and the bridging nitrido, while the other octahedral ruthenium center is coordinated by a bpy ligand, two chlorides, a DMF solvent molecule, and the bridging nitrido. This geometry is quite different than two previously reported products.[294,297] The reaction product of $K_3[Ru_2NCl_8(H_2O)_2]$ with bpy is reported as the complex $[Ru_2N(bpy)_4(Cl)_2]^{3+}$.[294] However, this report is only characterized by infrared spectroscopy and elemental analysis.

A different reported structure with bpy substitution on the Ru-μ-N-Ru backbone has two bipyridine ligands occupying an equatorial binding site on each ruthenium, shown by X-ray crystallography. This was accessed by the high temperature reaction of $[Ru(bpy)(CO)_2Cl_2]$ in HCl-HNO_3 mixtures.[297]

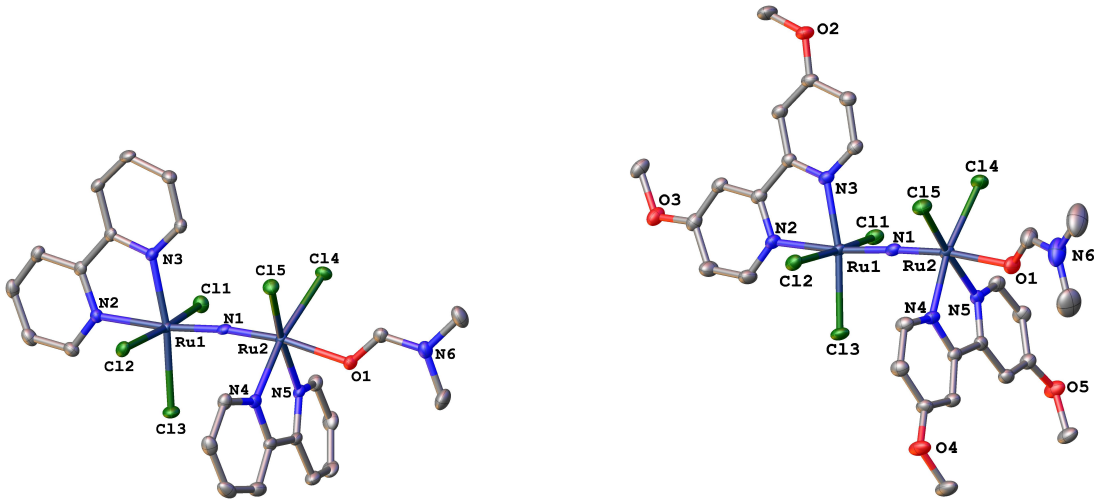

(a) (b)

Figure 4.6: The X-ray crystal structures of (a) $[Ru_2N(bpy)_2Cl_5(DMF)]$ and (b)$[Ru_2N(dmobpy)_2Cl_5(DMF)]$grown from diffusion of methanol into dimethylformamide at room temperature.

The crystal structure of **4.5** (Figure 4.6b) reveals the same stereochemistry that is present in complex **4.3**. Crystallographic refinement parameters and relevant interatomic distances and angles are collected in Tables 4.2 and B.5. The Ru-N nitrido distances are slightly asymmetric and vary from 1.7219(18) to 1.7375(18) Å. No significant deviations in these distances between the two compounds are noted, and the distances are similar to those found in previously reported dinuclear nitrido-bridged complexes.[295,297,298] The Ru-N-Ru angles, which deviate slightly from 180°, are 173.10(9)° and 177.27(11)° for **4.3** and **4.5**, respectively. The equatorial and axial Ru-ligand interatomic distances are disparate. For example, the Ru-N2 distance for the axial bpy ligand (2.1626(14) and 2.1546(19) Å for **4.3** and **4.5**, respectively) is approximately 0.1 Å longer than the corresponding equatorial

distances, which are between 2.0532(14) and 2.0646(18) Å. The elongation of the axial bond distances was most likely a consequence of the strong trans influence of the bridging nitrido ligand. Crystals of compound **4.4** were successfully grown, however could not be analyzed via X-ray diffraction due to twinning issues.

4.3.2 Spectroscopic characterization

UV-vis spectroscopy

The UV-vis spectrum of **4.1** in water shows 3 major transitions: 250 nm, 264 nm, 322 nm (Figure 4.7a). Compound **4.2** in water has a similar spectrum, with transitions at 239 nm, 274 nm, and 323 nm (Figure 4.7b, Table 4.3). The similarity in electronic spectra between these two complexes suggests that the transitions arise from the orbitals involved in the Ru-(μ-N)-Ru bridge. TDDFT analysis corroborates this hypothesis. The most intense transition for both **4.1** and **4.2** (264 nm or 274 nm, respectively) is from the axial ligands to the Ru-N-Ru backbone (Figures 4.7). For these two complexes, the axial ligands are chlorides – the energies of the LMCT[5] transition are quite similar.

[5]Ligand-to-metal charge transfer

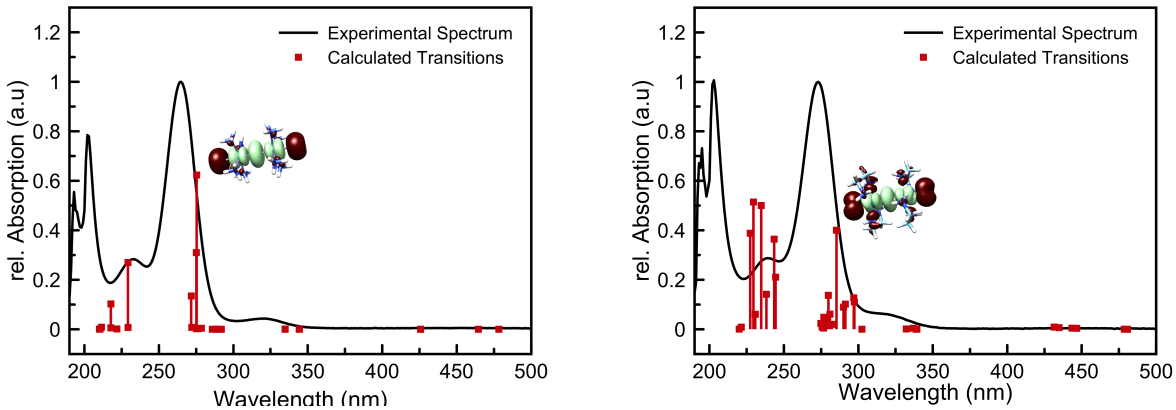

Figure 4.7: The experimental UV-vis absorption spectra in pH 7.4 PBS and calculated UV-vis spectra by TDDFT analysis. Calculated electronic transitions are illustrated by going from dark red to light green. (a) $[Cl(NH_3)_4Ru(\mu-N)Ru(NH_3)_4Cl]Cl_3$ and (b) $[Cl(en)_2Ru(\mu-N)Ru(en)_2Cl]Cl_3$

The UV-vis spectra of the compounds **4.3**, **4.4**, and **4.5** in dimethyl sulfoxide (DMSO) (Figure 4.8 and Table 4.3) exhibited low-energy transitions between 350 and 380 nm, and a higher energy transition near 300 nm. The low-energy transition is assigned as a metal-to-ligand charge transfer by analysis of the orbital contributions calculated by TDDFT. The energy of this transition shifts noticeably as the substituents on the bpy ligands are altered through **4.3**, **4.4**, and **4.5**.

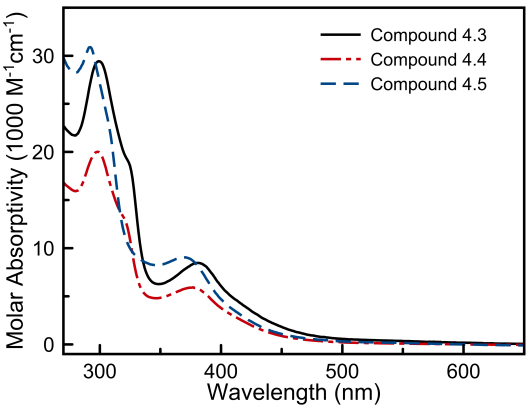

Figure 4.8: The experimental UV-vis absorption spectra in DMSO of $[Ru_2N(bpy)_2Cl_5(DMF)]$ (solid black line), $[Ru_2N(dmbpy)_2Cl_5(DMF)]$ (red dash-dot-dot line) and $[Ru_2N(dmobpy)_2Cl_5(DMF)]$ (blue dash line).

As more electron-donating groups are introduced, the MLCT[6] energy shifts to higher energy. This result is consistent with the effect of electron donating groups, which increase the energy of the accepting ligand π^* orbital of the diimine ligand.[315]

Table 4.3: Extinction coefficients for compounds **4.1** and **4.2** complexes taken in pH 7.4 PBS and compounds **4.3**, **4.4** and **4.5** in DMSO. Units in $[M^{-1}cm^{-1}]$ and wavelength maxima [nm] in parentheses

Compound **4.1**	Compound **4.2**	Compound **4.3**
9400 ± 820 (232)	9400 ± 240 (238)	29000 ± 200 (299)
32000 ± 3300 (265)	32000 ± 660 (274)	8200 ± 100 (381)
1400 ± 80 (322)	1700 ± 45 (322)	

Compound **4.4**	Compound **4.5**
20400 ± 800 (298)	35000 ± 4000 (392)
6000 ± 300 (376)	10200 ± 900 (368)

IR spectroscopy

A diagnostic feature in nitrido-bridged ruthenium complexes is the asymmetric Ru-N-Ru stretching mode. The infrared spectrum of **4.1SiF6** reveals the Ru-(μ-N)-Ru stretch to be at

[6]Metal-to-ligand charge transfer.

1061 cm^{-1}. This feature was assigned by exchanging the NH oscillators with ND oscillators. The exchange was accomplished by dissolving the compound in D_2O and lyophilization of the solvent. Comparison of the IR spectrum of compound **4.1** to **4.1SiF6** show consistent vibrations, with additional modes due to SiF_6^{2-} at 694 cm^{-1}. Of note, however, is a 17 cm^{-1} energy difference for the Ru-N-Ru stretching mode between **4.1** and **4.1SiF6**. We attribute this shift due to **4.1** and **4.1SiF6** containing axial chlorides and waters, respectively. DFT calculations of the vibrational frequencies of the two compounds revealed the same difference; the presence of axial waters increasing the Ru-N-Ru vibrational energy. We also see differences in the ammine stretches between **4.1** and **4.1SiF6** which we also attribute to the small change in the hydrogen bonding network caused by the replacement of chloride to water in the axial position. The axial water can hydrogen bond with the equatorial ammines, slightly reducing the observed vibrational energy. This same shift is observed in the vibrational frequency DFT calculations. Morover, reports of **4.SM2** indicate counterion dependent small shifts in the IR spectrum. This suggests that upon counterion substitution from chloride to hexafluorsilicate for compound **4.1** we would expect some changes.[316]

Compound **4.2** has a more complex IR spectrum in fingerprint region due to the additional modes from the C-H bonds (Figure 4.9b). The sharp feature at 1055 cm^{-1} is likely the Ru-N-Ru stretch, consistent with the previously reported datum for this complex.[294]

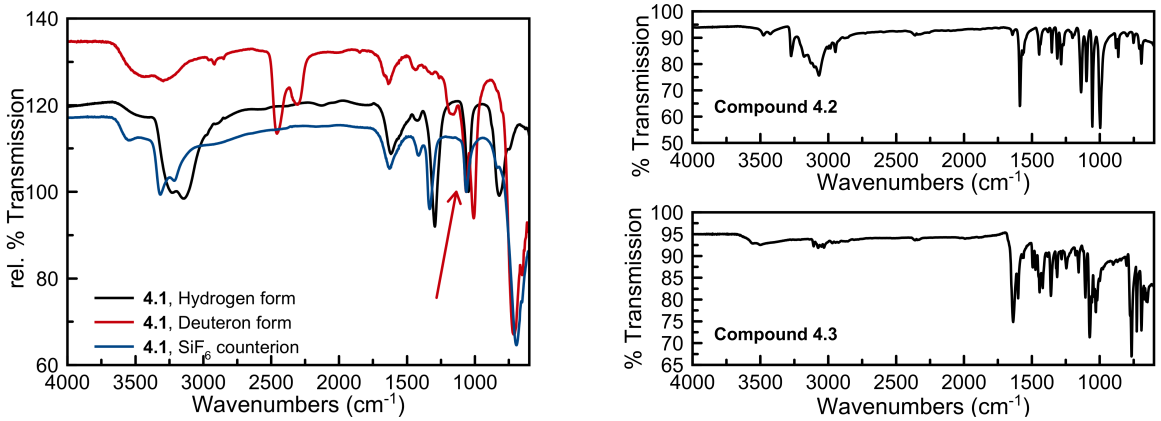

(a) (b)

Figure 4.9: The infrared spectra of (a) hydrogen, deuteron, and SiF_6 form of compound **4.1** and (b)$[Cl(en)_2Ru(\mu-N)Ru(en)_2Cl]Cl_3$ (**4.2**) and $[Ru_2N(bpy)_2Cl_5(H_2O)]$ (**4.3**). The arrow points at the Ru-N-Ru asymmetric stretch.

Similar to compound **4.2**, the conclusive identification of the asymmetric stretching mode in the IR spectrum of **4.3**, **4.4**, and **4.5**, however, was challenged by the presence of ligand vibrational features within this region (Figure 4.9b). Absorbance bands at 1030 and 1074 cm^{-1}, 1032 and 1065 cm^{-1}, and 1030 and 1063 cm^{-1}, are tentatively assigned as the symmetric and asymmetric Ru-N-Ru stretching frequencies in **4.3**, **4.4**, and **4.5**, respectively. These values are consistent with previously reported all-equatorial bpy complex, $[Ru_2N(bpy)_2Cl_5(H_2O)]$, suggesting that the stereochemical arrangement of these ligands has little effect on the ruthenium-nitrido bond.[294]

NMR spectroscopy

Compound **4.SM2** was reported to be diamagnetic with a magnetic susceptibility of -6.3×10^{-6} c.g.s.u.[292] The NMR spectra revealed that compounds **4.1**, **4.2**, **4.3**, **4.4**, and **4.5** were all diamagnetic as expected for Ru^{IV}/Ru^{IV} systems. The ^1H NMR spectrum of **4.1** in DMSO-d_6 had a single peak at 4.14 ppm corresponding to the ammine N-H protons.

The presence of a single peak is indicative of a symmetric complex; no additional signals are observed. Compound **4.2** had a ^{1}H NMR spectrum that showed two multiplets at 2.69 ppm and 3.10 ppm, relative to 1,4-dioxane in D_2O, corresponding to the C-H protons. The ammine protons are at 5.16 ppm and 5.32 ppm and decay in intensity over time ($t_{1/2}$ = 72.6 min) as the N-H protons exchange with deuterium. The two C-H protons on each carbon of the ethylenediamine were not symmetric due to the cant and restricted movement of the 5-membered chelate ring (Figure 4.5). The canting results in the CH_2 protons appearing as a doublet. Similarly, the ammine N-H protons were also a doublet. The ^{13}C NMR spectrum had one signal at 46.44 ppm, indicative of a symmetric spin system (Figure B.2). This is in contrast to the reported μ-nitrido complex with five en ligands; the authors reported an asymmetric spin system with five ^{13}C signals.[295]

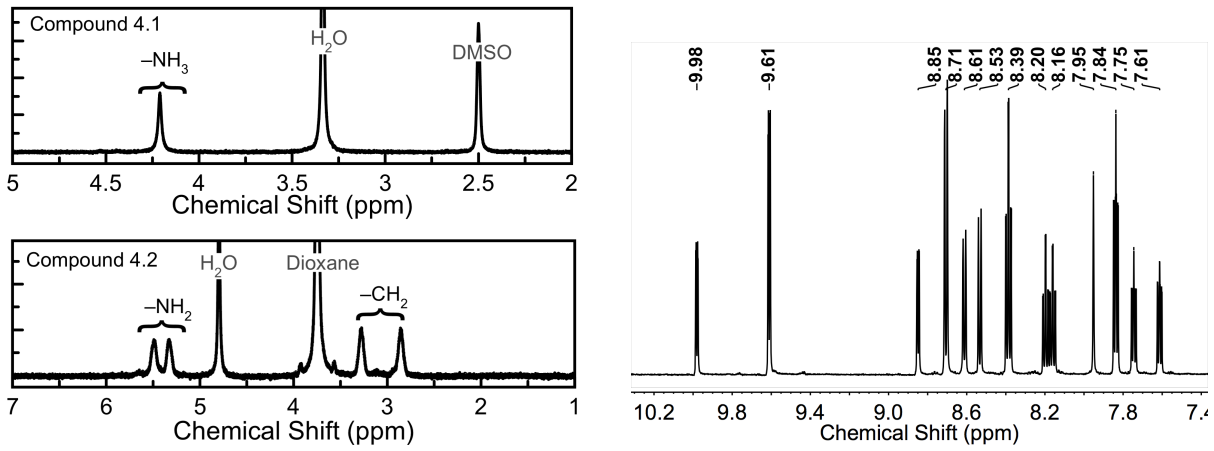

(a) (b)

Figure 4.10: The NMR spectra of (a) compounds **4.1** and **4.2** in DMSO-d_6 and D_2O, respectively and (b) compound **4.3** in DMSO-d_6.

^{1}H NMR spectroscopy of compounds **4.3**, **4.4** and **4.5** revealed three distinct aromatic spin systems similar to **4.3** (Figures 4.10b and B.4-B.9). Previously reported nitrido-bridged dinuclear ruthenium complexes bearing bpy ligands, $[Ru_2N(bpy)_2Cl_5(H_2O)]$ and $(H_5O_2)[Ru_2N(bpy)_2Cl_6]$ were isolated from the high temperature reaction of $[Ru(bpy)(CO)_2Cl_2]$ in HCl–HNO_3 mixtures and were structurally characterized by X-ray

crystallography.[297] These structures both showed a single bpy ligand coordinated in a bidentate manner to each ruthenium center. The orientation of the bpy ligands were such that both nitrogen donor atoms reside in a cis disposition on the equatorial plane, in the cis disposition relative to the bridging nitrido ligand. Although the ^{1}H NMR spectra of these complexes was not reported, symmetric spectra would be expected given the chemical equivalence of the two bpy ligands. By contrast, the ^{1}H NMR spectrum of compounds **4.3**, **4.4** and **4.5** reveal three distinct sets of aromatic spin systems in a ratio of 2:1:1 (Figure 4.10b), indicating that we had isolated a less symmetric compounds than the previously reported $[Ru_2N(bpy)_2Cl_5(H_2O)]$, $(H_5O_2)[Ru_2N(bpy)_2Cl_6]$, and $[Ru_2N(bpy)_4(Cl)_2]^{3+}$ complexes. Lastly, free DMF signals were present in the ^{1}H NMR at 7.95, 2.89, and 2.73 ppm, corresponding to uncomplexed solvent, suggesting the axial position is relatively labile to substitution.

Cyclic voltammetry

The electrochemical properties of **4.3**, **4.4**, and **4.5** were investigated by cyclic voltammetry (Figure 4.11). Anodic scans revealed the presence of a quasi-reversible oxidation feature, which is tentatively attributed to the $Ru^{V}Ru^{IV}/Ru^{IV}Ru^{IV}$ couple. In related nitrido-bridged dinuclear complexes, the $Ru^{V}Ru^{IV}$ state could be accessed at relatively mild potentials, signifying the ability of the nitrido ligand to stabilize high oxidation states.[302–304] This quasi-reversible oxidation ($E_{1/2}$) to the $Ru^{V}Ru^{IV}$ state occurs at 1.33, 1.25, and 1.19 V vs SCE for **4.3**, **4.4** and **4.5**, respectively, demonstrating that the donating methyl and methoxy groups on **4.4** and **4.5** stabilize the higher oxidation states.

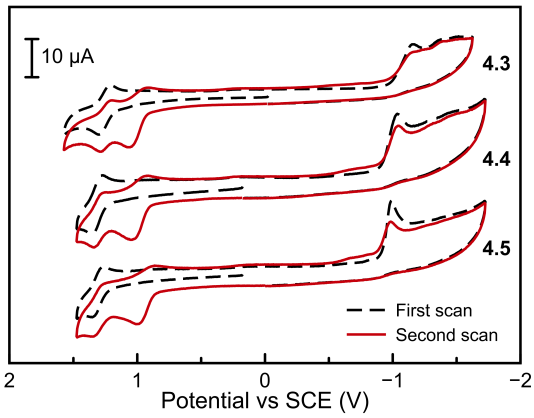

Figure 4.11: The cyclic voltammetry profiles of compounds **4.3**, **4.4**, and **4.5**.

Upon scanning cathodically, an irreversible reduction feature is observed, which is tentatively assigned to the $Ru^{IV}Ru^{IV}/Ru^{IV}Ru^{III}$ couple. The peak potentials (E_p) of this irreversible reduction are –1.03, –1.10, and –1.22 V vs SCE for **4.3**, **4.4**, and**4.5**, respectively. As expected, these values indicate that reduction occurs at more positive potentials when the bpy ligand has less electron-donating substituents. Upon cycling back to anodic potentials, a new quasi-reversible oxidation feature, presumably arising from the irreversible reduction product, is observed. Notably, the $E_{1/2}$ of this quasi-reversible oxidation is relatively invariant for the three complexes: 0.95 V vs SCE. This result suggests that this oxidation might arise from a ruthenium-containing product that lacks the diimine ligands.

4.3.3 Solution reactivity

Ru360 was found to undergo aquation at the axial positions with the formate groups replaced by aquo ligands.[233] The corresponding Cl/Cl complex, with chlorides instead of formates, was also observed to undergo aquation. This reaction is most likely a two-step process, where one axial ligand is substituted by water and then the second one. However, only one rate constant was observed and thus the data was treated as a single-step process

that was first-order with respect to ruthenium. The aquation was observed to be pH dependent, with a maximum rate constant of $\sim 8\times10^{-3}$ sec^{-1} ($t_{1/2}$ = 1.4 min) at pH 1 slowing to $\sim 2\times10^{-4}$ sec^{-1} ($t_{1/2}$ = 58 min) at pH 7 for the aquation of both the formate species and the chloride species.

Compounds **4.3**, **4.4**, and**4.5** did not have an observed solution state structure, other than the labile DMF axial ligand observed by ^{1}H NMR spectroscopy. Compound **4.1** exhibited a time-dependent change in the UV-vis spectrum. In pure water, the main spectral feature at 265 nm underwent a blue shift to 256 nm (Figure 4.12a). Plots of $\ln[(A_0 - A)/(A_t - A)]$ vs time were linear, indicating a first order kinetic process, where A_0 is the initial absorbance, A_t is the absorbance at time t and A is the equilibrium absorbance.[317] The observed first order rate constant (k_{obs}) in pure water was $1.9\times10^{-4} \pm 8.8\times10^{-6}sec^{-1}$ ($t_{1/2}$ = 60 min), fit to the equation$[(A_0 - A)/(A_t - A)] = \exp(-k_{obs}t)$. There were three well-resolved isosbestic points in pure water at 315 nm, 292 nm and 234 nm, indicating that this reaction proceeds without any long-lived intermediates. The rate constant was similar to those measured for the aquation of other ruthenium complexes.[233,317,318]

Tracking the pH reveals a decrease in the pH from ∼8 to ∼4. This suggests the aquation process includes the loss of an equivalent of HCl and therefore most likely pH dependent. Additionally, the aquation was found to be highly dependent on the buffer utilized. At pH 7.4, three different UV-vis spectral features were observed with three different buffers (Figure 4.12b) In 0.1 M MOPS[7], almost no spectral changes were observed, while in 0.1 M Bis-Tris the process appeared to reach equilibrium (Figure 4.12b, left). In 0.1 M potassium phosphate buffer, the aquation appeared to proceed but a new product grew in, potentially a phosphate-bound complex. At very low pH (1-3.5) in $HClO_4$ acid a biexponential spectral change[8] is observed (Figure 4.12b, right). The two observed rate constants are most likely from each

[7] 3-(*N*-morpholino)propanesulfonic acid

[8] abs = $c_1(e^{-k_1t}) + c_2(e^{-k_2t}) + c_3$ where c_n are coefficients and k_1 and k_2 are first order rate constants

of the two aquation steps. The first rate constant (k_1) is is $9.1\times10^{-4} \pm 4.1\times10^{-4}$ sec^{-1} ($t_{1/2}$ = 12 min) and the second (k_2) is $6.3\times10^{-5} \pm 9.8\times10^{-6}$ sec^{-1} ($t_{1/2}$ = 183 min) between pH 1 and 3.5 in $HClO_4$. This reaction is significantly slower than the aquation observed for Ru360. Above pH 5 the UV-vis kinetic traces were consistently more complex, without clean isosbestic points or spectral shifts. The complexity suggests that as the hydroxide concentration increases additional mechanisms are accessed leading to more complex spectra.

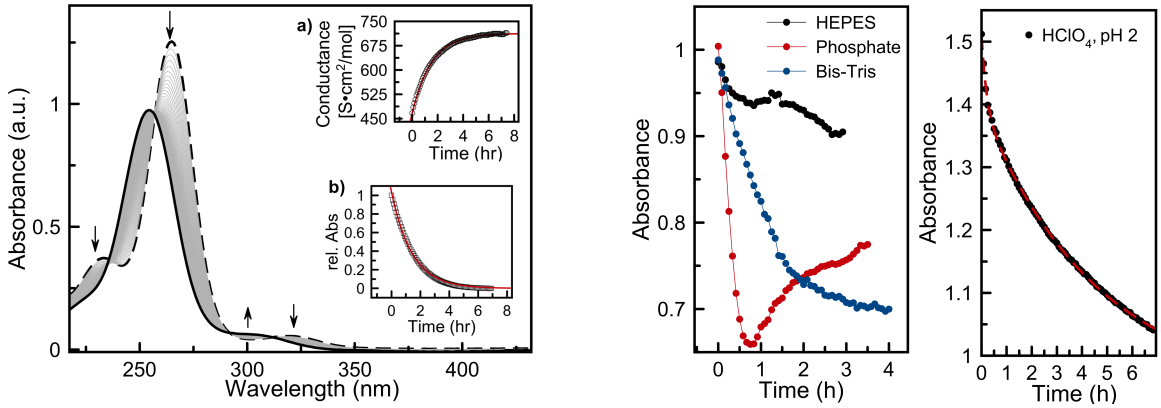

(a) (b)

Figure 4.12: (a) The solution state change of compound **4.1** in pure H_2O by conductance (subfigure a) and UV-Vis (main and subfigure b). (b) Buffer dependence at pH 7.4 for the aquation process and a representative trace for the aquation in $HClO_4$ (pH 2) for compound **4.1**.

As the chloro ligands are substituted for aquo, it is expected the electrical conductivity will increase as the charge of the complex will increase from +3 to +5. Indeed, this was observed in a time dependent manner (Figure 4.12a) with a first order rate constant of $1.8\times10^{-4} \pm 8.1\times10^{-6}$ sec^{-1} ($t_{1/2}$ = 64 min). This was almost identical to the rate constant in H_2O observed by UV-vis. Due to the instability of the complex to aquation, analysis of the initial compound using the Debye-Hückel-Onsager equation could not be obtained on the initial solutions. This equation describes the relationship between concentration (c) and conductivity in very dilution solutions: $\Lambda = \Lambda_0 - K\sqrt{c}$, where Λ is the measured molar conductivity, Λ_0 is the infinite dilution conductivity, and K is a constant that is

proportional to Λ_0, the ionic charge and the ionic strength.[319,320] For the stable equilibrium product of compound **3.1** an infinite dilution conductance of 997 S·cm^2/mol was measured. As the electrolyte number increases, the conductance will also increase, ranging from 150-250 S·cm^2/mol, depending on the electrolyte.[320] $K_4[Fe(CN)_6]$, a 4:1 electrolyte, had an infinite dilution conductance of 740 S·cm^2/mol. A 5:1 electrolyte would be expected to have a higher Λ_0. This will put the range for 5:1 electrolytes around 900-1000 S·cm^2/mol. Aquation of compound **4.1** would result in increased charge from +3 to +5, which was consistent with the observed data.

Moreover, the fully aquated product would have a symmetric ^{1}H NMR signature. The equilibrium product from the aquation of compound **4.1** was isolated by the lypohilization of an aged, aqueous solution. The ^{1}H NMR spectra of the equilibrium product indicated the formation of a new species. This new compound contains only one NMR signature, a singlet at 4.24 ppm, consistent with a new symmetric product. In the case of single aquation, with one aquo axial ligand and one chloro, an asymmetric signature would be expected. Both the new NMR signature, and the increased conductivity, are observed in the equilibrium product of **4.1**. Thus we conclude compound **4.1** underwent complete aquation.

Compound **4.2** was isolated with chlorides in the axial positions confirmed by X-ray crystallography (Figure 4.4b). Similar to compound **4.1**, the change can be observed by NMR, UV-vis and conductivity. Integration of the ^{1}H NMR peaks indicated only about 20% conversion (Figure 4.13a). The C-H protons from the en ligand occurred at 2.69 and 3.10 ppm. However, in an aged solution two additional peaks appeared at 2.76 and 2.96 ppm with the same symmetric spin system as the original two C-H signals. To verify these smaller signatures as the diaquated product, a little AgOTf was added to the NMR tube. The silver will react with the Cl^- to form insoluble AgCl. Water will quickly add in the axial positions, thereby forming the diaqua complex. After the addition of AgOTf the peaks at

2.96 and 2.76 ppm quickly grew in intensity while the peaks at 2.69 and 3.10 ppm decreased in intensity. This revealed that the observed signals were in fact from the Cl/Cl complex and the H_2O/H_2O complex. The asymmetric Cl/H_2O system was not observed in the ^1H NMR.

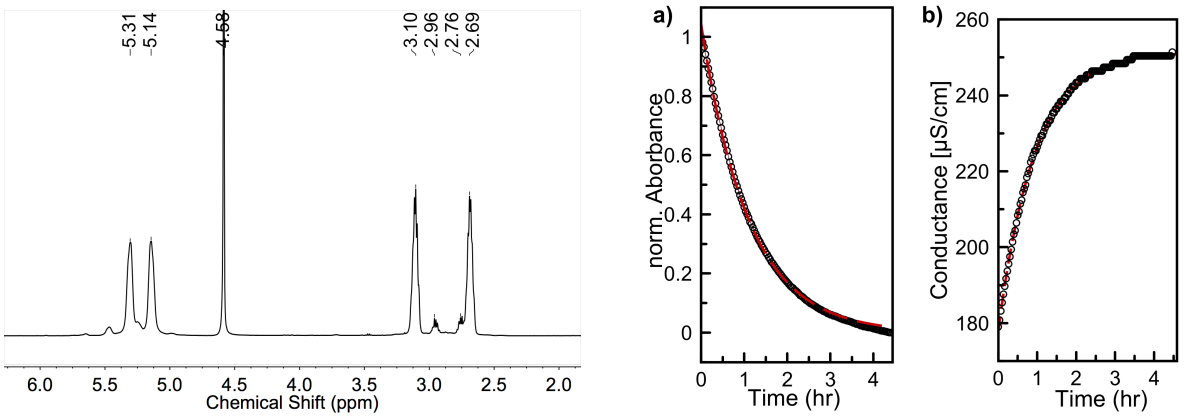

(a) (b)

Figure 4.13: (a) Equilibrium ^1H NMR spectrum of compound **4.2** (b) The solution state change of compound **4.2** in pure H_2O by UV-Vis (subfigure a) and conductance (subfigure b).

The time-dependent conductance of compounds **4.2** reveals an observed rate constant of 2.5×10^{-4} sec^{-1} ($t_{1/2}$ = 46 min) (Figure 4.13b). The UV-vis undergoes a blue shift from 274 nm to 267 nm. Tracking the decrease in the absorption at 274 nm over time reveals a rate constant of 3.0 $\times10^{-4}$ sec^{-1} ($t_{1/2}$ = 39 min), similar to the rate constant observed by conductance. A fresh aqueous solution has a molar conductance of 368.1±13.48 $S{\cdot}cm^2/mol$, consistent with the +3 charge expected from the crystal structure.[321] From these data, we conclude that compound **4.2** undergoes incomplete aquation, reaching equilibrium at ∼20% formation of the H_2O/H_2O product.

4.4 Conclusion

In summary, the synthesis and characterization of five diruthenium μ-nitrido complexes are described. These complexes are prepared starting from $K_3[Ru_2NCl_8(H_2O)_2]$. X-ray crystal structures revealed ligand substitution on the equatorial positions for compound **4.1** and **4.2**, however an asymmetric bonding for compounds **4.3** and **4.5**. Compounds **4.1** and **4.2** have UV-vis spectrum dominated by LMCT transitions, while compounds **4.3**, **4.4**, and **4.5** are dominated by MLCT transitions. Infrared spectroscopy revealed consistent Ru-N-Ru stretching modes which are diagnostic for this class of compounds. NMR spectroscopy was consistent with the symmetric and asymmetric environment for each respective complex. In aqueous solutions compound **4.1** and **4.2** underwent aquation in the axial positions, observed by changes in the UV-vis spectrum, conductance and ^{1}H NMR. Future directions for these systems include exploring detailed kinetics for compounds **4.1** and **4.2**. In addition, exploring axial ligand substitutions as well as different equatorial ligands can be used to build a library of similar complexes.

CHAPTER 5

BIOLOGICAL INVESTIGATIONS

5.1 Introduction[1]

In additional to their application as catalysts, ruthenium complexes may also exhibit interesting biological activity. NAMI-A and KP1019 (Figure 5.1a, 5.1b) are examples of ruthenium based anti-cancer agents and have been advanced into the clinical trial stages.[322–328] RAPTA-C, a complex of the organometallic "piano-stool"-type family (Figure 5.1c), and similar structural analogs have also been extensively explored for their anticancer properties.[329–333]

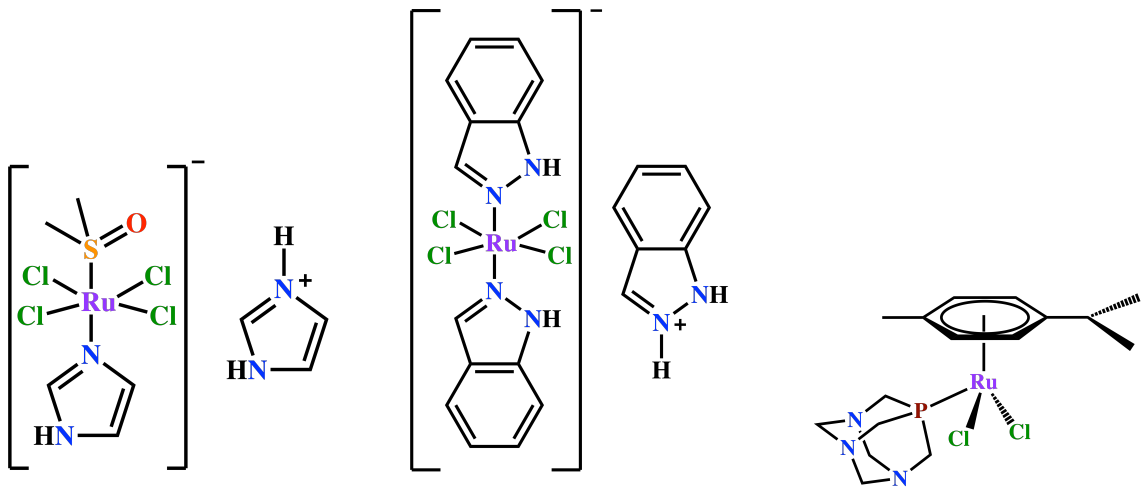

(a) (b) (c)

Figure 5.1: The structure of three of the most common ruthenium anti-cancer complexes under investigation: (a) NAMI-A, (b) KP1019 and (c) RAPTA-C

RuRed, discussed earlier in chapter 2, has been used as a cellular stain due to its high charge and intense color. It also inhibits mitochondrial calcium uptake along

[1]Chapter reproduced in part with permission from *Inorg. Chem.*, **2017**, 56(6), pp 3123 - 3126. Copyright 2017, American Chemical Society.

with Ru360 (see Chapter 2). Due to their low toxicities and potent MCU inhibitory properties, these compounds have been investigated as potential therapeutics for lowering the effects of ischemia-reperfusion injury.[192,193,249–252,255,259–261,334] We were interested in expanding the library of MCU inhibitory complexes with similar structural frameworks as Ru360 to explore potential structure-activity relationships, and thereby understand the mechanism of action. In this vein, we synthesized and characterized several structural analogs of Ru360 (see Chapters 3 and 4): $[(OH_2)(NH_3)_4Ru(\mu\text{-}O)Ru(NH_3)_4(OH_2)]^{5+}$ (**3.1**), $[Cl(NH_3)_4Ru(\mu\text{-}N)Ru(NH_3)_4Cl]^{3+}$ (**4.1**). $[Cl(en)_2Ru(\mu\text{-}N)Ru(en)_2Cl]$ (**4.2**), $[(DMF)Cl_2(bpy)Ru(\mu\text{-}N)Ru(bpy)Cl_3]$ (**4.3**), $[(DMF)Cl_2(dmbpy)Ru(\mu\text{-}N)Ru(dmbpy)Cl_3]$ (**4.4**) and $[(DMF)Cl_2(dmobpy)Ru(\mu\text{-}N)Ru(dmobpy)Cl_3]$ (**4.5**).

These structural analogs of Ru360 were tested for cell viability in HeLa cell. MCU inhibition abilities were determined in permeabilized HeLa cells. Compounds found to inhibit mitochondrial calcium uptake were further studied using isolated mitochondria expressing the MCU in a variable dose manner to determine the 50% inhibitory concentration of calcium uptake. From these data three compounds were found to inhibit the MCU: $[(OH_2)(NH_3)_4Ru(\mu\text{-}O)Ru(NH_3)_4(OH_2)]^{5+}$, $[Cl(NH_3)_4Ru(\mu\text{-}N)Ru(NH_3)_4Cl]^{3+}$ and $[Cl(en)_2Ru(\mu\text{-}N)Ru(en)_2Cl]^{3+}$. These three compounds were tested on both HeLa and HEK293 cells for uptake and cytotoxicity. The most potent compound was found to be **4.1**, and additional mechanistic studies with the D261A and S238A MCU mutants were investigated.

5.2 Cellular toxicity

The MTT assay can be used to measure cell viability.[335,336] The reduction of the yellow 3-(4,5-dimethylthiazol-2-yl)-2,5-diphenyltetrazolium bromide (MTT) to the formazan salt,

3-(4,5-dimethylthiazol-2-yl)-2,5-diphenylformazan, (Figure 5.2) by mitochondrial reductase produces purple crystals. The crystals only form in respiring (viable) cells and are soluble in polar organic solvents, such as DMSO. Dose-dependent % viability is determined by measuring the absorbance of the resulting formazan dye.

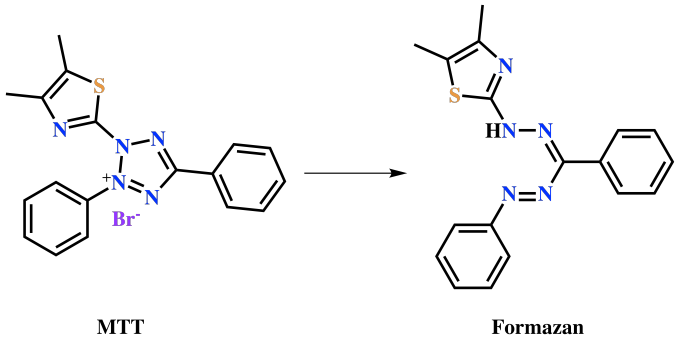

Figure 5.2: Reduction of 3-(4,5-dimethylthiazol-2-yl)-2,5-diphenyltetrazolium bromide (MTT) to 3-(4,5-dimethylthiazol-2-yl)-2,5-diphenylformazan (Formazan) catalyzed by mitochondrial reductase.

Compounds **3.1**, **4.1** and **4.2**, were nontoxic in HeLa cells, with 50% viability inhibitory concentrations (IC_{50}) of 228 $\pm$15 μM and 225$\pm$33 μM, for **4.1** and **4.2**,respectively (Figure 5.3a). The three μ-nitrido complexes with bipyridine (**4.3**, **4.4**, and **4.5**) substitutions were also nontoxic up to 20 μM (Figure 5.3b). However, due to solubility limitations of these complexes, IC_{50} values could not be obtained. Compound **3.1** did not show consistent cytotoxicity at high concentrations over four trials – in one trial at 400 μM there was not 100% cell death and one data set showed a full cell curve with an IC_{50} value of 290 μM. At 100 μM, the average cell viability was 67$\pm$13 % over four trials; this is most likely due to the observed instability in biological media, as discussed in Chapter 3.

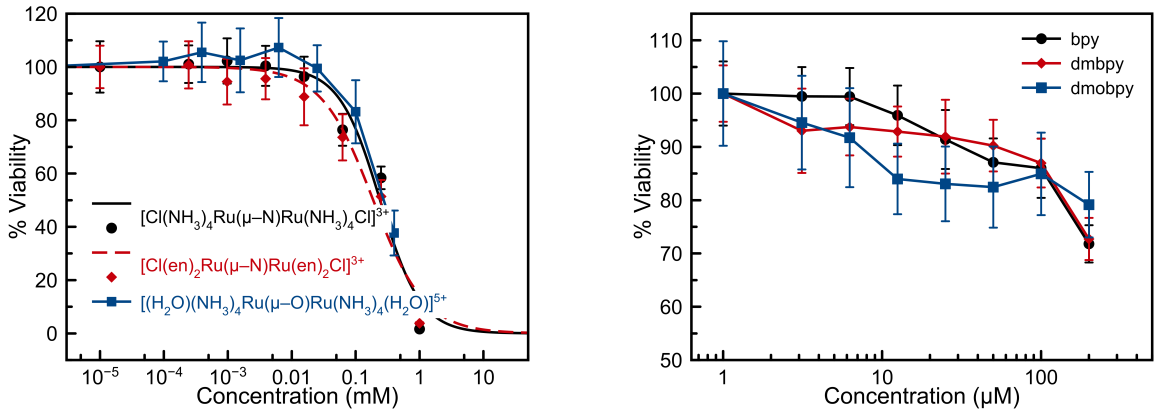

(a) (b)

Figure 5.3: The cellular viabilities of the (a) oxo-bridged Ru360 analog, and the ammine and ethylenediamine substituted nitrido complexes. (b) The cell viabilities of the three bipyridine substituted nitrido bridged complexes in HeLa cells.

The cell viability was also considered in healthy kidney cells (HEK293). These were used as a more accurate model for ischemia reperfusion injury in comparison to the HeLa cells as kidneys are known to undergo IRI. HEK293 cells were found to have diminished adherence to cell culture dishes when treated with ruthenium-containing complexes, in comparison to untreated cells. Thus, single-dose cytotoxicity measurements were performed with a slightly modified protocol. HEK293 cells were dosed with the three lead compounds, **3.1**, **4.1** and **4.2**, for 72 hr. The % viabilities were found to be 83%, 68% and 80% for compounds **3.1**, **4.1** and **4.2**, respectively. These complexes were all more cytotoxic in comparison with HeLa cells, however could still be considered generally nontoxic.

5.3 Cellular uptake

Metallic complexes may enter cells via several different mechanisms. Passive diffusion, or simple diffusion through the cellular membrane, is perhaps the simplest pathway, and some metallic complexes are known to enter in this manner.[337] However, this is less likely

for charged complexes, such as NAMI-A or KP1019 (Figure 5.1) as their positive charges impede progress through the anionic phospholipid membrane. These types of complexes are more likely to enter via active transport, the second major mechanism for cellular uptake. NAMI-A, for example, is not taken up by the cell efficiently and instead acts on the cellular wall.[338–340] Binding of serum proteins and ubiquitin by metal complexes may prove to be an additional mechanism for cellular entry of ruthenium complexes.[339,341–343] Transferrin is a serum protein that acts as an iron binder and transporter. After binding the transferrin receptor, the protein enters the cell via endocytosis and the iron is reduced and released into the cytosol.[344,345] Although ruthenium complexes have been shown to bind transferrin, whether or not this mediates ruthenium cellular uptake is a subject of continuing research.[289,324,326,338,339,346–355]. Regardless of the mechanism, passive or active, the levels of compound that enter the cell are critical in determining the efficacy of the compound of interest.

KP1019 accumulates in SW480 (colon adenocarcinoma) cells at a concentration of 171 $\pm$ 7 pg/μg; Ru content in a variety of cell lines from short term dosage by KP1019 is around 500 pmol/10^6 cells.[356,357] In A2780 cells dosed with KP1019, ruthenium levels in isolated mitochondrial was 650 pg/μg, whereas in the related cisplatin resistant line, A2780cisR, the Ru content was a factor of 3.7 lower. However, for NAMI-A, this value was close to 350 pg/μg, and there was not a significant difference between cell lines. This result suggests that even for similar compounds the subcellular distribution is highly variable. Ruthenium is not endogenous to biological systems. Therefore detection of complexes is amenable to analytical techniques such as atomic absorption spectroscopy, X-ray absorption or fluorescence techniques, electron paramagnetic resonance spectroscopy and inductively coupled plasma ionization techniques.[346,356–363] Atomic absorption (AA) is one of the more common methods due to its high sensitivity and ease of use.[356,360]

Table 5.1: Ru levels of lead compounds treated with 25 μM in HeLa and HEK293 cells.

Compound	Cell Type	Concentration [pg Ru/μg protein]
Ru360	HeLa	75 ± 16
$[(OH_2)(NH_3)_4Ru(\mu-O)Ru(NH_3)_4(OH_2)]^{5+}$	HeLa	45 ± 3
$[Cl(NH_3)_4Ru(\mu-N)Ru(NH_3)_4Cl]^{3+}$	HeLa	210 ± 83
$[Cl(en)Ru(\mu-N)Ru(en)Cl]^{3+}$	HeLa	96± 15
Ru360	HEK293	202 ± 23
$[(OH_2)(NH_3)_4Ru(\mu-O)Ru(NH_3)_4(OH_2)]^{5+}$	HEK293	123 ± 34
$[Cl(NH_3)_4Ru(\mu-N)Ru(NH_3)_4Cl]^{3+}$	HEK293	327 ± 98
$[Cl(en)Ru(\mu-N)Ru(en)Cl]^{3+}$	HEK293	76 ± 43

To measure the cellular uptake of compounds **3.1**, **4.1** and **4.2**, the cells were cultured for 24 h. The cells were then treated with 25 μM of each compound and incubated for an additional 24 h. The cells were harvested, lysed, the protein content measured by the Bradford assay, and the ruthenium content by AA. Treatment with 25 μM of compound **3.1** in HeLa cells showed complex uptake of 45 pg/μg Ru content per protein (Table 5.1). Dosing HeLa cells with **4.1** and **4.2** showed Ru content per protein content of 210 and 96 pg/μg, respectively. In HEK293 cells, these levels were 123, 327 and 76 pg Ru/ μg protein for **3.1**, **4.1** and **4.2**, respectively. Dosing with Ru360 had a Ru uptake concentration of 75 pg Ru/ μg protein in HeLa cells and 202 pg Ru/ μg protein in HEK293 cells (Table 5.1). A plausible explanation in the difference between these compounds is the difference in charge. The +5 charge of complex **3.1** maybe facilitate interactions with the anionic phospholipid membranes. In comparison, the +3 charge of complex **4.1** will have less electrostatic interactions with the membranes. However additional mechanisms may be operating since the nitrido bridged complexes aquate at the axial positions, which will increase the complex charge (+3 to +5, see Chapter 4). The low uptake of the ethylenediamine substituted system (compound **4.2**) was unexpected. Though of the same ionic charge as compound **4.1**, the slightly more lipophilic ligands appear to impact uptake significantly.

5.4 Calcium uptake inhibition

For all the structural analogues to Ru360 and related starting materials, we verified the mitochondrial calcium uptake inhibition properties. HeLa cells (7.5×10^6) were permeabilized with digitonin and incubated with 2 μM of the turn-on calcium-responsive dye Calcium Green-5N.[118,364] The fluorescence response of the dye was monitored over time after the addition of 7.5-10 μM boluses of $CaCl_2$. Addition of Ca^{2+} ions leads to an immediate increase in emission intensity, which decays over the course of 3-5 minutes as the Ca^{2+} ions are buffered by the mitochondria (Figure 5.4a, blank). This process is reproducible for many ($\sim$10) pulses of Ca^{2+} ions, after which an overload of Ca^{2+} in mitochondria triggers the opening of the permeability transition pore and leads to release of Ca^{2+} ions from the organelle.

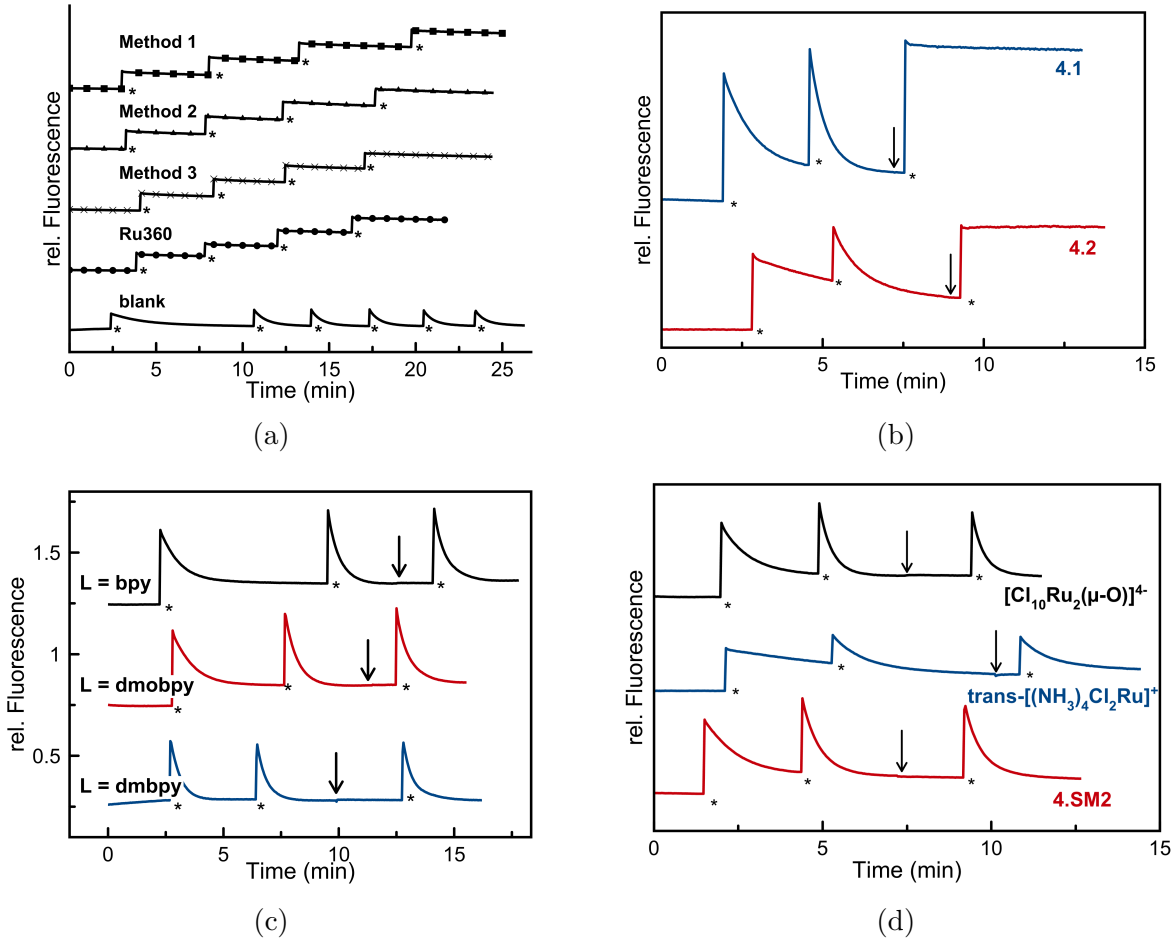

Figure 5.4: Calcium uptake inhibition using the Calcium Green-5N assay using permeabilized HeLa cells. The arrows indicate when the ruthenium complex is added in (b), (c) and (d). (a) The response from the three methods to synthesize $[(OH_2)(NH_3)_4Ru(\mu\text{-}O)Ru(NH_3)_4(OH_2)]^{5+}$ (**3.1**), commercial Ru360 and no inhibitors present (blank). The inhibitors were preincubated in the cuvette for 15 min before beginning the run. (b) $[Cl(NH_3)_4Ru(\mu\text{-}N)Ru(NH_3)_4Cl]^{3+}$ (**4.1**) and $[Cl(en)Ru(\mu\text{-}N)Ru(en)Cl]^{3+}$ (**4.2**) calcium uptake inhibition; (c) Bipyridine substituted nitrido bridged complexes (**4.3**, **4.4** and **4.5**), with the ligand specified; (d) the lack of calcium uptake inhibition of two starting materials and a potential metabolite. The asterisk indicates the addition of a calcium ion bolus. Figure reproduced in part with permission from *Inorg. Chem.*, **2017**, 56(6), pp 3123 - 3126. Copyright 2017, American Chemical Society.

The addition of 5 μM of **3.1**, synthesized by the different methods outlined in Chapter 3, to permeabilized HeLa cells inhibits mitochondrial calcium uptake (Figure 5.4a). A bolus of Ca^{2+} gives rise to an increase in fluorescence intensity with no decay, as the mitochondrial

calcium uptake is impaired. Commercially available Ru360 exhibits similar properties in preventing mitochondrial calcium uptake (Figure 5.4a). Similar responses were seen with **4.1** and **4.2** (Figure 5.4b). However, the bipyridine substituted complexes, $[Cl_{10}Ru_2(\mu-O)]$ and **4.SM2** did not show any inhibitory properties (Figures 5.4c, 5.4d). trans-$[(NH_3)_4Cl_2Ru]^+$ (synthesized by literature procedures[365]) was considered a potential active metabolite of Ru360 and **3.1** decomposition. The breaking of the μ-oxo bond from decomposition would release two mononuclear ruthenium species, with four ammine ligands in the equatorial plane, similar to trans-$[(NH_3)_4Cl_2Ru]^+$. However trans-$[(NH_3)_4Cl_2Ru]^+$ did not inhibit calcium uptake (Figure 5.4d), revealing this potential decomposition product is not active.

[2]To confirm the activity of the complexes on the MCU and not a different calcium transporter, we utilized yeast mitochondria expressing the human pore-forming subunit MCU, the essential regulator EMRE of the mitochondrial calcium uniporter, and a mitochondria-targeted aequorin as a luminescence-based calcium sensor.[168,185,366,367] Focusing on the compounds determined to work in the permeabilized cells assay (**3.1**, **4.1**, **4.2**), we measured the concentration-dependent inhibitory effect on calcium uptake. The dose-response curves, fit with the Hill Equation, revealed the Michaelis constant (k), a measure of the effectiveness of calcium uptake inhibition, for commercially available Ru360 to be 227 ± 20 nM (Figure 5.5a). Results for commercial Ru360 were notoriously inconsistent. Eight separate trials produced Michaelis constants between 466 nM and 153 nM, averaging to 279 ± 111 nM. This may be due to uncharacterized impurities. Ru360 is known to undergo aquation at the axial positions, therefore the differences in activity may be due to different levels of the aquated product. The analogue **3.1** (method 1) was found to be more potent with a constant of 38 ± 16 nM while preparations via methods 2 and 3 afforded similar potencies of k = 48 ± 10 and 50 ± 20 nM, respectively (Figure 5.5a). Remarkably, although **3.1** and Ru360 differ only by nature of the axial ligand, **3.1** demonstrates up to 10× greater inhibitory properties (Figure

[2]Thanks to Daniela Arduino in the group of Fabiana Perocchi for obtaining these data

5.5a). **4.1** and **4.2** also only differ in equatorial ligands and have inhibitory constants of 26 ± 3 nM and 1100 ± 50 nM, respectively (Figure 5.5b).

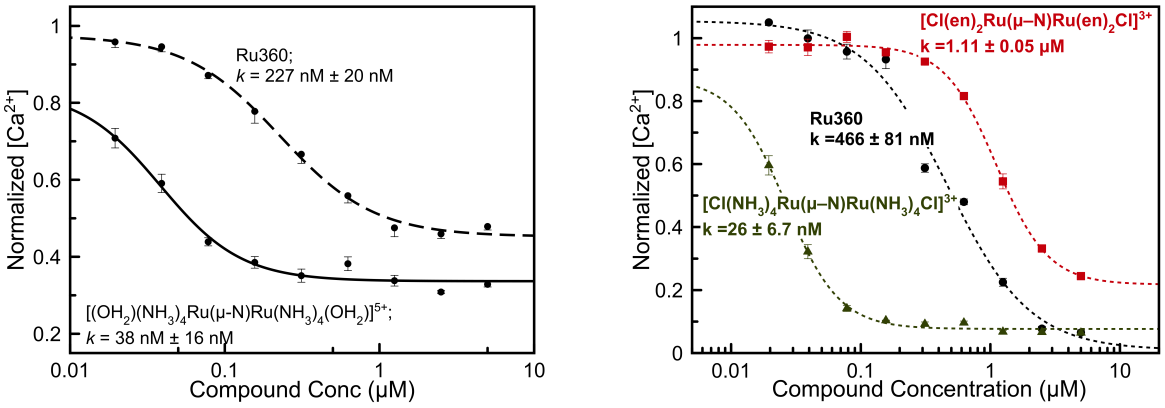

Figure 5.5: Dose response of the mitochondrial calcium uptake in isolated yeast mitochondria expressing the MCU (a) in the presence of Ru360, or **3.1** and (b) in the presence of Ru360, **4.1** or **4.2**. Figure reproduced in part with permission from *Inorg. Chem.*, **2017**, 56(6), pp 3123 - 3126. Copyright 2017, American Chemical Society.

[3]We then investigated the ability of each complex to inhibit calcium uptake in non-permeabilized cells. Non-permeabilized cells are more relevant to *in vivo* systems, taking into account differences in uptake mechanisms. HeLa cells were cultured and incubated with the cell permeant, mitochondrial targeting, calcium sensitive fluorescent dye Rho-2AM. Mitochondrial calcium uptake was stimulated by the addition of histimine.[368] Inhibition of mitochondrial calcium uptake by compound **3.1** was found to be inconsistent across two replicates and compound **4.2** did not show significant inhibition (Figure 5.6). However, compound **4.1** was found to inhibit calcium uptake significantly. This data is consistent with the Ru cellular uptake measurements. Compound **4.1** showed the most uptake in HeLa cells, and had the highest MCU inhibitory ability. Compound **4.2** had the worst cellular uptake and did not significantly inhibit mitochondrial calcium uptake.

[3]Thanks to Santhanam Shanmughapriya and Neeharika Nemani in the group of Madesh Muniswamy for obtaining these data

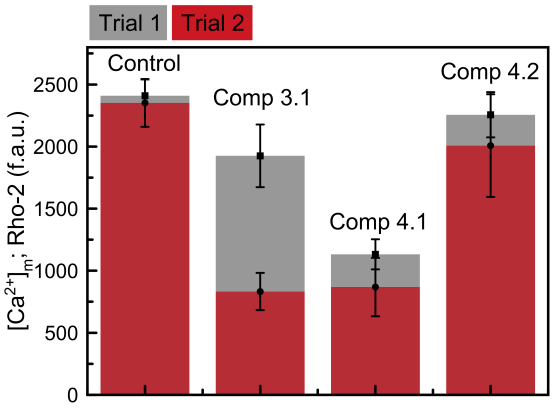

Figure 5.6: Calcium uptake inhibition of $[(OH_2)(NH_3)_4Ru(\mu\text{-}O)Ru(NH_3)_4(OH_2)]^{5+}$ (comp **3.1**), $[(Cl)(NH_3)_4Ru(\mu\text{-}N)Ru(NH_3)_4(Cl)]^{3+}$ (comp **4.1**), and $[Cl(en)Ru(\mu\text{-}N)Ru(en)Cl]^{3+}$ (comp **4.2**) in unpermeabilized HeLa cells measured by Rho-2 fluorescence. The variability between trials can be seen for compound **3.1**.

To further understand the mechanism of action of these complexes, two MCU mutants in isolated yeast mitochondria and isolated HEK293 mitochondria were investigated. The first study investigated the effect of the D261A mutant on inhibitor function. The D261 residue has been established as a key residue responsible for inhibition with Ru360; mutation of this residue to an alanine (D261A) will retain about 30% of protein function. However, the inhibitory ability of Ru360 is attenuated.[185,369] Molecular docking studies of mitoxantrone and Ru360 with the MCU showed significant hydrogen bonding interactions between this residue and these inhibitors.[185,186] To test the significance of the D261 residue on the mechanism of action of our compounds, **4.1** and **4.2** were incubated[4] in a dose-response manner with the D261A mutant expressed in yeast mitochondria.

[4]Thanks to Daniela Arduino in the group of Fabiana Perocchi for this data

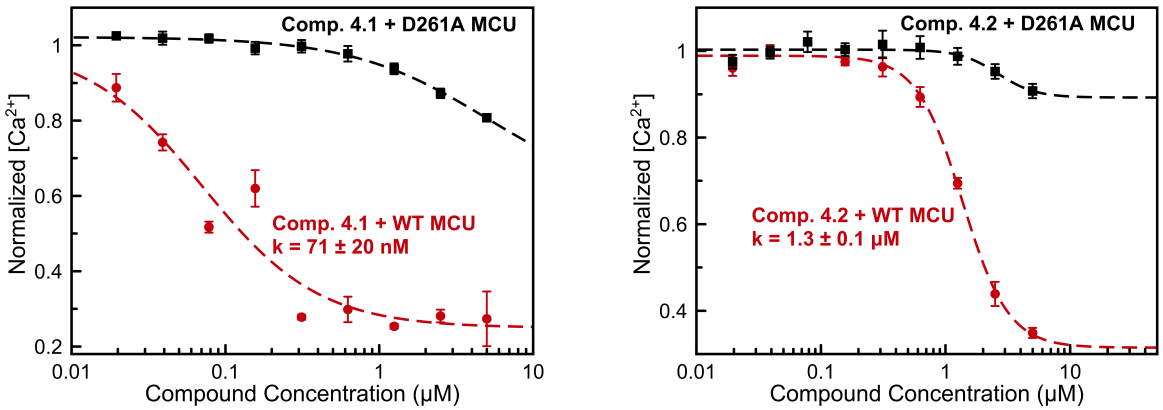

(a) (b)

Figure 5.7: Dose response of the mitochondrial calcium uptake in isolated yeast mitochondria expressing the D261A mutant MCU in the presence of (a) **4.1** and in the presence of (b) **4.2**.

In the D261A mutant compound **4.1** is ineffective (Figure 5.7a). Compound **4.2** was also tested on the D261A MCU mutant – the effect was similar (Figure 5.7b). This reveals that compounds **4.1** and **4.2** inhibit by interacting with the same aspartate (A261) residue as Ru360.[185]

The the S238A mutant has a similar effect as the D261A mutant – the protein function is maintained but Ru360-induced calcium inhibition is attenuated.[189] Hydrogen bonding was also observed between Ru360 and S238 in the aforementioned docking studies.[186]

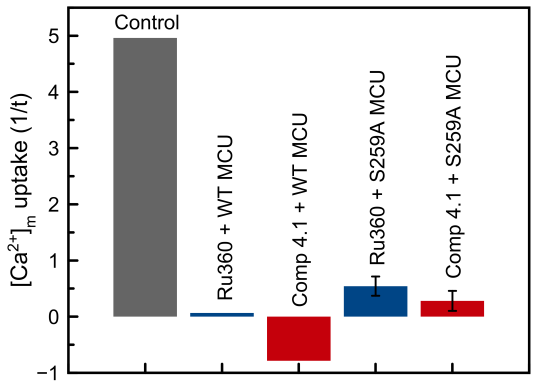

Figure 5.8: Inhibition of calcium uptake in HEK293 cells after mutation of the conserved serine to alanine; control: calcium uptake with no inhibitor

[5]Under constant concentration of compound **4.1** (10 nM) or Ru360 (500 nM) the S259A mutant showed a similar affect as the D261A mutant. The S259A and S238A are same residue, the difference in residue number is due to the differences in sequence between organisms. S238 is from the *C. elegans* MCU and S259 is from human-derived MCU. The S259A MCU had decreased protein function, however the inhibitors were less effective at blocking mitochondrial calcium uptake (Figure 5.8).

5.5 Conclusion

A number of dinuclear μ-nitrido and μ-oxo complexes were tested for biological activity. None of the complexes were found to be cytotoxic by the MTT assay. Three compounds, **3.1**, **4.1** and **4.2**, showed mitochondrial calcium uptake inhibition. Compound **4.1** had the highest cellular uptake in both HeLa and HEK293 cells and showed calcium uptake inhibition in unpermeabilized HEK293 cells. Compound **4.1** interacts with the MCU through

[5]Thanks to Santhanam Shanmughapriya and Neeharika Nemani in the group of Madesh Muniswamy for this data

a conserved serine and aspartate; mutations of these residues greatly reduced the complex's inhibitory ability.

Different axial ligand substitution kinetics may play an important role in the relative activity of these species. It is reported, for example, that the formate ligands of Ru360 aquate at a faster rate than the chloride analogue.[233] Additionally, the complex chemical environment of biological media contains a range of potential ligands that may affect the formation of the true active species. Using EPR, we showed that compound **3.1** is unstable over 24 hr in complete cell growth media, forming unknown EPR-active species. Considering the difference in activities between Ru360, which bears axial formate groups, and compound **3.1**, which bears axial water ligands, it appears that the nature of the axial ligands plays a large role in the inhibitory activity. The difference in inhibition constants is remarkable – **3.1** is 10× more effective. The difference between compound **4.1** (ammine equatorial ligands) and **4.2** (en equatorial ligands) is also striking – **4.1** is 36× more effective than **4.2**. Further modifications of the axial and equatorial ligands may lead to more effective MCU inhibitors by optimizing ligand substitution kinetics.

The difference in MCU-inhibitory activity of the complexes supports a two-part hypothesis for the mechanism of inhibition. First, the serine is tightly binding through the axial position of the complexes. Mutation of this serine greatly attenuates the MCU-inhibitory ability of these complexes. This could be either covalent, through a nucleophilic attack of the serine hydroxy to the electrophilic ruthenium to displace the axial ligand, or simply through a hydrogen-bonding interaction. As a formate group is both a poorer leaving group, and is less effective in hydrogen bonding in comparison to a water, the obtained data cannot differentiate between these two options. Second, the ability of the equatorial ligands to hydrogen bond with the aspartate residues mediates the inhibition. Compounds **4.1** and **4.2** only differ in their equatorial ligands. The ethylenediamine ligands of **4.2** cannot form hydrogen

bonds as effectively as **4.1**, and therefore is a less effective inhibitor. Compounds **4.3**-**4.5** have very poor hydrogen bonding capabilities, both in the axial and equatorial positions and no calcium uptake inhibition is observed.

A docking study looking at the interaction between Ru360 and the MCU corroborates the importance of the hydrogen bonding network with the equatorial ligands.[186] Structure activity relationship studies and docking studies with mitoxantrone indicate that long sidechain moieties with multiple hydrogen binding sides are necessary for inhibition.[185] Additional studies will be needed to consider the exact role of the axial vs equitorial ligands. Moreover, molecular biology studies to determine the method of cellular uptake and off-target protein interactions, and success in protection in ischemic-reperfusion injury models will elucidate the efficacy of these compounds for potential therapeutics.

APPENDIX A

EXPERIMENTAL DETAILS FOR $[(OH_2)(NH_3)_4RU(\mu-O)RU(NH_3)_4(OH_2)]^{5+}$

A.1 General methods and materials

Ruthenium trichloride hydrate ($RuCl_3 \cdot n\,H_2O$, 40% Ru) was purchased from Pressure Chemical and used as received. Ru360 was purchased from EMD Millipore Calbiochem (Lot # 2660892). Solvents, including concentrated HCl and NH_3, were ACS reagent grade and used as received. Purifications employed Dowex 50WX2 200-400 mesh (H^+ form) strongly acidic cation exchange resin, which was purchased from Alfa Aesar. Prior to chromatographic separation, the resin was treated 35 column volumes of 0.1 M HCl. $[Ru(NH_3)_5Cl]Cl_2$ and potassium μ-oxo-bis[pentachlororuthenate(IV)] were prepared via previously published procedures.[279,370]

A.2 Physical measurements

FTIR spectra were acquired on a Bruker Hyprion FTIR, with ZnSe ATR attachment for solid powders. Elemental analyses were performed by Atlantic Microlab, Inc. (Norcross, GA). Electrochemical measurements were carried out using a Pine Instruments WaveNow potentiostat. A three-electrode cell comprising a glassy carbon working electrode, a platinum counter electrode, and a Ag/AgCl reference electrode was used. Samples were dissolved to a final concentration of approximately 2-5 mM in 0.10 M pH 7.6 ammonium formate and were degassed with nitrogen for at least 15 minutes prior to analysis. UV-visible absorbance spectra were acquired with an Agilent Cary 8454 spectrophotometer. Near-IR absorbance spectra were collected on a Shimadzu 3600 UV-Vis/NIR spectrophotometer. Samples for electron paramagnetic resonance (EPR) spectroscopy were prepared in 20% glycerol/water solution

and frozen in liquid nitrogen in 4 mm thin wall quartz tubes. EPR spectra were recorded at a microwave frequency of 9.4 GHz on a BRUKER ELEXYS-II E500 spectrometer equipped with a liquid helium cryostat ESR10 in the ACERT center (National Biomedical Center for Advanced ESR Technology) at Cornell University. Concentrations of the Ru-containing solutions were determined by graphite furnace atomic absorption spectroscopy (GFAAS). A Perkin-Elmer PinAAcle 900Z GFAAS was used with end-capped graphite tubes, and certified calibration standards in the range of 25-100 μg/L were used to create suitable calibration curves. All solutions used in cellular studies were made in MilliQ 18 M$\cdot$ cm water. X-ray powder diffraction patterns (Figure A.1) were recorded on a Scintag Powder X-Ray Diffractometer in 2θ medium resolution Brag Brentano geometry employing Cu Kα line focused radiation at 40 kV, 44 mA power and equipped with a Ge crystal detector fitted with a 1.0 mm radiation entrance slit. Samples were mounted on zero background sample holders by dropping powders from a wide-blade spatula and then leveling the sample surface with the back of the spatula. No sample grinding was used. Samples were observed using a continuous 2θ scan from 1.5 – 50 °(Omega = 1.0 °). Orca (version 3.03) was used for all computations. DFT analysis used the BP86 functional and def2-TZVP(-f) basis set for geometry optimization. The ZORA correction was applied to account for relativist effects due to the presence of heavy atoms and the RI approximation was also applied for Coulomb integral approximations. TDDFT utilized the PBE0 functional with the RICOSX approximation. A solvent (water) correction was applied to all calculations using the COSMO function.

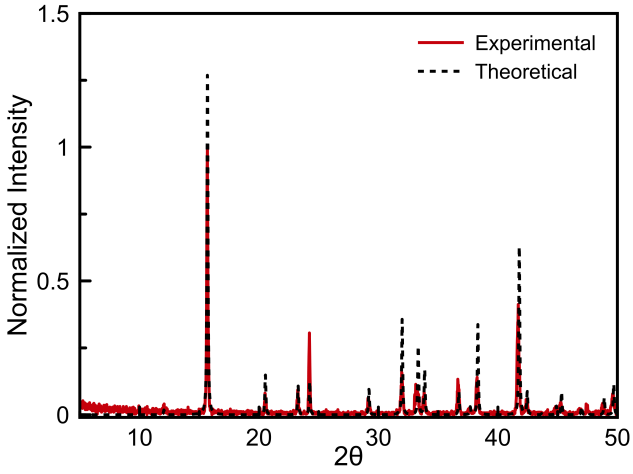

Figure A.1: X-ray powder diffraction pattern of $K_4[Ru_2OCl_{10}]$. Theoretical spectrum calculated from the crystal structure data using Mercury software (v. 3.8, Cambridge Crystallographic Data Centre).

A.3 Synthetic methods for $[(OH_2)(NH_3)_4Ru(\mu-O)Ru(NH_3)_4(OH_2)]^{5+}$ (3.1)

A.3.1 Method 1

This method was based on a previous literature protocol.[233] Ruthenium trichloride hydrate (250 mg, 1.11 mmol for the monohydrate) was refluxed in 1.5 mL 6 M HCl and 1 mL ethanol for 1 hr to reduce Ru(IV) and nitrosyl-containing impurities. A 250 μL volume of d=0.88 NH_4OH was added, and a dark red-brown solid precipitated immediately. This mixture was centrifuged while still warm. The supernatant was discarded, and 20 mL of d=0.88 NH_4OH was added to the remaining solid. The reaction was heated at 90 °C for 5 min and then allowed to stir at 40 °C overnight. The crude product was precipitated with approximately 60 mL ethanol, and the resulting suspension was chilled at 4 °C. The compound was

isolated by centrifugation, dissolved in ∼20 mL 0.1 M HCl, and loaded immediately onto a DOWEX 50WX2 cation exchange column (5 g resin for 1/2 of the crude product, 10 mm diameter column) pre-equilibrated with 0.1 M HCl. The desired complex was eluted using 1-3 M HCl gradient, with the product beginning to move at 2 M and completely eluting at 3 M. A yellow byproduct, $[Ru(NH_3)_5Cl]Cl_2$, elutes at 1.5 M HCl, and ruthenium red and related impurities elute at as the HCl concentration is increased to 4 M. Fractions containing only the 360 and 600 nm absorbance bands were pooled and evaporated to dryness to obtain the compound as a green-brown solid **3.1**. Yield: 18 mg (2.7%). Elemental analysis: calcd % for $[(OH_2)(NH_3)_4Ru(\mu-O)Ru(NH_3)_4(OH_2)]Cl_5 \cdot 1.5H2O$: C 0.00, H 5.25, N 18.84, Cl 29.81%; found: C 0.00, H 4.95, N 18.39, Cl 29.96.

A.3.2 Method 2

$[Ru(NH_3)_5Cl]Cl_2$ (100 mg, 0.34 mmol) was dissolved in 50 mL 1 M NH_4OH, heated at 60 °C for 6 hr in a loosely capped 200 mL round-bottom flask, and then left to stir at room temperature for 3 days. The pH of the resulting green solution was adjusted with concentrated HCl to <7, resulting in a color change of the solution from green to brown, and then loaded immediately on a DOWEX 50WX2 cation exchange column (5 g resin, 10 mm diameter column) pre-equilibrated with 0.1 M HCl. The compound was isolated from this column as described in method 1. Yield: 20 mg (9.8%).

A.3.3 Method 3

$K_4[Ru_2OCl_{10}]$ (50 mg, 0.11 mmol) was suspended in 50 mL d=0.88 NH_4OH and heated at 50 °C in a loosely capped 200 mL round-bottom flask for 30 min. The reaction mixture was filtered while hot through a pad of Celite. To the dark green filtrate was added 150

mL of ethanol, and the resulting suspension was cooled at 4 °C for 1-2 hr. The green solid was isolated by centrifugation, dissolved in 0.1 M HCl (∼20 mL), and loaded on a DOWEX 50WX2 cation exchange column (5 g resin, 10 mm diameter) pre-equilibrated with 0.1 M HCl. The compound was eluted as described above. It should also be noted that a purple-pink impurity sometimes eluted at the tail end of the fraction containing the compound, so additional care must was to avoid contamination of the desired product. Yield: 5 mg (7.6%).

A.4 X-ray crystallography

Red prisms of $[(OH_2)(NH_3)_4Ru(\mu{-}O)Ru(NH_3)_4(OH)]^{4+}$ were grown by the vapor diffusion of ethanol into an aqueous solution of **3.1**. Crystals of $K_4[Ru_2OCl_{10}]$ were grown by the slow evaporation of a 2.5 M HCl solution at elevated temperatures. Crystals of $[Ru(NH_3)_5Cl]Cl_2$ were obtained directly from the cation exchange purification of **3.1** via slow evaporation of the fractions containing 2 M HCl. X-ray diffraction data for $[(OH_2)(NH_3)_4Ru(\mu{-}O)Ru(NH_3)_4(OH)]^{4+}$, $[Ru(NH_3)_5Cl]Cl_2$ and $K_4[Ru_2OCl_{10}]$ were collected on a Bruker APEX 2 CCD Kappa diffractometer (Mo Kα, $\lambda = 0.71073$ Å) at 223 K. The structures were solved through intrinsic phasing using SHELXT[371] and refined against F^2 on all data by full-matrix least squares with SHELXL[372] following established refinement strategies.[373] All non-hydrogen atoms were refined anisotropically. Hydrogen atoms of NH_3 ligands were included in the model at geometrically calculated positions and refined using a riding model, allowing the torsion angle to refine (HFIX 137). The OH hydrogen atom of $[(OH_2)(NH_3)_4Ru(\mu{-}O)Ru(NH_3)_4(OH)]^{4+}$ was located on the difference Fourier map, and refined semi-freely, constraining the O–H distance to 0.83 Å and the thermal ellipsoid of the H atom to be 1.5 times that of the oxygen atom. In the structure of $[(OH_2)(NH_3)_4Ru(\mu{-}O)Ru(NH_3)_4(OH)]^{4+}$, heavily disordered electron density, centered around a crystallographic inversion center, could not be satisfactorily refined as discrete sol-

vent molecules. This residual electron density was modeled using the SQUEEZE function in PLATON.[374] Residual electron density in a solvent-accessible void of 36.8 Å^3 accounts for approximately 11 e-. We hypothesize that this density corresponds to a disordered water molecule (10 e-). Details of the data quality and a summary of the residual values of all the refinements are listed in Tables A.1, A.2, A.3, and 3.1.

Table A.1: Selected distances and angles for $[Ru(NH_3)_5Cl]Cl_2$. Labels are as shown in Figure 3.3a. Numbers in parentheses are the estimated standard deviation in the last significant figures.

Interatomic Distances [Å]		Interatomic Angles [°]	
N1–Ru	2.082(3)	N2-Ru-Cl1	90.69(8)
N2–Ru	2.111(3)	N4-Ru-Cl1	89.71(5)
N3–Ru	2.107(3)	N1-Ru-N2	89.40(12)
N4–Ru	2.100(2)	N1-Ru-N3	89.33(12)
Cl1–Ru	2.3494(8)	N1-Ru-N4	90.29(5)
		N2-Ru-N4	89.94(5)
		N3-Ru-N4	90.07(5)

Table A.2: Selected bond distances and angles for $K_4[Ru_2OCl_{10}]$. Labels are as shown in Figure 3.3b. Numbers in parentheses are the estimated standard deviation in the last significant figures.

Interatomic Distances [Å]		Interatomic Angles [°]	
Cl1–Ru1	2.3185(16)	O1-Ru1-Cl1	180.00
Ru1–O1	1.8066(6)	Cl2-Ru1-Cl1	87.12(2)
Ru1–Cl2	2.3672(8)	Cl2-Ru1-O1	92.88(2)

Table A.3: Selected bond distances and angles for Ru360 analog. Labels are as shown in Figure 3.5. Numbers in parentheses are the estimated standard deviation in the last significant figures.

Interatomic Distances [Å]		Interatomic Angles [°]	
O2–Ru	1.8218(2)	Ru-O2-Ru	180.000(12)
Ru–O1	2.039(2)	O1-Ru-O2	178.45(7)
N3–Ru	2.110(3)	N1-Ru-N2	91.33(10)
N4–Ru	2.108(2)	N1-Ru-N4	88.80(10)
N1–Ru	2.105(3)	N2-Ru-N3	89.56(10)
N2–Ru	2.102(2)	N3-Ru-N4	90.18(10)
		N1-Ru-O1	88.32(10)
		N1-Ru-O2	90.66(7)
		N2-Ru-O1	89.91(9)
		N2-Ru-O2	91.28(6)
		O2-Ru-N4	92.52(6)
		O1-Ru-N4	86.30(9)
		N2-Ru-N4	176.20(9)
		O2-Ru-N3	91.43(7)
		O1-Ru-N3	89.58(10)
		N1-Ru-N3	177.72(10)

A.5 Aqueous stability

Stock solutions of **3.1** for use in biological studies were made in MilliQ 18 MΩ·cm water to final concentrations ranging from 1-5 mM. Aliquots were stored at –20 °C in between use for short term stability. The stability of the stock solutions to freeze-thaw cycles was determined by analyzing the UV-Vis spectrum of a solution before and after five freeze-thaw cycles, over the course of five days. UV-vis spectroscopy revealed that the compound remained approximately 90% intact after being subjected to these conditions as well. To assess long term stability of the complex, the stock solution was frozen at –80 °C for three months. The UV-Vis spectrum was measured after this time, and the sample was determined to be greater than 90% pure based on the intensities of the absorbance bands.

Solutions of complex **3.1** (1 mM) were dissolved in 1× PBS with 5 mol equivalent of glutathione and incubated at 37 °C. Samples were taken at t = 0 and t = 24 hr to assess stability. 20% glycerol was added to the samples and were analyzed by EPR at 20 K. Solutions of complex **3.1** (0.5 mM) in DMEM containing 10% FBS (fetal bovine serum) were incubated at 37 °C for 24 hr. Samples were taken at t = 0 and t = 24 hr to access stability. 20% glycerol was added to the samples and were analyzed by EPR at 20 K.

APPENDIX B

EXPERIMENTAL DETAILS FOR SUBSTITUTED DIRUTHENIUM μ-NITRIDO SYSTEMS

B.1 General methods and materials

Ruthenium trichloride hydrate ($RuCl_3 \cdot n\,H_2O$, 40% Ru) was purchased from Pressure Chemical and used as received. Ru360 was purchased from EMD Millipore Calbiochem (Lot # 2660892). Solvents, including concentrated HCl and NH_3, were ACS reagent grade and used as received. Potassium chloride, stannous chloride and potassium nitrite were purchased from Macron Fine Chemicals, Fisher Scientific and Alfa Aesar, respectively, and used as received. $K_2[RuCl_5NO]$ and $K_3[Ru_2NCl_8(H_2O)_2]$ were prepared based on previously published procedures.[306,307] 2,2'-bipyridine (bpy) was obtained from Alfa Aesar. 4,4'-dimethoxy-2,2'-bipyridine (dmobpy) and 4,4'-dimethyl-2,2'-bipyridine (dmbpy) were purchased from Sigma-Aldrich and used as received.

B.2 Physical measurements

FTIR spectra were acquired on a Bruker Hyprion FTIR, with ZnSe ATR attachment for solid powders. Elemental analyses were performed by Atlantic Microlab, Inc. (Norcross, GA). UV-visible absorbance spectra were acquired with an Agilent Cary 8454 spectrophotometer. Conductance measurements were performed using a Sper Scientific model 860032 conductivity meter. Extinction coefficients of **4.1** and **4.2** were taken in pH 7.4 1×PBS and **4.3**, **4.4** and **4.5** were taken in DMSO. ^{1}H NMR were acquired on a 400 MHz INOVA spectrometer or a 500 MHz Bruker AV 3HD spectrometer equipped with a broadband Prodigy cryoprobe. $^{13}C\{^1H\}$ NMR spectra were acquired on a 500 MHz Bruker AV 3HD spectrometer

equipped with a broadband Prodigy cryoprobe. A Pine Instruments WaveNow potentiostat and a three electrode cell including a glassy carbon working electrode, a platinum counter electrode, and a silver reference electrode were used to acquire cyclic voltammograms at a scan rate of 100 mV/s. Compounds were dissolved in a 0.10 M solution of $[Bu_4N][PF_6]$ in DMF. Nitrogen gas was bubbled into the solution to deoxygenate the cell before analysis. An internal standard, ferrocene (0.45 V vs SCE), was used to reference the potentials.[375,376] Orca (version 3.03) was used for all computations. DFT analysis used the BP86 functional and def2-TZVP(-f) basis set for geometry optimization and vibrational frequency calculations. The ZORA correction was applied to account for relativist effects due to the presence of heavy atoms and the RI approximation was also applied for Coulomb integral approximations. TDDFT utilized the PBE0 functional with the RICOSX approximation. A solvent (water or DMSO) correction was applied using the COSMO function.

B.3 Synthetic methods

B.3.1 Synthesis of $K_2[Ru(Cl)_5NO]$ (4.SM1)

$RuCl_3 \cdot n\,H_2O$ (1g, 4.82 mmol (monohydrate)) and KNO_2 (1.3 g, 15.3 mmol) were combined and refluxed in 20 mL of 0.5 M HCl for one hour. To the red solution KCl (1.13 g, 15.2 mmol) and 3 mL 11.6 M HCl were added and reflux was continued for 3 hrs. The resulting magenta solution was heated at 106 °C under air stream to remove solvent until dark purple crystals started to form (∼5 mL solvent remaining). The crystals were filtered and washed with copious amounts of 50% ethanol in water, ethanol, ether and then air dried. Yield: 750 mg, 43% yield.

B.3.2 Synthesis of $K_3[Ru_2NCl_8(H_2O)_2]$ (4.SM2)

$SnCl_2$ (1.27 g, 6.69 mmol) was dissolved in 2.5 mL of 6 M HCl and added to **4.SM1** (1 g, 2.58 mmol) in 15 mL H_2O and refluxed for 1 hour to form a red-brown solution. The solvent was evaporated at 104 °C under an air stream until red-brown crystals crashed out (2-5 mL left). The crystals were filtered and washed with 50% ethanol in water, ethanol, ether and air dried. Yield: 325 mg, 38% yield.

B.3.3 Synthesis of $[Ru_2N(NH_3)_8(H_2O)_2]Cl_5$ (4.1)

182 mg (0.278 mmol) of $K_3[Ru_2NCl_8(H_2O)_2]$ was dissolved in 50 mL of d=0.88 NH_4OH[293] and heated in a loosely stoppered flask at 75 °C for 6 hours to yield a clear bright orange solution with a fine grey-brown precipitate. The precipitate was assumed to be residual SnO_2 left over from the formation of **4.SM2**. The reaction was cooled, filtered and the filtrate concentrated to dryness by rotory evaporation. The crude solid was dissolved in 25 mL of hot water, precipitated via the addition of 5 mL concentrated HCl, cooled overnight, filtered and washed with 6 M HCl, ethanol and diethyl ether to yield crude orange microcrystalline solid (83 mg). Pure complex was recrystallized by acetone diffusion into aqueous solutions over 1-2 weeks. Yield after filtering and washing with ethanol and diethyl ether: 39 mg, 26% yield. ^{1}H NMR (400 MHz, DMSO-d_6): δ 4.14 (s, 24H). IR (ATR, cm^{-1}): 1047(s). Elemental analysis: calcd % for $Ru_2N(NH_3)_8(Cl)_2Cl_3 \cdot 1.5\,H_2O$: C 0.77, H 4.99, N 22.38, Cl 31.46%; found: C 0.73, H 4.42, N 21.84, Cl 30.29%.

B.3.4 Synthesis of $[Ru_2N(en)_4(Cl)_2]Cl_3$ (4.2)

100 mg (0.153 mmol) of $K_3[Ru_2NCl_8(H_2O)_2]$ was suspended in 1 mL H_2O and warmed.[294] 1 mL of ethylenediamine (en) was combined with 1 mL H_2O and stirred on a 90 °C oil bath. After about 5 minutes, the **4.SM2** solution was added to the hot ethylenediamine solution and then heated for 1 hour. After cooling and filtering, 30 mL of ethanol was added and the reaction cooled overnight. The crude product was isolated by centrifugation and dissolved in 4-6 mL water. The addition of 1-2 mL of concentrated HCl and chilling overnight precipitates pure orange microcrystals. Yield after filtering and washing with ethanol and diethyl ether: 28 mg, 28% yield. ^{1}H NMR (400 MHz, D_2O vs dioxane): δ 5.49 (bs, 8H), 5.33 (bs, 8H), 3.28 (m, 8 H), 2.85 (m, 8H). $^{13}C\{^1H\}$ NMR (125 MHz, D2O): 46.44. IR (ATR, cm-1): 1055(s). Elemental analysis: calcd% for $Ru_2N(C_2N_2H_8)_4Cl_5{\cdot}2.5H_2O$: C 14.15, H 5.49, N 18.57%; found: C 14.20, H 5.26, N 18.19%.

B.3.5 Synthesis of $[Ru_2N(bpy)_2Cl_5(DMF)]$ (4.3)

Suspensions of $K_3[Ru_2NCl_8(H_2O)_2]$ (300 mg, 0.459 mmol) and 2,2'-bipyridine (358 mg, 2.295 mmol) in 3 mL of water and 7 mL of acetone, respectively, were warmed at 45 °C for 10 min to ensure full dissolution of these compounds. Once dissolved, the resulting solutions were mixed and heated under reflux for 8 h. The resulting red-brown crude solid was isolated by filtration and washed with acetone and diethyl ether. This crude solid (180 mg) was suspended in DMF (12 mL), sonicated for 15 min, stirred at rt for 30 min, and then filtered. The vapor diffusion of methanol into the resulting dark red filtrate afforded red crystals of the desired compound after a week. Yield: 60 mg, 16% yield. ^{1}H NMR (600 MHz, DMSO-d_6): 9.98 (dd, J = 5.6 and 1.5 Hz, 1H), 9.61 (dd, J = 5.7 and 1.5Hz, 2H), 8.85 (dd, J = 5.6 and 1.7 Hz, 1H), 8.71 (d, J = 8.0 Hz, 2H), 8.61 (d, J = 8.1 Hz, 1H), 8.53 (d, J

= 8.2 Hz, 1H), 8.39 (td, J = 7.8 and 1.5 Hz, 2H), 8.20 (td, J = 7.9 and 1.5 Hz, 1H), 8.16 (td, J = 7.8 and 1.7 Hz, 1H), 7.84 (ddd, J = 7.8, 5.6, and 1.3 Hz, 2H), 7.75 (ddd, J = 7.8, 5.6, and 1.3 Hz, 1H), 7.61 (ddd, J = 7.8, 5.5 and 1.0 Hz, 1H). $^{13}C\{^1H\}$ NMR (125 MHz, DMSO-d_6): 158.18, 155.45, 154.74, 153.33, 152.71, 149.20, 140.94, 140.14, 139.38, 126.09, 126.02, 125.76, 123.56, 123.27, 122.55. IR (ATR, cm^{-1}): 1030(s) and 1074(w). Anal. calcd for **4.5**, $C_{23}H_{23}Cl_5N_6ORu_2$: C, 35.47; H, 2.98; N, 10.79%. Found: C, 35.27; H, 3.50; N, 10.53%.

B.3.6 Synthesis of $[Ru_2N(dmbpy)_2Cl_5(DMF)]$ (4.4)

Suspensions of $K_3[Ru_2NCl_8(H_2O)_2]$ (300 mg, 0.459 mmol) and 4,4'-dimethyl-2,2'-bipyridine (338 mg, 1.836 mmol) in 3 mL of water and 7 mL of acetone, respectively, were warmed at 45 °C for 10 min. The resulting acetone suspension and aqueous solution were mixed and heated under reflux for 6 h. The resulting red-brown crude solid was isolated by filtration and washed with chloroform and diethyl ether. To further purify the complex from excess dmbpy ligand, the crude solid was suspended in 10 mL of chloroform and heated under reflux for 2 h, and then isolated again by filtration while still warm. As a final means of purification, the solid (120 mg) was suspended in 6 mL of DMF, sonicated for 30 min, stirred at rt for 1 h, and then filtered. The dark red filtrate, which contains pure product, was subjected to vapor diffusion with methanol. Over the course of the week, red crystals of the desired product were obtained. Yield: 14 mg, 3.5% yield. Note: additional batches of pure product can be obtained by repeating the sonication procedure with the crude solid. The product is only sparingly soluble in DMF, so the isolation of more compound requires repeated extractions in this solvent. ^1H NMR (600 MHz, DMSO-d_6): 9.77 (d, J = 5.8 Hz, 1H), 9.40 (d, J = 5.6 Hz, 2H), 8.67 (d, J = 5.7 Hz, 1H), 8.55 (s, 2H), 8.45 (s, 1H), 8.37 (s, 1H), 7.65 (d, J = 6.0 Hz, 2H), 7.56 (d, J = 5.9Hz, 1H), 7.42 (d, J = 5.9 Hz, 1H), 2.60(s,

2H), 2.59 (s, 1H), 2.45 (s, 1H). $^{13}C\{^1H\}$ NMR (125 MHz, DMSO-d_6): 157.67, 154.67, 154.24, 153.10, 152.48, 151.84, 151.76, 150.99, 148.45, 126.70, 126.38, 126.18, 123.97, 123.66, 122.94, 21.00, 20.80, 20.43. IR (ATR, cm^{-1}): 1020(w), 1032(s), 1065(s), and 1084(w). Anal. calcd for **4.4**, $C_{27}H_{35}Cl_5N_6O_3Ru_2$: C, 37.23; H, 4.05; N, 9.65%. Found: C, 37.27; H, 4.17; N 9.60%.

B.3.7 Synthesis of $[Ru_2N(dmobpy)_2Cl_5(DMF)]$(4.5).

Suspensions of $K_3[Ru_2NCl_8(H_2O)_2]$ (300 mg, 0.459 mmol) and 4,4'-dimethoxy-2,2'-bipyridine (397 mg, 1.836 mmol) in 3 mL of water and 7 mL of acetone, respectively, were warmed at 45 °C for 10 min. The resulting acetone suspension and aqueous solution were mixed and heated under reflux for 6 h. The resulting red-brown crude solid was isolated by filtration and washed with chloroform and diethyl ether. To remove excess dmobpy ligand, the crude solid was suspended in 10 mL of chloroform and heated under reflux for 2 h, and then isolated again by filtration. For further purification, the solid was then suspended in 10 mL of 6:4 acetone:water, heated at reflux for 4 h, and then filtered. This crude solid (120 mg) was suspended in 12 mL of DMF, sonicated for 30 min, stirred at rt for 1 h, and then filtered. The dark red filtrate, which contains pure product, was subjected to vapor diffusion with methanol to afford the product as red crystals. Yield: 22 mg, 5.3% yield. Note: as described above, more pure product can be obtained by sequential extractions of the remaining crude solid with DMF as described. ^1H NMR (600 MHz, DMSO-d_6): 9.71 (d, J = 6.6 Hz, 1H), 9.35 (d, J = 6.7 Hz, 2H), 8.66 (d, J = 6.5 Hz, 1H), 8.29 (d, J = 2.8 Hz, 2H), 8.22 (d, J = 2.8 Hz, 1H), 8.10 (d, J = 2.5 Hz, 1H), 7.42 (dd, J = 6.7 and 2.7 Hz, 2H), 7.34 (dd, J = 6.7 and 2.7 Hz, 1H), 7.21 (dd, J = 6.6 and 2.5 Hz, 1H), 4.08 (s, 2H), 4.07 (s, 1H), 3.97 (s, 1H). $^{13}C\{^1H\}$ NMR (125 MHz, DMSO-d_6): 168.29, 167.90, 167.70, 159.35, 156.27, 155. 67, 155.00, 153.61, 150.21, 111.65, 111.19, 110.80, 109.83, 108.90, 57.00, 56.87, 56.71. IR (ATR, cm^{-1}): 1015(s), 1030(vs), 1049(vs), 1065(s), and 1074(vw). Anal. calcd for **4.5**,

$C_{27}H_{31}Cl_5N_6O_5Ru_2$: C, 36.07; H, 3.48; N, 9.35%. Found: C, 35.80; H, 3.64; N, 9.15%.

B.4 X-ray crystallography

Low-temperature X-ray diffraction data for compound **4.2** were collected on a Rigaku XtaLAB Synergy diffractometer coupled to a Rigaku Hypix detector with Cu Kα radiation (λ = 1.54184 Å), from a PhotonJet micro-focus X-ray source at 100 K. The diffraction images were processed and scaled using the CrysAlisPro software.[377] Low-temperature X-ray diffraction data for **4.1** and **4.SM2** were collected on a Bruker APEX 2 CCD Kappa diffractometer (Mo Kα, λ = 0.71073 Å) at 223 K. The diffraction images were processed and scaled using the APEX2 software.[378] The structures were solved through intrinsic phasing using SHELXT[371] and refined against F^2 on all data by full-matrix least squares with SHELXL[372] following established refinement strategies.[373] All non-hydrogen atoms were refined anisotropically. All hydrogen atoms bound to carbon were included in the model at geometrically calculated positions and refined using a riding model. Hydrogen atoms bound to nitrogen in **4.2** and oxygen in **4.SM2** were located in the difference Fourier synthesis and subsequently refined semi-freely with the help of distance restraints. The isotropic displacement parameters of all hydrogen atoms were fixed to 1.2 times the Ueq value of the atoms they are linked to (1.5 times for methyl groups). The unit cell of **4.1** contained disordered solvent molecules, which have been treated as diffuse contributions to the overall scattering without specific atom positions using the solvent mask routine in Olex2.[379] The unit cell of **4.3** contained 3 methanol molecules and the unit cell of **4.5** contained three DMF molecules, which have been treated as diffuse contributions to the overall scattering without specific atom positions using the solvent mask routine in Olex2. Details of the data quality and a summary of the residual values of the refinements are listed in Tables B.2, B.3, B.4, B.1, B.5, B.6, 4.1, and 4.2.

Table B.1: Unit Cell Parameters for $K_2[RuCl_5NO]$.

	Crystal Data
Morphology	Block
Crystal System	Orthorhombic
Volume/ Å^3	960
a/Å	6.91
b/Å	10.42
c/Å	13.35
$\alpha/^\circ$	90
$\beta/^\circ$	90
γ°	90

Table B.2: Relevant distances and angles for $K_3[Ru_2NCl_8(H_2O)_2]$. Labels are as shown in Figure 4.2a. Numbers in parentheses are the estimated standard deviation in the last significant figures.

Interatomic Distances [Å]		Interatomic Angles [°]	
Cl1–Ru	2.3858(4)	N1-Ru-O1	179.99(5)
O1–Ru	2.1790(17)	Ru-N-Ru	180.0
Cl2–Ru	2.3699(4)	Cl2-Ru-Cl1	171.595(16)
N1–Ru	1.7251(2)	Cl1-Ru-O1	84.95(4)
		Cl2-Ru-O1	86.65(4)
		Cl1-Ru-N1	95.038(12)
		Cl2-Ru-N1	93.359(12)

Table B.3: Selected bond distances and angles for $[(OH)(OH_2)(NH_3)_8Ru_2(\mu{-}N)](SiF_6)_2$. Labels are as shown in Figure 4.4a. Numbers in parentheses are the estimated standard deviation in the last significant figures.

Interatomic Distances [Å]		Interatomic Angles [°]	
N1–Ru	1.7374(3)	Ru-N1-Ru	180.0
Ru–O1	2.082(2)	O1-Ru-N1	179.52(6)
N2–Ru	2.101(3)	N1-Ru-N2	93.67(8)
N3–Ru	2.102(2)	N1-Ru-N3	94.05(6)
N4–Ru	2.108(2)	N1-Ru-N4	96.70(7)
		N3-Ru-N4	89.36(6)
		N2-Ru-N3	89.90(6)
		N2-Ru-O1	86.82(10)
		N3-Ru-O1	85.94(6)
		N4-Ru-O1	82.82(10)
		N2-Ru-N4	169.64(10)

Table B.4: Selected bond distances and angles for $[Cl(en)_2Ru(\mu-N)Ru(en)_2Cl]Cl_3$. Labels are as shown in Figure 4.4b. Numbers in parentheses are the estimated standard deviation in the last significant figures.

Interatomic Distances [Å]		Interatomic Angles [°]	
N1–Ru	1.7592(3)	Ru-N1-Ru	176.3(2)
N2–Ru	2.105(3)	N1-Ru-Cl1	177.59(10)
N3–Ru	2.104(3)	N1-Ru-N2	95.46(10)
N4–Ru	2.106(3)	N1-Ru-N3	96.21(15)
N5–Ru	2.108(3)	N1-Ru-N4	95.12(9)
Cl1–Ru	2.4550(8)	N1-Ru-N5	94.58(14)
		N2-Ru-Cl1	84.03(8)
		N2-Ru-N4	169.26(11)
		N2-Ru-N5	99.05(10)
		N3-Ru-Cl1	86.05(8)
		N3-Ru-N2	81.58(10)
		N3-Ru-N4	95.49(10)
		N3-Ru-N4	169.09(11)
		N4-Ru-Cl1	85.47(8)
		N4-Ru-N4	81.87(10)
		N4-Ru-Cl1	83.19(8)

Table B.5: Selected bond distances and angles for $[Ru_2N(bpy)_2Cl_5(DMF)]$. Labels are as shown in Figure 4.6a. Numbers in parentheses are the estimated standard deviation in the last significant figures.

Interatomic Distances [Å]		Interatomic Angles [°]	
N3–Ru1	2.0548(14)	Ru2-N1-Ru1	173.10(9)
N4–Ru2	2.0532(14)		
N5–Ru2	2.0607(15)		
N2–Ru1	2.1626(14)		
Ru1–N1	1.7351(14)		
Ru2–N1	1.7256(13)		

Table B.6: Selected bond distances and angles for $[Ru_2N(dmobpy)_2Cl_5(DMF)]$. Labels are as shown in Figure 4.6b. Numbers in parentheses are the estimated standard deviation in the last significant figures.

Interatomic Distances [Å]		Interatomic Angles [°]	
N3–Ru1	2.0646(18)	Ru2-N1-Ru1	177.22(11)
N4–Ru2	2.0567(18)		
N5–Ru2	2.0596(19)		
N2–Ru1	2.1546(19)		
Ru1–N1	1.7375(18)		
Ru2–N1	1.7219(18)		

B.5 Aqueous kinetics

Stock solutions of **4.1** and **4.2** were made in MilliQ 18 M·cm water to final concentrations ranging from 1 to 3 mM. Solutions were used immediately. Various concentrations of of $HClO_4$ were used to probe pH dependence between pH 1 and 3.5.

B.6 Conductivity

Solutions of **4.1** and **4.2** were made in MilliQ 18 M·cm water to final concentrations ranging from 0.45 to 0.5 mM.

B.7 NMR spectra

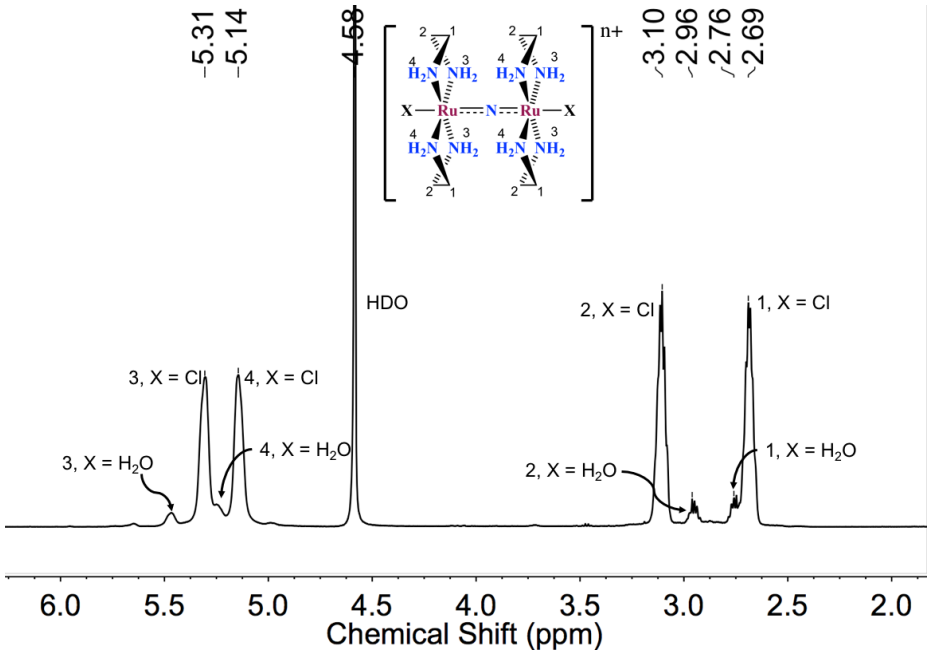

Figure B.1: ^{1}H NMR of Compound **4.2** in D_2O.

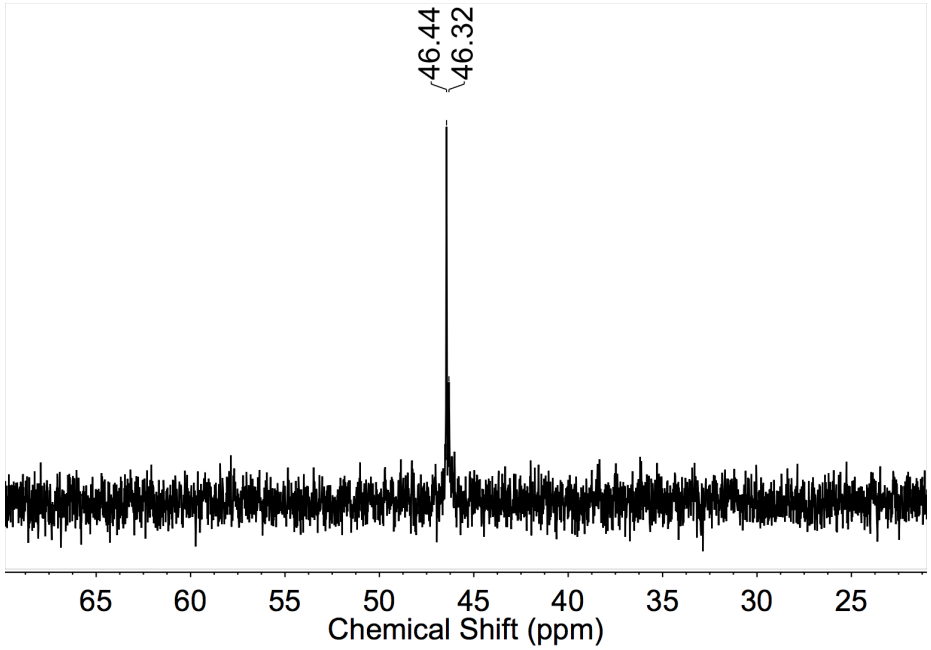

Figure B.2: $^{13}C\{^{1}H\}$ NMR of Compound **4.2** in D_2O.

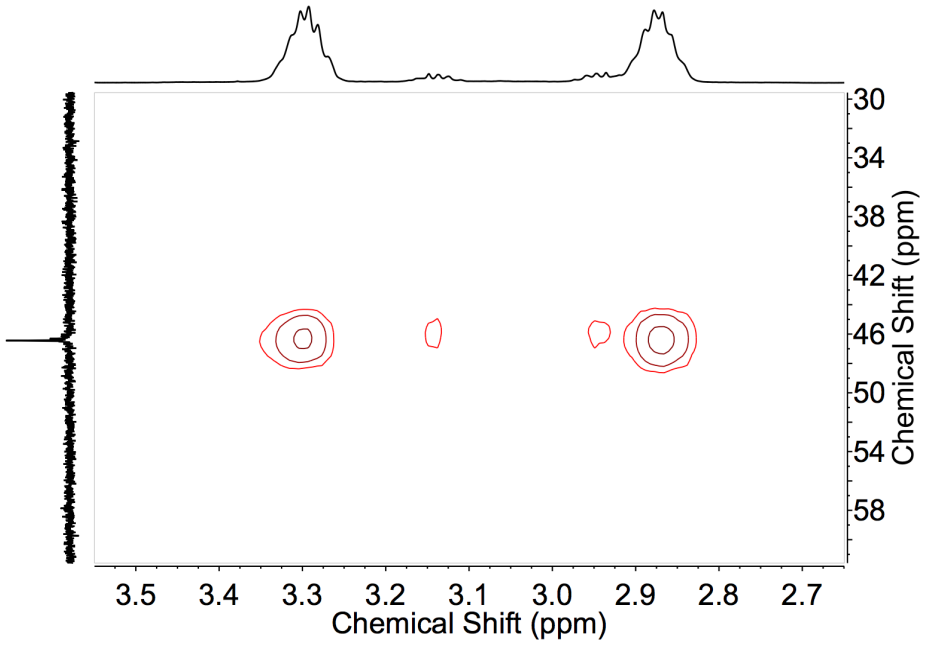

Figure B.3: $^{13}C\{^{1}H\}/^{1}H$ HSQC NMR of Compound **4.2** in D_2O. The cross peaks show the smaller, inner peaks at 2.96 and 2.76 ppm in the proton NMR are associated with the small peak at 46.32 ppm in the ^{13}C NMR.

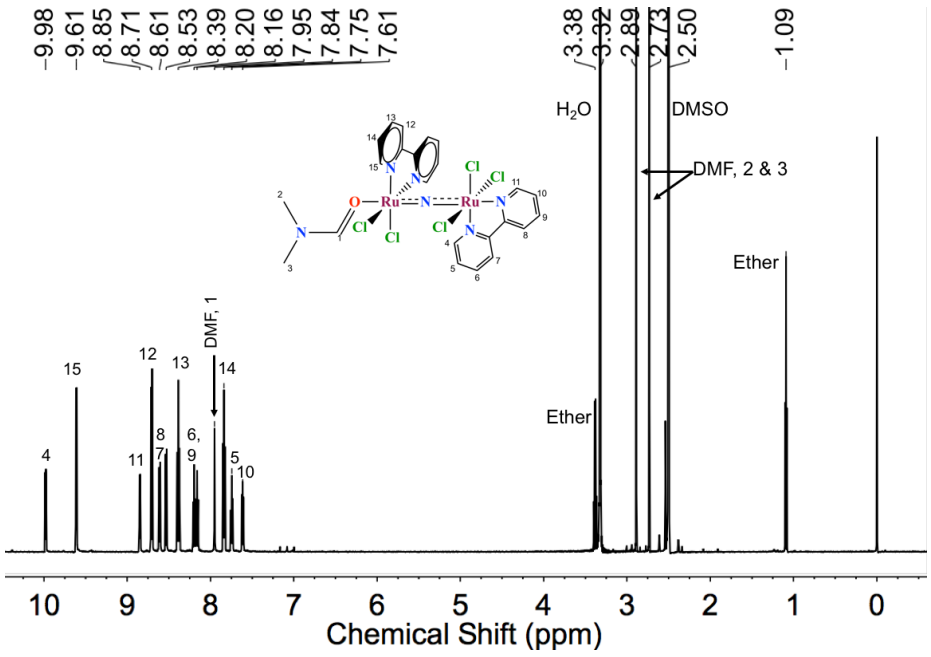

Figure B.4: ^{1}H NMR of Compound **4.3** in DMSO-d_6.

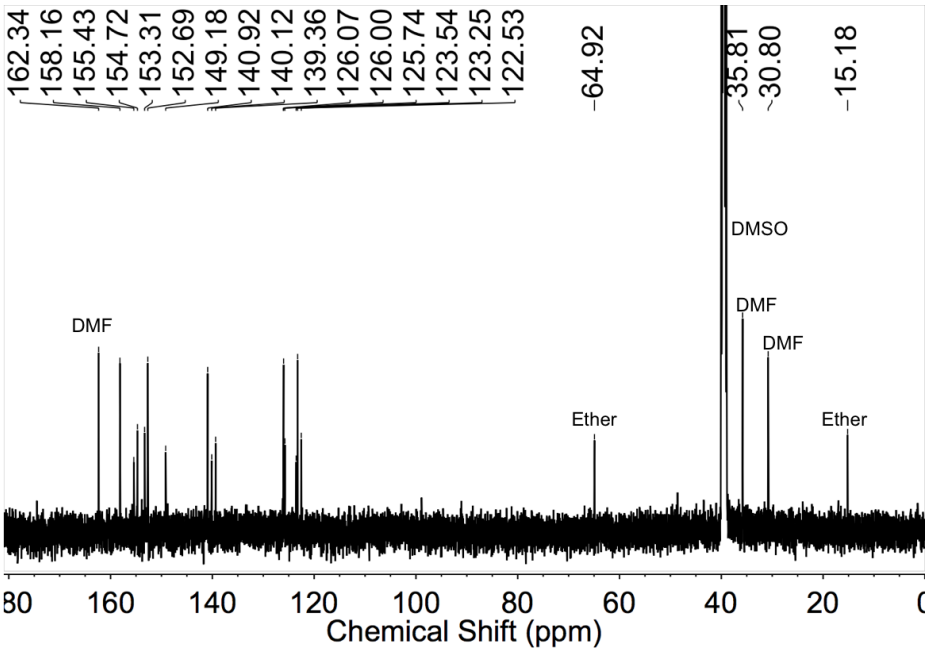

Figure B.5: $^{13}C\{^{1}H\}$ NMR of Compound **4.3** in DMSO-d_6.

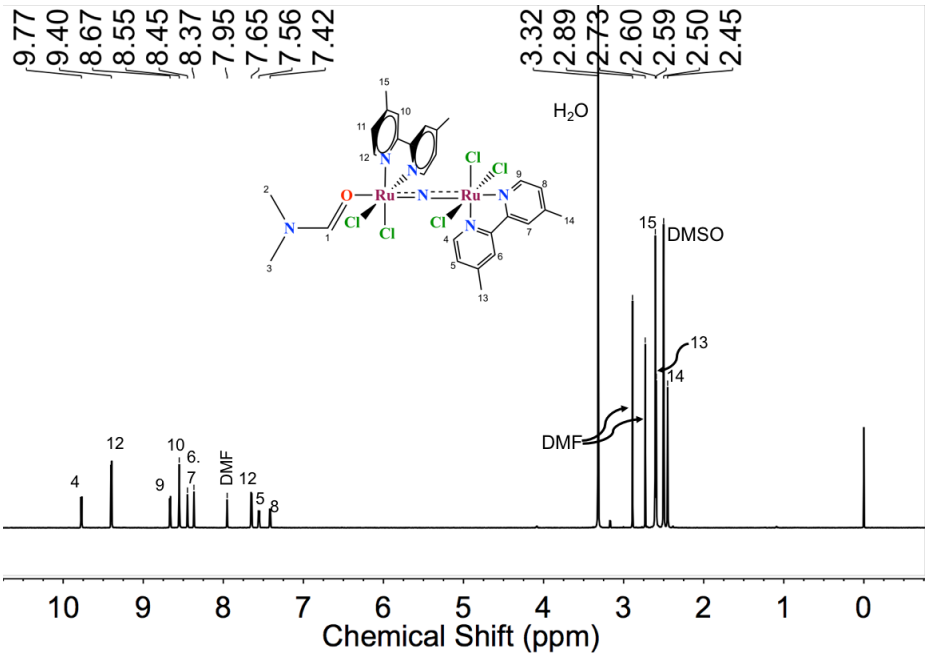

Figure B.6: ^{1}H NMR of Compound **4.4** in DMSO-d_6.

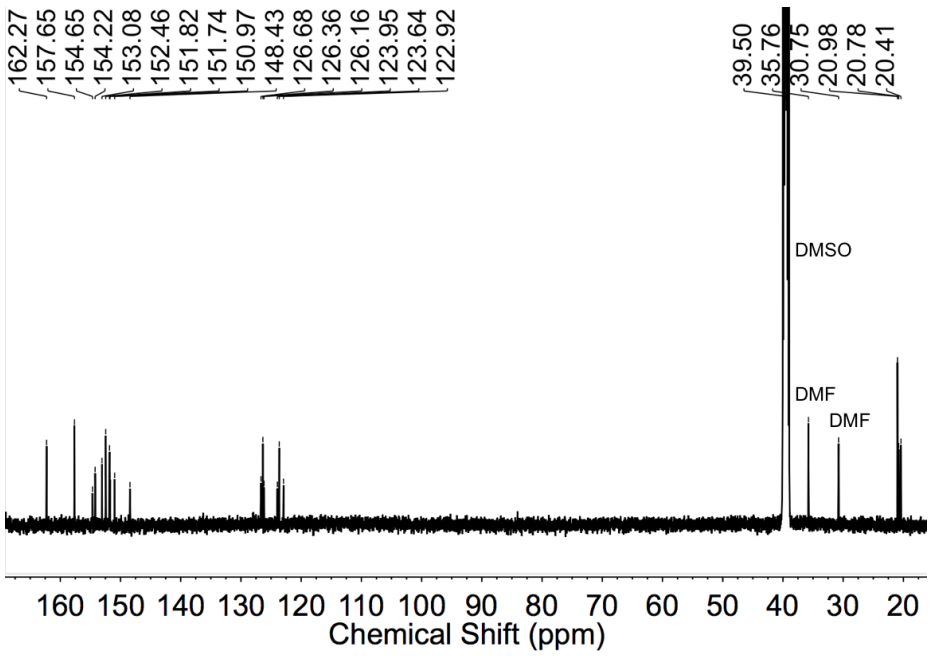

Figure B.7: $^{13}C\{^{1}H\}$ NMR of Compound **4.4** in DMSO-d_6.

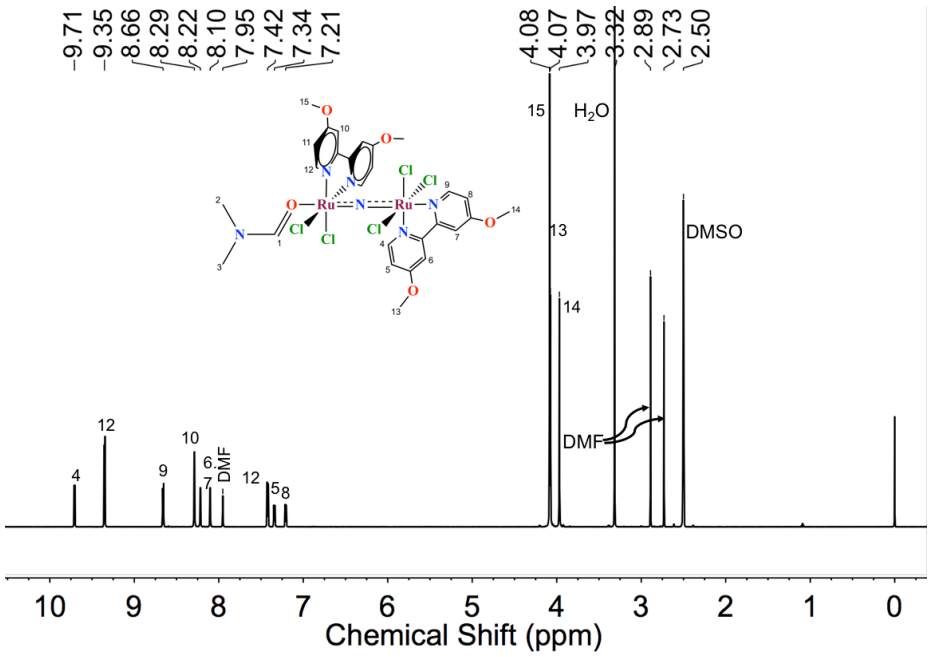

Figure B.8: ^{1}H NMR of Compound **4.5** in DMSO-d_6.

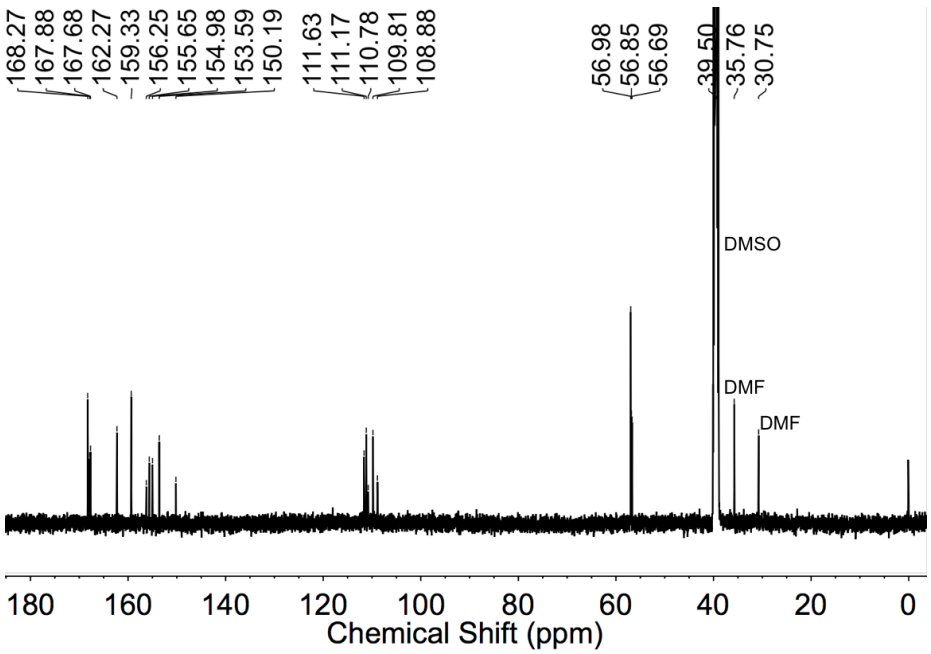

Figure B.9: $^{13}C\{^{1}H\}$ NMR of Compound **4.5** in DMSO-d_6.

APPENDIX C

EXPERIMENTAL DETAILS FOR BIOLOGICAL ASSAYS

C.1 Cell culture

HeLa (human cervical cancer) cells were grown as adherent monolayers in growth medium consisting of Dulbeccos Modified Eagle's Medium (DMEM) supplemented with 10% fetal bovine serum (FBS). The cultures were grown in 100 cm^2 petri dishes in an incubator at 37 °C with a humidified atmosphere composed of 5% CO_2. Cells were tested for mycoplasma contamination at least monthly with the PlasmoTest^{TM} Mycoplasma Detection Kit (InvivoGen).

C.2 Cell viability assays

Stock solutions of the complexes were prepared in H_2O ($[Cl_{10}Ru_2(\mu-O)]$, trans-$[(NH_3)_4Cl_2Ru]^+$, **4.SM2**, **3.1**, **4.1**, **4.2**) or DMSO (**4.3**, **4.4**, **4.5**) at concentrations between 2-3 mM. Cells were seeded in a 96-well plate at a density of about 2000 cells/well for HeLa cells and in a 6-well plate at a density of about 4000 cells/well for HEK293 cells. For Hela cells, after 24 hr, the growth medium was removed and replaced with 200 μL of growth medium containing varied concentrations of the complexes of interest. After an additional 72 hr incubation, the medium was removed and replaced with 200 μL of 5 mg/mL 3-(4,5-dimethylthiazol-2-yl)-2,5-diphenyltetrazolium bromide (MTT), diluted in serum-free medium. After 46 hr, the MTT was removed, and the resulting purple formazan crystals were dissolved in 200 μL DMSO containing 17% 0.1 M glycine and 0.1 M NaCl at pH 10.5. The absorbance at 570 nm in each well was determined using a BioTek Synergy HT plate reader. Six replicates per concentration level and at least three independent experiments

were completed for each compound. For HEK293 cells, after 24 hr the cells were dosed at 25 μM without removing the growth media. After an additional 72 hr incubation 400 μL of 5 mg/mL MTT was added. After 3-5 hr, the cells and MTT were removed, transferred to a 5 mL round-bottom tube and centrifuged for 10 minutes at 1000$\times$ (5310g). The supernatant was removed and the resulting purple formazan crystals were dissolved in 2 mL DMSO containing 17% 0.1 M glycine and 0.1 M NaCl at pH 10.5. Each sample was plated onto a 96-well place and the absorbance at 570 nm in each well was determined using a BioTek Synergy HT plate reader. Three replicates were completed for each compound.

C.3 Mitochondrial calcium uptake in permeabilized HeLa cells

HeLa (human cervical cancer) cells were amplified in 500 cm^2 petri dishes. Growth media was removed, and HeLa cells at 80-100% confluency were washed once with 1$\times$ PBS, incubated with 1 mM EDTA in 1$\times$ PBS for 10 minutes, and gently agitated to detach cells from the surface. Cells were centrifuged for 10 minutes at 1000$\times$ (5310g) and re-suspended in a pH 7.4 buffered glucose-containing salt solution (BGSS: 110 mM KCl, 1mM KH_2PO_4, 1mM $MgCl_2$, 20 mM HEPES, 5 mM sodium succinate, 30 μM EGTA, 1 mg/mL glucose) with a final cell density of 3.25 $\times$ 106 cells/mL. To permeabilize and track calcium uptake the cells, the suspension was stirred in a 1 cm pathlength acrylic cuvette at 37 C with 40 μM digitonin (DMSO) and 2 μM of Calcium Green 5N (Invitrogen, aqueous solution). A SLM 8100C steady-state fluorimeter (excitation=506 nm, emission=532 nm) was used to monitor the fluorescence of the Calcium Green 5N dye. Calcium (starting with 7.5 μM boluses) was added to test for mitochondrial calcium uptake inhibition. Compounds were added (5 μM), after two calcium boluses were added to the solution to verify cellular action after a stable emission intensity baseline was achieved. Alternatively the compounds can be incubated before adding calcium boluses if cellular action was verified using a previous cuvette.

C.4 Mitochondrial calcium uptake in isolated yeast mitochondria

Yeast mitochondria were reconstituted with the human components of the mitochondrial calcium uniporter MCU and EMRE as previously reported[366] in a yeast strain expressing a mitochondrial matrix-targeted aequorin as an indicator of Ca^{2+} concentration.[168,366] Approximately, 1 μg/well of isolated mitochondria was seeded into a white 96-well plate and incubated in the presence of compounds (aqueous solutions) at varied concentration levels for 5 min at room temperature. Ca^{2+}-stimulated light signal was recorded at 469 nm every 0.1 s with a luminescence counter (MicroBeta2 LumiJET Microplate Counter, PerkinElmer). Luminescence intensity was converted to calcium concentration as previously described.[367] Plots of normalized calcium concentration, versus concentration of ruthenium complex gave dose-response curves that were fit with the Hill Equation: $y = A + \frac{(B-A)x^n}{k^n+x^n}$.

BIBLIOGRAPHY

[1] J. J. M. Halls, C. A. Walsh, N. Greenham, E. A. Marseglia, R. Friend, S. C. Moratti, and A. Holmes, *Nature*, **1995**, *376*, 498–500.

[2] N. S. Sariciftci, L. Smilowitz, A. J. Heeger, and F. Wudl, *Science*, **1992**, *258*, 1474–1476.

[3] S. Günes, H. Neugebauer, and N. S. Sariciftci, *Chem. Rev.*, **2007**, *107*, 1324–1338.

[4] J. Benson-Smith, L. Goris, K. Vandewal, K. Haenen, J. Manca, D. Vanderzande, D. Bradley, and J. Nelson, *Adv. Funct. Mater.*, **2007**, *17*, 451–457.

[5] K. M. Coakley and M. D. McGehee, *Chem. Mater.*, **2004**, *16*, 4533–4542.

[6] A. C. Arias, J. D. MacKenzie, R. Stevenson, J. J. M. Halls, M. Inbasekaran, E. P. Woo, D. Richards, and R. H. Friend, *Macromolecules*, **2001**, *34*, 6005–6013.

[7] C. J. Brabec, N. S. Sariciftci, and J. C. Hummelen, *Adv. Funct. Mater.*, **2001**, *11*, 15–26.

[8] A. J. Ferguson, N. Kopidakis, S. E. Shaheen, and G. Rumbles, *J. Phys. Chem. C*, **2008**, *112*, 9865–9871.

[9] D. Veldman, Ö. Ípek, S. C. J. Meskers, J. Sweelssen, M. M. Koetse, S. C. Veenstra, J. M. Kroon, S. S. van Bavel, J. Loos, and R. A. J. Janssen, *J. Am. Chem. Soc.*, **2008**, *130*, 7721–7735.

[10] P. Peumans and S. R. Forrest, *Chem. Phys. Lett.*, **2004**, *398*, 27–31.

[11] G. Yu, J. Gao, J. C. Hummelen, F. Wudl, and A. J. Heeger, *Science*, **1995**, *270*, 1789–1791.

[12] C. W. Tang, *Appl. Phys. Lett.*, **1986**, *48*, 183–185.

[13] G. J. Hedley, A. Ruseckas, and I. D. W. Samuel, *Chem. Rev.*, **2017**, *117*, 796–837.

[14] M. A. Green, Y. Hishikawa, W. Warta, E. D. Dunlop, D. H. Levi, J. Hohl-Ebinger, and A. W. Ho-Baillie, *Prog. Photovoltaics Res. Appl.*, **2017**, *25*, 668–676.

[15] S. Mori, H. Oh-oka, H. Nakao, T. Gotanda, Y. Nakano, H. Jung, A. Iida, R. Hayase, N. Shida, M. Saito, K. Todori, T. Asakura, A. Matsui, and M. Hosoya, *MRS Proceedings*, **2015**, *1737*.

[16] T. J. Savenije, A. J. Ferguson, N. Kopidakis, and G. Rumbles, *J. Phys. Chem. C*, **2013**, *117*, 24085–24103.

[17] Y. Kim, S. Cook, S. M. Tuladhar, S. A. Choulis, J. Nelson, J. R. Durrant, D. D. C. Bradley, M. Giles, I. McCulloch, C.-S. Ha, and M. Ree, *Nat. Mater.*, **2006**, *5*, 197–203.

[18] K. Kim, J. Liu, M. A. G. Namboothiry, and D. L. Carroll, *Appl. Phys. Lett.*, **2007**, *90*, 163511.

[19] F. Padinger, R. Rittberger, and N. Sariciftci, *Adv. Funct. Mater.*, **2003**, *13*, 85–88.

[20] Y. Kim, S. A. Choulis, J. Nelson, D. D. C. Bradley, S. Cook, and J. R. Durrant, *J. Mater. Sci.*, **2005**, *40*, 1371–1376.

[21] J. Nakamura, K. Murata, and K. Takahashi, *Appl. Phys. Lett.*, **2005**, *87*, 132105.

[22] M. Al-Ibrahim, O. Ambacher, S. Sensfuss, and G. Gobsch, *Appl. Phys. Lett.*, **2005**, *86*, 201120.

[23] G. Li, V. Shrotriya, Y. Yao, and Y. Yang, *J. Appl. Phys.*, **2005**, *98*, 043704.

[24] R. Hiorns, R. deBettignies, J. Leroy, S. Bailly, M. Firon, C. Sentein, A. Khoukh, H. Preud'homme, and C. Dagron-Lartigau, *Adv. Funct. Mater.*, **2006**, *16*, 2263–2273.

[25] P. E. Keivanidis, T. M. Clarke, S. Lilliu, T. Agostinelli, J. E. Macdonald, J. R. Durrant, D. D. C. Bradley, and J. Nelson, *J. Phys. Chem. Lett.*, **2010**, *1*, 734–738.

[26] R. A. Marsh, J. M. Hodgkiss, S. Albert-Seifried, and R. H. Friend, *Nano Lett.*, **2010**, *10*, 923–930.

[27] T. M. Clarke and J. R. Durrant, *Chem. Rev.*, **2010**, *110*, 6736–6767.

[28] T. M. Clarke, A. M. Ballantyne, J. Nelson, D. D. C. Bradley, and J. R. Durrant, *Adv. Funct. Mater.*, **2008**, *18*, 4029–4035.

[29] M. Loi, S. Toffanin, M. Muccini, M. Forster, U. Scherf, and M. Scharber, *Adv. Funct. Mater.*, **2007**, *17*, 2111–2116.

[30] H. Ohkita, S. Cook, Y. Astuti, W. Duffy, S. Tierney, W. Zhang, M. Heeney, I. McCulloch, J. Nelson, D. D. C. Bradley, and J. R. Durrant, *J. Am. Chem. Soc.*, **2008**, *130*, 3030–3042.

[31] L. J. A. Koster, V. D. Mihailetchi, and P. W. M. Blom, *Appl. Phys. Lett.*, **2006**, *88*, 052104.

[32] P. Schilinsky, C. Waldauf, and C. J. Brabec, *Appl. Phys. Lett.*, **2002**, *81*, 3885–3887.

[33] A. J. Ferguson, N. Kopidakis, S. E. Shaheen, and G. Rumbles, *J. Phys. Chem. C*, **2011**, *115*, 23134–23148.

[34] J. Kirkpatrick, P. E. Keivanidis, A. Bruno, F. Ma, S. A. Haque, A. Yarstev, V. Sundstrom, and J. Nelson, *J. Phys. Chem. B*, **2011**, *115*, 15174–15180.

[35] A. M. Nardes, A. L. Ayzner, S. R. Hammond, A. J. Ferguson, B. J. Schwartz, and N. Kopidakis, *J. Phys. Chem. C*, **2012**, *116*, 7293–7305.

[36] S. D. Oosterhout, A. J. Ferguson, B. W. Larson, D. C. Olson, and N. Kopidakis, *J. Phys. Chem. C*, **2016**, *120*, 24597–24604.

[37] T. Offermans, P. A. van Hal, S. C. J. Meskers, M. M. Koetse, and R. A. J. Janssen, *Phys. Rev. B*, **2005**, *72*, 045213.

[38] S. H. Park, A. Roy, S. Beaupre, S. Cho, N. Coates, J. S. Moon, D. Moses, M. Leclerc, K. Lee, and A. J. Heeger, *Nat. Photon*, **2009**, *3*, 297–302.

[39] D. C. Coffey, B. W. Larson, A. W. Hains, J. B. Whitaker, N. Kopidakis, O. V. Boltalina, S. H. Strauss, and G. Rumbles, *J. Phys. Chem. C*, **2012**, *116*, 8916–8923.

[40] T. Clarke, A. Ballantyne, F. Jamieson, C. Brabec, J. Nelson, and J. Durrant, *Chem. Comm.*, **2008**, pp. 89–91.

[41] I. Hwang, D. Moses, and A. J. Heeger, *J. Phys. Chem. C*, **2008**, *112*, 4350–4354.

[42] M. Westerling, R. Österbacka, and H. Stubb, *Phys. Rev. B*, **2002**, *66*, 165220.

[43] R. Österbacka, C. P. An, X. M. Jiang, and Z. V. Vardeny, *Science*, **2000**, *287*, 839–842.

[44] W. L. Rance, A. J. Ferguson, T. McCarthy-Ward, M. Heeney, D. S. Ginley, D. C. Olson, G. Rumbles, and N. Kopidakis, *ACS Nano*, **2011**, *5*, 5635–5646.

[45] A. C. Morteani, P. Sreearunothai, L. M. Herz, R. H. Friend, and C. Silva, *Phys Rev Lett*, **2004**, *92*, 247402.

[46] C. Yin, T. Kietzke, D. Neher, and H.-H. Hörhold, *Appl. Phys. Lett.*, **2007**, *90*, 092117.

[47] A. C. Morteani, R. H. Friend, and C. Silva, *Chem. Phys. Lett.*, **2004**, *391*, 81–84.

[48] M. M. Alam and S. A. Jenekhe, *J. Phys. Chem. B*, **2001**, *105*, 2479–2482.

[49] J. C. Schlothauer, K. Grabmayer, G. M. Wallner, and B. Röder, *Prog. Photovolt: Res. Appl.*, **2016**, *24*, 855–870.

[50] E. J. Spadafora, R. Demadrille, B. Ratier, and B. Grevin, *Nano Lett.*, **2010**, *10*, 3337 – 3342.

[51] F. Wang, Q. Gao, K. Peng, Z. Li, Z. Li, Y. Guo, L. Fu, L. M. Smith, H. H. Tan, and C. Jagadish, *Nano Lett.*, **2015**, *15*, 3017–3023.

[52] C. Shen, H. Kampwerth, M. Green, T. Trupke, J. Carstensen, and A. Schütt, *Sol. Energy Mater Sol. Cells*, **2013**, *109*, 77–81.

[53] C. Shen, M. A. Green, O. Breitenstein, T. Trupke, M. Zhang, and H. Kampwerth, *Sol. Energy Mater Sol. Cells*, **2014**, *123*, 41–46.

[54] M. Glatthaar, J. Haunschild, R. Zeidler, M. Demant, J. Greulich, B. Michl, W. Warta, S. Rein, and R. Preu, *J. Appl. Phys.*, **2010**, *108*, 014501.

[55] T. Trupke, E. Pink, R. A. Bardos, and M. D. Abbott, *Appl. Phys. Lett.*, **2007**, *90*, 093506.

[56] T. J. Savenije, J. E. Kroeze, M. M. Wienk, J. M. Kroon, and J. M. Warman, *Phys. Rev. B*, **2004**, *69*, 155205.

[57] M. P. D. Haas and J. M. Warman, *Chem. Phys.*, **1982**, *73*, 35–53.

[58] Y. Martin, D. W. Abraham, and H. K. Wickramasinghe, *Appl. Phys. Lett.*, **1988**, *52*, 1103–1105.

[59] J. L. Luria, K. A. Schwarz, M. J. Jaquith, R. G. Hennig, and J. A. Marohn, *Adv. Mater.*, **2011**, *23*, 624–628.

[60] J. L. Luria, N. Hoepker, R. Bruce, A. R. Jacobs, C. Groves, and J. A. Marohn, *ACS Nano*, **2012**, *6*, 9392–9401.

[61] J. L. Luria *Spectroscopic Characterization of Charge Generation and Trapping in Third-Generation Solar Cell Materials Using Wavelength- and Time-Resolved Electric Force Microscopy.* PhD thesis, Cornell University, **2011**.

[62] L. M. Smieska, V. A. Pozdin, J. L. Luria, R. G. Hennig, M. A. Hines, C. A. Lewis, and J. A. Marohn, *Adv. Funct. Mater.*, **2012**, *22*, 5096–5106.

[63] M. Jaquith *The Kinetics Of Charge Trapping In Polycrystalline Pentacene And Ion Migration In Light Emitting Electrochemical Cells Studied By Time- And Temperature-resolved Electric Force Microscopy.* PhD thesis, Cornell University, **2008**.

[64] L. M. Smieska, Z. Li, D. Ley, A. B. Braunschweig, and J. A. Marohn, *Chem. Mater.*, **2016**, *28*, 813–820.

[65] M. Nonnenmacher, M. P. O'Boyle, and H. K. Wickramasinghe, *Appl. Phys. Lett.*, **1991**, *58*, 2921–2923.

[66] J. R. O'Dea, L. M. Brown, N. Hoepker, J. A. Marohn, and S. Sadewasser, *MRS Bull.*, **2012**, *37*, 642–650.

[67] J. J. Choi, J. Luria, B.-R. Hyun, A. C. Bartnik, L. Sun, Y.-F. Lim, J. A. Marohn, F. W. Wise, and T. Hanrath, *Nano Lett.*, **2010**, *10*, 1805–1811.

[68] D. C. Coffey and D. S. Ginger, *Nat. Mater.*, **2006**, *5*, 735–740.

[69] R. Giridharagopal, G. E. Rayermann, G. Shao, D. T. Moore, O. G. Reid, A. F. Tillack, D. J. Masiello, and D. S. Ginger, *Nano Lett.*, **2012**, *12*, 893–898.

[70] D. U. Karatay, J. S. Harrison, M. S. Glaz, R. Giridharagopal, and D. S. Ginger, *Rev. Sci. Instrum.*, **2016**, *87*, 053702.

[71] G. Shao, M. S. Glaz, F. Ma, H. Ju, and D. S. Ginger, *ACS Nano*, **2014**, *8*, 10799–0807.

[72] M. Takihara, T. Takahashi, and T. Ujihara, *Appl. Phys. Lett.*, **2008**, *93*, 021902.

[73] J. Murawski, T. Graupner, P. Milde, R. Raupach, U. Zerweck-Trogisch, and L. M. Eng, *J. Appl. Phys.*, **2015**, *118*, 154302.

[74] J. Murawski, T. Mönch, P. Milde, M. P. Hein, S. Nicht, U. Zerweck-Trogisch, and L. M. Eng, *J. Appl. Phys.*, **2015**, *118*, 244502.

[75] Z. Schumacher, Y. Miyahara, A. Spielhofer, and P. Grutter, *Phys. Rev. Appl.*, **2016**, *5*, 044018.

[76] R. P. Dwyer, S. R. Nathan, and J. A. Marohn, *Sci. Adv.*, **2017**, *3*, e1602951.

[77] N. Hoepker *Fluctuations near thin films of polymers, organic photovoltaics, and organic semiconductors probed by electric force microscopy.* PhD thesis, Cornell University, **2013**.

[78] O. Cherniavskaya, L. Chen, V. Weng, L. Yuditsky, and L. E. Brus, *J. Phys. Chem. B*, **2003**, *107*, 1525–1531.

[79] W. R. Silveira, E. M. Muller, T. N. Ng, D. Dunlap, and J. A. Marohn, in *Scanning Probe Microscopy: Electrical and Electromechanical Phenomena at the Nanoscale*, ed. S. Kalinin and A. Gruverman, Springer New York, New York, NY, 2007; pp. 788–830.

[80] B. Boashash, *Proc. IEEE*, **1992**, *80*, 520–538.

[81] S. M. Yazdanian, J. A. Marohn, and R. F. Loring, *J. Chem. Phys.*, **2008**, *128*, 224706.

[82] E. Moore *1. Mechanical Detection of Electron Spin Resonance from Nitroxide Spin Probes, 2. Ultrasensitive Cantilever Torque Magnetometry of Magnetization Switching in Individual Nickel Nanorods.* PhD thesis, Cornell University, **2012**.

[83] E. W. Moore, S. Lee, S. A. Hickman, S. J. Wright, L. E. Harrell, P. P. Borbat, J. H. Freed, and J. A. Marohn, *Proc. Natl. Acad. Sci.*, **2009**, *106*, 22251–22256.

[84] D. Rugar, H. Mamin, and P. Guethner, *Appl. Phys. Lett.*, **1989**, *55*, 2588–2590.

[85] D. De Stefani, R. Rizzuto, and T. Pozzan, *Annu. Rev. Biochem.*, **2016**, *85*, 161–192.

[86] M. Giacomello, I. Drago, P. Pizzo, and T. Pozzan, *Cell Death Differ.*, **2007**, *14*, 1267–1274.

[87] C. Mammucari, G. Gherardi, and R. Rizzuto, *Front. Oncol.*, **2017**, *7*, 139.

[88] M. R. Duchen, A. Verkhratsky, and S. Muallem, *Cell Calcium*, **2008**, *44*, 1–5.

[89] J. Danziger and M. L. Zeidel, *Clin. J. Am. Soc. Nephrol.*, **2015**, *10*, 852–862.

[90] A. E. Consolini, M. I. Ragone, P. Bonazzola, and G. A. Colareda in *Mitochondrial Dynamics in Cardiovascular Medicine;* Springer International Publishing, Cham, 2017; pp. 141–167.

[91] P. K. Hepler, *Plant Physiol.*, **2016**, *170*, 3–22.

[92] N. S. Orlov, A. E. Klimanova, M. A. Tverskoi, A. E. Vladychenskaya, V. L. Smolyaninova, and D. O. Lopina, *Molecules*, **2017**, *22*, H679–H691.

[93] N. S. Dhalla, *Arch. Int. Physiol. Biochim.*, **1969**, *77*, 916–934.

[94] J.-P. Decuypere, G. Monaco, G. Bultynck, L. Missiaen, H. De Smedt, and J. B. Parys, *Biochim. Biophys. Acta*, **2011**, *1813*, 1003–1013.

[95] P. Pinton, A. Romagnoli, R. Rizzuto, and C. Giorgi, *Curr. Mol. Med.*, **2008**, *8*, 119–130.

[96] N. Demaurex and C. Distelhorst, *Science*, **2003**, *300*, 65–67.

[97] M. J. Berridge, M. D. Bootman, and H. L. Roderick, *Nat. Rev. Mol. Cell Biol.*, **2003**, *4*, 517–529.

[98] A. Wiederkehr, G. Szanda, D. Akhmedov, C. Mataki, C. W. Heizmann, K. Schoonjans, T. Pozzan, A. Spät, and C. Wollheim, *Cell Metab.*, **2011**, *13*, 601–611.

[99] W. F. Graier, M. Frieden, and R. Malli, *Pflügers Arch.*, **2007**, *455*, 375–396.

[100] M. J. Berridge, P. Lipp, and M. D. Bootman, *Nat Rev Mol Cell Biol*, **2000**, *1*, 11–21.

[101] R. Malli and W. F. Graier, *FEBS Lett.*, **2010**, *584*, 1942–1947.

[102] S. S. Roy and G. Hajnóczky, *Methods*, **2008**, *46*, 213–223.

[103] G. Csordás, C. Renken, P. Varnai, L. Walter, D. Weaver, K. F. Buttle, T. Balla, C. A. Mannella, and G. Hajnóczky, *J. Cell Biol.*, **2006**, *174*, 915–921.

[104] P. Pinton, D. Ferrari, E. Rapizzi, F. D. Virgilio, T. Pozzan, and R. Rizzuto, *EMBO J.*, **2001**, *20*, 2690–2701.

[105] G. Csordás and G. Hajnóczky, *Cell Calcium*, **2001**, *29*, 249–262.

[106] L. Filippin, P. J. Magalhães, G. Di Benedetto, M. Colella, and T. Pozzan, *J. Biol. Chem.*, **2003**, *278*, 39224–39234.

[107] S. M. Davidson, D. Yellon, and M. R. Duchen in *Mitochondria: Practical Protocols;* Humana Press, Totowa, NJ, 2007; pp. 421–430.

[108] J. J. Lemasters, D. R. Trollinger, T. Qian, W. E. Cascio, and H. Ohata, *Methods in Enzymology*, **1999**, *302*, 341–358.

[109] A. Minta, J. P. Kao, and R. Y. Tsien, *J. Biol. Chem.*, **1989**, *264*, 8171–8178.

[110] T. Pozzan and R. Rudolf, *Biochim. Biophys. Acta*, **2009**, *1787*, 1317–1323.

[111] C. Jean-Quartier, A. I. Bondarenko, M. R. Alam, M. Trenker, M. Waldeck-Weiermair, R. Malli, and W. F. Graier, *Mol. Cell. Endocrinol.*, **2012**, *353*, 114–127.

[112] A. T. Deak, C. Jean-Quartier, A. I. Bondarenko, L. N. Groschner, R. Malli, W. F. Graier, and M. Waldeck-Weiermair in *Mitochondrial Medicine: Volume I, Probing Mitochondrial Function;* Springer New York, New York, NY, 2015; pp. 421–439.

[113] H. J. Knot, I. Laher, E. A. Sobie, S. Guatimosim, L. Gomez-Viquez, H. Hartmann, L.-S. Song, W. Lederer, W. F. Graier, R. Malli, M. Frieden, and O. H. Petersen, *Mol. Interv.*, **2005**, *5*, 112–127.

[114] D. R. Trollinger, W. E. Cascio, and J. J. Lemasters, *Biochem. Biophys. Res. Commun.*, **1997**, *236*, 738–742.

[115] E. Chacon, J. J. Lemasters, H. Ohata, I. S. Harper, D. R. Trollinger, and B. Herman, *FEBS Lett.*, **1996**, *382*, 31–36.

[116] I. Johnson, *The Molecular Probes Handbook: A Guide to Fluorescent Probes and Labeling Technologies*, Life Technologies Corporation, 11 ed., 2010.

[117] K. R. Gee, K. A. Brown, W. N. U. Chen, J. Bishop-Stewart, D. Gray, and I. Johnson, *Cell Calcium*, **2000**, *27*, 97–106.

[118] S. Rajdev and I. J. Reynolds, *Neurosci. Lett.*, **1993**, *162*, 149 – 152.

[119] M. A. Matlib, Z. Zhou, S. Knight, S. Ahmed, K. M. Choi, J. Krause-Bauer, R. Phillips, R. Altschuld, Y. Katsube, N. Sperelakis, and D. M. Bers, *J. Biol. Chem.*, **1998**, *273*, 10223–10231.

[120] M. Eberhard and P. Erne, *Biochem. Biophys. Res. Commun.*, **1991**, *180*, 209–215.

[121] O. Shimomura, F. H. Johnson, and Y. Saiga, *J. Cell. Comp. Physiol.*, **1962**, *59*, 223–239.

[122] J. G. Morin and J. W. Hastings, *J. Cell. Physiol.*, **1971**, *77*, 313–318.

[123] O. Shimomura, *J. Microsc.*, **2005**, *217*, 3–15.

[124] R. Rizzuto, A. W. M. Simpson, M. Brini, and T. Pozzan, *Nature*, **1992**, *358*, 325–327.

[125] R. Rizzuto, M. Brini, M. Murgia, and T. Pozzan, *Science*, **1993**, *262*, 744–747.

[126] J.-R. Martin, K. L. Rogers, C. Chagneau, and P. Brület, *PLoS One*, **2007**, *2*, e275.

[127] K. L. Rogers, S. Picaud, E. Roncali, R. Boisgard, C. Colasante, J. Stinnakre, B. Tavitian, and P. Brulet, *PLoS One*, **2007**, *2*, e974.

[128] M. Brini, P. Pinton, T. Pozzan, and R. Rizzuto, *Microsc. Res. Tech.*, **1999**, *46*, 380–389.

[129] O. Shimomura and F. H. Johnson, *Nature*, **1975**, *256*, 236–238.

[130] M. Montero, M. T. Alonso, E. Carnicero, I. Cuchillo-Ibáñez, A. Albillos, A. G. García, J. García-Sancho, and J. Alvarez, *Nat. Cell Biol.*, **1999**, *2*, 57–61.

[131] C. J. Bell, N. A. Bright, G. A. Rutter, and E. J. Griffiths, *J. Biol. Chem.*, **2006**, *281*, 28058–28067.

[132] M. Chalfie, Y. Tu, G. Euskirchen, W. W. Ward, and D. C. Prasher, *Science*, **1994**, *263*, 802–805.

[133] R. Rizzuto, M. Brini, P. Pizzo, M. Murgia, and T. Pozzan, *Curr. Biol.*, **1995**, *5*, 635–642.

[134] J. Zhang, R. E. Campbell, A. Y. Ting, and R. Y. Tsien, *Nat. Rev. Mol. Cell Biol.*, **2002**, *3*, 906–918.

[135] L. Filippin, M. C. Abad, S. Gastaldello, P. J. Magalhes, D. Sandona, and T. Pozzan, *Cell Calcium*, **2005**, *37*, 129–136.

[136] A. Miyawaki, J. Llopis, R. Heim, J. M. McCaffery, J. A. Adams, M. Ikura, and R. Y. Tsien, *Nature*, **1997**, *388*, 882–887.

[137] A. E. Palmer, C. Jin, J. C. Reed, and R. Y. Tsien, *Proc. Natl. Acad. Sci.*, **2004**, *101*, 17404–17409.

[138] M. Zaccolo, F. De Giorgi, C. Y. Cho, L. Feng, T. Knapp, P. A. Negulescu, S. S. Taylor, R. Y. Tsien, and T. Pozzan, *Nat. Cell Biol.*, **1999**, *2*, 25–29.

[139] V. O. Nikolaev, M. Bünemann, L. Hein, A. Hannawacker, and M. J. Lohse, *J. Biol. Chem.*, **2004**, *279*, 37215–37218.

[140] M. Sato, N. Hida, T. Ozawa, and Y. Umezawa, *Anal. Chem.*, **2000**, *72*, 5918–5924.

[141] A. Honda, S. R. Adams, C. L. Sawyer, V. Lev-Ram, R. Y. Tsien, and W. R. G. Dostmann, *Proc. Natl. Acad. Sci.*, **2001**, *98*, 2437–2442.

[142] T. Nagai, A. Sawano, E. S. Park, and A. Miyawaki, *Proc. Natl. Acad. Sci.*, **2001**, *98*, 3197–3202.

[143] G. S. Baird, D. A. Zacharias, and R. Y. Tsien, *Proc. Natl. Acad. Sci.*, **1999**, *96*, 11241–11246.

[144] W. A. Sather and E. W. McCleskey, *Annu. Rev. Physiol.*, **2003**, *65*, 133–159.

[145] G. C. Bompotis, S. Deftereos, C. Angelidis, E. Choidis, V. Panagopoulou, A. Kaoukis, V. P. Vassilikos, M. W. Cleman, and G. Giannopoulos, *Med. Chem.*, **2016**, *12*, 114–130.

[146] Y. Kirichok, G. Krapivinsky, and D. E. Clapham, *Nature*, **2004**, *427*, 360–364.

[147] G. Michels, I. F. Khan, J. Endres-Becker, D. Rottlaender, S. Herzig, A. Ruhparwar, T. Wahlers, and U. C. Hoppe, *Circulation*, **2009**, *119*, 2435–2443.

[148] R. Palty, E. Ohana, M. Hershfinkel, M. Volokita, V. Elgazar, O. Beharier, W. F. Silverman, M. Argaman, and I. Sekler, *J. Biol. Chem.*, **2004**, *279*, 25234–25240.

[149] L. Boyman, G. S. B. Williams, D. Khananshvili, I. Sekler, and W. J. Lederer, *J. Mol. Cell. Cardiol.*, **2013**, *59*, 205–213.

[150] R. Palty, W. F. Silverman, M. Hershfinkel, T. Caporale, S. L. Sensi, J. Parnis, C. Nolte, D. Fishman, V. Shoshan-Barmatz, S. Herrmann, D. Khananshvili, and I. Sekler, *Proc. Natl. Acad. Sci.*, **2010**, *107*, 436–441.

[151] E. Carafoli, R. Tiozzo, G. Lugli, F. Crovetti, and C. Kratzing, *J. Mol. Cell. Cardiol.*, **1974**, *6*, 361–371.

[152] M. Crompton, M. Capano, and E. Carafoli, *Eur. J. Biochem.*, **1976**, *69*, 453–462.

[153] M. Crompton, R. Moser, H. Ludi, and E. Carafoli, *Eur. J. Biochem.*, **1978**, *82*, 25–31.

[154] M. P. Blaustein and W. J. Lederer, *Physiol. Rev.*, **1999**, *79*, 763–854.

[155] M. D. Brand, *Biochem. J.*, **1985**, *229*, 161–166.

[156] K. Baysal, D. W. Jung, K. K. Gunter, T. E. Gunter, and G. P. Brierley, *Am. J. Physiol.*, **1994**, *266*, C800–C808.

[157] D. W. Jung, K. Baysal, and G. P. Brierley, *J. Biol. Chem.*, **1995**, *270*, 672–678.

[158] B. Kim and S. Matsuoka, *J. Physiol.*, **2008**, *586*, 1683–1697.

[159] H. Affolter and E. Carafoli, *Biochem. Biophys. Res. Commun.*, **1980**, *95*, 193–196.

[160] R. K. Dash and D. A. Beard, *J. Physiol.*, **2008**, *586*, 3267–3285.

[161] R. Palty and I. Sekler, *Cell Calcium*, **2012**, *52*, 9–15.

[162] D. M. Yellon and D. J. Hausenloy, *N. Engl. J. Med.*, **2007**, *357*, 1121–1135.

[163] P. E. Wolkowicz, L. H. Michael, R. M. Lewis, and J. McMillin-Wood, *Am. J. Physiol.*, **1983**, *244*, H644–H651.

[164] J. Liao, H. Li, W. Zeng, D. B. Sauer, R. Belmares, and Y. Jiang, *Science*, **2012**, *335*, 686–690.

[165] D. Khananshvili, *Ann. N.Y. Acad. Sci.*, **1991**, *639*, 85–95.

[166] T. E. Gunter and D. R. Pfeiffer, *Am. J. Physiol. Cell Physiol.*, **1990**, *258*, C755–C786.

[167] D. J. Pagliarini, S. E. Calvo, B. Chang, S. A. Sheth, S. B. Vafai, S. Ong, G. A. Walford, C. Sugiana, A. Boneh, W. K. Chen, D. E. Hill, M. Vidal, J. G. Evans, D. R. Thorburn, S. A. Carr, and V. K. Mootha, *Cell*, **2008**, *134*, 112–123.

[168] F. Perocchi, V. M. Gohil, H. S. Girgis, X. R. Bao, J. E. McCombs, A. E. Palmer, and V. K. Mootha, *Nature*, **2010**, *467*, 291–296.

[169] J. M. Baughman, F. Perocchi, H. S. Girgis, M. Plovanich, C. A. Belcher-Timme, Y. Sancak, X. R. Bao, L. Strittmatter, O. Goldberger, R. L. Bogorad, V. Koteliansky, and V. K. Mootha, *Nature*, **2011**, *476*, 341–345.

[170] D. De Stefani, A. Raffaello, E. Teardo, I. Szabo, and R. Rizzuto, *Nature*, **2011**, *476*, 336–340.

[171] M. Plovanich, R. L. Bogorad, Y. Sancak, K. J. Kamer, L. Strittmatter, A. A. Li, H. S. Girgis, S. Kuchimanchi, J. De Groot, L. Speciner, N. Taneja, J. OShea, V. Koteliansky, and V. K. Mootha, *PLoS One*, **2013**, *8*, e55785.

[172] D. Chaudhuri, Y. Sancak, V. K. Mootha, and D. E. Clapham, *eLife*, **2013**, *2*, e00704.

[173] A. Raffaello, D. De Stefani, D. Sabbadin, E. Teardo, G. Merli, A. Picard, V. Checchetto, S. Moro, I. Szabo, and R. Rizzuto, *EMBO J.*, **2013**, *32*, 2362–2376.

[174] Y. Sancak, A. L. Markhard, T. Kitami, E. Kovacs-Bogdan, K. J. Kamer, N. D. Udeshi, S. A. Carr, D. Chaudhuri, D. E. Clapham, A. A. Li, S. E. Calvo, O. Goldberger, and V. K. Mootha, *Science*, **2013**, *342*, 1379–1382.

[175] E. Kovacs-Bogdan, Y. Sancak, K. J. Kamer, M. Plovanich, A. Jambhekar, R. J. Huber, M. A. Myre, M. D. Blower, and V. K. Mootha, *Proc. Natl. Acad. Sci.*, **2014**, *111*, 8985–8990.

[176] L. Wang, X. Yang, S. Li, Z. Wang, Y. Liu, J. Feng, Y. Zhu, and Y. Shen, *EMBO J.*, **2014**, *33*, 594–604.

[177] N. Hoffman, H. Chandramoorthy, S. Shamugapriya, X. Zhang, S. Rajan, K. Mallilankaraman, R. Gandhirajan, R. Vagnozzi, L. Ferrer, K. Sreekrishnanilayam, K. Natarajaseenivasan, S. Vallem, T. Force, E. Choi, J. Cheung, and M. Madesh, *Cell Rep.*, **2013**, *5*, 1576–1588.

[178] G. Csordás, T. Golenár, E. Seifert, K. Kamer, Y. Sancak, F. Perocchi, C. Moffat, D. Weaver, S. Perez, R. Bogorad, V. Koteliansky, J. Adijanto, V. Mootha, and G. Hajnóczky, *Cell Metab.*, **2013**, *17*, 976–987.

[179] V. Hung, P. Zou, H.-W. Rhee, N. Udeshi, V. Cracan, T. Svinkina, S. Carr, V. Mootha, and A. Ting, *Mol. Cell*, **2014**, *55*, 332–341.

[180] K. J. Kamer and V. K. Mootha, *EMBO Rep.*, **2014**, *15*, 299–307.

[181] K. Mallilankaraman, P. Doonan, C. Cadenas, H. Chandramoorthy, M. Müller, R. Miller, N. E. Hoffman, R. K. Gandhirajan, J. Molgó, M. Birnbaum, B. Rothberg, D.-O. Mak, J. K. Foskett, and M. Madesh, *Cell*, **2012**, *151*, 630–644.

[182] M. Patron, V. Checchetto, A. Raffaello, E. Teardo, D. VecellioReane, M. Mantoan, V. Granatiero, I. Szabò, D. DeStefani, and R. Rizzuto, *Mol. Cell*, **2014**, *53*, 726–737.

[183] C. Tsai, Y. Wu, P. Pao, C. B. Phillips, C. Williams, C. Miller, M. Ranaghan, and M. Tsai, *Proc. Natl. Acad. Sci.*, **2017**, *114*, 4388–4393.

[184] T. König, S. Tröder, K. Bakka, A. Korwitz, R. Richter-Dennerlein, P. Lampe, M. Patron, M. Mühlmeister, S. Guerrero-Castillo, U. Brandt, T. Decker, I. Lauria, A. Paggio, R. Rizzuto, E. Rugarli, D. DeStefani, and T. Langer, *Mol. Cell*, **2016**, *64*, 148–162.

[185] D. M. Arduino, J. Wettmarshausen, H. Vais, P. Navas-Navarro, Y. Cheng, A. Leimpek, Z. Ma, A. Delrio-Lorenzo, A. Giordano, C. Garcia-Perez, G. Madard, B. Kuster, J. Garcia-Sancho, D. Mokranjac, J. K. Foskett, M. T. Alonso, and F. Perocchi, *Mol. Cell*, **2017**, *67*, 711–723.

[186] C. Cao, S. Wang, T. Cui, X. Su, and J. J. Chou, *Proc. Natl. Acad. Sci.*, **2017**, *114*, E2846–E2851.

[187] T. Yamamoto, R. Yamagoshi, K. Harada, M. Kawano, N. Minami, Y. Ido, K. Kuwahara, A. Fujita, M. Ozono, A. Watanabe, A. Yamada, H. Terada, and Y. Shinohara, *Biochim. Biophys. Acta*, **2016**, *1857*, 831–839.

[188] M. Colombini, *Biochim. Biophys. Acta*, **2016**, *1863*, 2498–2502.

[189] K. Oxenoid, Y. Dong, C. Cao, T. Cui, Y. Sancak, A. L. Markhard, Z. Grabarek, L. Kong, Z. Liu, B. Ouyang, Y. Cong, V. K. Mootha, and J. J. Chou, *Nature*, **2016**, *533*, 269–273.

[190] D. J. Hausenloy and D. M. Yellon, *J. Clin. Invest.*, **2013**, *123*, 92–100.

[191] G. Hajnóczky, G. Csordás, S. Das, C. Garcia-Perez, M. Saotome, S. Sinha Roy, and M. Yi, *Cell Calcium*, **2006**, *40*, 553–560.

[192] J. Kwong, X. Lu, R. Correll, J. Schwanekamp, R. Vagnozzi, M. A. Sargent, A. York, J. Zhang, D. Bers, and J. Molkentin, *Cell Reports*, **2015**, *12*, 15–22.

[193] Y. Oropeza-Almazán, E. Vázquez-Garza, H. Chapoy-Villanueva, G. Torre-Amione, and G. García-Riva, *Oxid. Med. Cell. Longev.*, **2017**, *2017*, 1–13.

[194] G. Margolis, E. Hertzberg-Bigelman, R. Levy, J. Ben-Shoshan, G. Keren, and M. Entin-Meer, *Cardiology*, **2016**, *134*, 57–64.

[195] H. M. Piper, D. Garcna-Dorado, and M. Ovize, *Cardiovasc. Res.*, **1998**, *38*, 291–300.

[196] E. C. Keeley, J. A. Boura, and C. L. Grines, *Lancet*, **2003**, *361*, 1304–1305.

[197] A. S. Manning and D. J. Hearse, *J. Mol. Cell. Cardiol.*, **1984**, *16*, 497–518.

[198] R. C. Kukreja and Y. Janin, *J. Thromb. Thrombolysis*, **1997**, *4*, 7–24.

[199] E. Braunwald and R. A. Kloner, *Circulation*, **1982**, *66*, 1146–1149.

[200] R. Bolli and E. Marban, *Physiol. Rev.*, **1999**, *79*, 609–634.

[201] F. V. de Werf, *Eur. Heart J.*, **2014**, *35*, 2510–2515.

[202] G. M. Frolich, P. Meier, S. K. White, D. M. Yellon, and D. J. Hausenloy, *Eur. Heart J.*, **2013**, *34*, 1714–1722.

[203] R. Ferrari, C. Balla, M. Malag, G. Guardigli, G. Morciano, M. Bertini, S. Biscaglia, and G. Campo, *Circ. J.*, **2017**, *81*, 131–141.

[204] S. M. Krause, W. E. Jacobus, and L. C. Becker, *Circ. Res.*, **1989**, *65*, 526–530.

[205] R. Bolli, B. S. Patel, M. O. Jeroudi, E. K. Lai, and P. B. McCay, *J. Clin. Invest.*, **1988**, *82*, 476–485.

[206] R. Ferrari, *Basic Res. Cardiol.*, **1995**, *90*, 300–302.

[207] A. Krug, W. D. M. D. Rochemont, and G. Korb, *Circ. Res.*, **1966**, *19*, 57–62.

[208] H. Ito, *Nat. Rev. Cardiol.*, **2006**, *3*, 499–506.

[209] H. Ito, A. Maruyama, K. Iwakura, S. Takiuchi, T. Masuyama, M. Hori, Y. Higashino, K. Fujii, and T. Minamino, *Circulation*, **1996**, *93*, 223–228.

[210] J. Ganame, G. Messalli, S. Dymarkowski, F. E. Rademakers, W. Desmet, F. Van de Werf, and J. Bogaert, *Eur. Heart J.*, **2009**, *30*, 1440–1449.

[211] J. Santo-Domingo, L. Vay, E. Hernandez-SanMiguel, C. D. Lobatan, A. Moreno, M. Montero, and J. Alvarez, *Br. J. Pharmacol.*, **2007**, *151*, 647–654.

[212] V. T. Thu, H.-K. Kim, L. T. Long, S.-R. Lee, T. M. Hanh, T. H. Ko, H.-J. Heo, N. Kim, S. H. Kim, K. S. Ko, B. D. Rhee, and J. Han, *Cardiovasc. Res.*, **2012**, *94*, 342–350.

[213] N. Kon, M. Murakoshi, A. Isobe, K. Kagechika, N. Miyoshi, and T. Nagayama, *Cell Death Discovery*, **2017**, *3*, 17045.

[214] J. Schwartz, E. Holmuhamedov, X. Zhang, G. L. Lovelace, C. D. Smith, and J. J. Lemasters, *Toxicol. Appl. Pharmacol.*, **2013**, *273*, 172–179.

[215] A. Degterev and A. Linkermann, *Cell. Mol. Life Sci.*, **2016**, *73*, 2251–2267.

[216] K. J. Kelly, T. A. Sutton, N. Weathered, N. Ray, E. J. Caldwell, Z. Plotkin, and P. C. Dagher, *Am. J. Physiol.*, **2004**, *287*, F760–F766.

[217] H. J. Kim, S. Y. Koo, B. Ahn, O. Park, D. H. Park, D. O. Seo, J. H. Won, H. J. Yim, H. Kwak, H. S. Park, C. W. Chung, Y. L. Oh, and S. H. Kim, *Arch. Pharmacal Res.*, **2010**, *33*, 1813–1823.

[218] B. M. Duggar, *Ann. N.Y. Acad. Sci.*, **1948**, *51*, 177–181.

[219] I. Chopra and M. Roberts, *Microbiol. Mol. Biol. Rev.*, **2001**, *65*, 232–260.

[220] P. W. Pires, C. T. Rogers, J. L. McClain, H. S. Garver, G. D. Fink, and A. M. Dorrance, *Am. J. Physiol.*, **2011**, *301*, H87–H97.

[221] S. X. Jiang, J. Lertvorachon, S. T. Hou, Y. Konishi, J. Webster, G. Mealing, E. Brunette, J. Tauskela, and E. Preston, *J. Biol. Chem.*, **2005**, *280*, 33811–33818.

[222] T. P. Theruvath, Z. Zhong, P. Pediaditakis, V. K. Ramshesh, R. T. Currin, A. Tikunov, E. Holmuhamedov, and J. J. Lemasters, *Hepatology*, **2008**, *47*, 236–246.

[223] S. R. Nathan, N. W. Pino, D. M. Arduino, F. Perocchi, S. N. MacMillan, and J. J. Wilson, *Inorg. Chem.*, **2017**, *56*, 3123–3126.

[224] K. C. Reed and F. L. Bygrave, *Biochem. J.*, **1974**, *140*, 143–155.

[225] F. Villani, F. Piccinini, A. Chiarra, and G. Brambilla, *Biochem. Pharmacol.*, **1975**, *24*, 1349–1351.

[226] M. Crompton and L. Andreeva, *Biochem. J.*, **1994**, *302*, 181–185.

[227] J. F. Unitt, K. L. Boden, A. V. Wallace, A. H. Ingall, M. E. Coombs, and F. Ince, *Bioorg. Med. Chem.*, **1999**, *7*, 1891–1896.

[228] J. H. Luft, *Anat. Rec.*, **1971**, *171*, 347–368.

[229] R. L. Karpel, M. S. Shirley, and S. R. Holt, *Biophys. Chem.*, **1981**, *13*, 151–165.

[230] J. M. Fletcher, B. F. Greenfield, C. J. Hardy, D. Scargill, and J. L. Woodhead, *J. Chem. Soc.*, **1961**, pp. 2000–2006.

[231] M. B. Robin and P. Day, *Adv. Inorg. Chem. Radiochem.*, **1968**, *10*, 247–422.

[232] M. de C.T. Carrondo, W. Griffith, J. Hall, and A. Skapski, *Biochim. Biophys. Acta*, **1980**, *627*, 332–334.

[233] J. Emerson, M. J. Clarke, W. L. Ying, and D. R. Sanadi, *J. Am. Chem. Soc.*, **1993**, *115*, 11799–11805.

[234] C. L. Moore, *Biochem. Biophys. Res. Commun.*, **1971**, *42*, 298–305.

[235] W. Bondareff, *J. Neurosurg.*, **1970**, *32*, 145–151.

[236] F. D. Vasington, P. Gazzotti, R. Tiozzo, and E. Carafoli, *Biochim. Biophys. Acta*, **1972**, *256*, 43–54.

[237] H. T. Taipale, R. A. Kaupplnen, and H. Komulainen, *Biochem. Pharmacol.*, **1989**, *38*, 1109–1113.

[238] M. C. Beatrice, D. L. Stiers, and D. R. Pfeiffer, *J. Biol. Chem.*, **1982**, *257*, 7161–7171.

[239] M. G. Hamilton and P. M. Lundy, *J. Pharmacol. Exp. Ther.*, **1995**, *273*, 940.

[240] I. Velasco, J. Moran, and R. Tapia, *Neurochem. Res.*, **1995**, *20*, 599–604.

[241] K. C. Reed and F. L. Bygrave, *FEBS Lett.*, **1974**, *46*, 109–114.

[242] K. Broekemeier, R. Krebsbach, and D. Pfeiffer, *Mol. Cell. Biochem.*, **1994**, *139*, 33–40.

[243] W. L. Ying, J. Emerson, M. J. Clarke, and D. R. Sanadi, *Biochemistry*, **1991**, *30*, 4949–4952.

[244] E. J. Griffiths, *FEBS Lett.*, **2000**, *486*, 257–260.

[245] G. Csordás, P. Varnai, T. Golenar, S. Sheu, and G. Hajnózky, *Mol. Cell. Endocrinol.*, **2012**, *353*, 109–113.

[246] S. Tang, X. Wang, Q. Shen, X. Yang, C. Yu, C. Cai, G. Cai, X. Meng, and F. Zou, *Biochem. Biophys. Res. Commun.*, **2015**, *458*, 186–193.

[247] A. N. Antony, M. Paillard, C. Moffat, E. Juskeviciute, J. Correnti, B. Bolon, E. Rubin, G. Csordás, E. L. Seifert, J. B. Hoek, and G. Hajnoczky, *Nat. Commun.*, **2016**, *7*, 1–10.

[248] Y. Liao, Y. Hao, H. Chen, Q. He, Z. Yuan, and J. Cheng, *Protein Cell*, **2015**, *6*, 434–442.

[249] R. Ferrari, F. di Lisa, R. Raddino, and O. Visioli, *J. Mol. Cell. Cardiol.*, **1982**, *14*, 737–740.

[250] V. M. Figueredo, K. P. Dresdner, Jr., A. C. Wolney, and A. M. Keller, *Cardiovasc. Res.*, **1991**, *25*, 337–342.

[251] Y. Park, D. K. Bowles, and J. P. Kehrer, *J. Pharmacol. Exp. Ther.*, **1990**, *253*, 628–635.

[252] A. Belous, C. Knox, I. B. Nicoud, J. Pierce, C. Anderson, C. Pinson, and R. S. Chari, *J. Surg. Res.*, **2003**, *111*, 284–289.

[253] N. Mewton, P. Croisille, G. Gahide, G. Rioufol, E. Bonnefoy, I. Sanchez, T. T. Cung, C. Sportouch, D. Angoulvant, G. Finet, X. André-Fouët, G. Derumeaux, C. Piot, H. Vernhet, D. Revel, and M. Ovize, *J. Am. Coll. Cardiol.*, **2010**, *55*, 1200–1205.

[254] C. Piot, P. Croisille, P. Staat, H. Thibault, G. Rioufol, N. Mewton, R. Elbelghiti, T. T. Cung, E. Bonnefoy, D. Angoulvant, C. Macia, F. Raczka, C. Sportouch, G. Gahide, G. Finet, X. André-Fouët, D. Revel, G. Kirkorian, J. Monassier, G. Derumeaux, and M. Ovize, *N. Engl. J. Med.*, **2008**, *359*, 473–481.

[255] Y. Abdallah, S. A. Kasseckert, W. Iraqi, M. Said, T. Shahzad, A. Erdogan, C. Neuhof, D. Gündüz, K. Schlüter, H. Tillmanns, H. M. Piper, H. P. Reusch, and Y. Ladilov, *J. Cell. Mol. Med.*, **2011**, *15*, 2478–2485.

[256] A. P. Halestrap, C. P. Connern, E. J. Griffiths, and P. M. Kerr, *Mol. Cell. Biochem.*, **1997**, *174*, 167–172.

[257] E. J. Griffiths and A. P. Halestrap, *J. Mol. Cell. Cardiol.*, **1993**, *25*, 1461–1469.

[258] N. Mewton, T. T. Cung, O. Morel, G. Cayla, E. Bonnefoy-Cudraz, G. Rioufol, D. Angoulvant, P. Guerin, M. Elbaz, N. Delarche, P. Coste, G. Vanzetto, M. Metge, J. Aupetit, B. Jouve, P. Motreff, C. Tron, J. Labeque, P. G. Steg, Y. Cottin, G. Range,

J. Clerc, P. Coussement, F. Prunier, F. Moulin, O. Roth, L. Belle, P. Dubois, P. Barragan, M. Gilard, C. Piot, P. Colin, M. Morice, J.-P. Monassier, O. Ider, J. L. P. Dubois-Rande, T. Unterseeh, H. Lebreton, T. Beard, D. Blanchard, G. Grollier, V. Malquarti, P. Staat, A. Sudre, M. J. Hansson, E. Elmer, I. Boussaha, C. Jossan, A. Torner, M. Claeys, D. Garcia-Dorado, and M. Ovize, *Am. Heart J.*, **2015**, *169*, 758–766.

[259] L. J. Motloch, S. Reda, M. Wolny, and U. C. Hoppe, *Pharmaceuticals*, **2015**, *8*, 474–482.

[260] G. de Jesus García-Rivas, A. Guerrero-Hernandez, G. Guerrero-Serna, J. S. Rodriguez-Zavala, and C. Zazueta, *FEBS J.*, **2005**, *272*, 3477–3488.

[261] G. de Jesus García-Rivas, K. Carvajal, F. Correa, and C. Zazueta, *Br. J. Pharmacol.*, **2006**, *149*, 829–837.

[262] A. Joly, *Compt. rend.*, **1892**, *115*, 1299.

[263] G. T. Morgan and F. H. Burstall, *J. Chem. Soc.*, **1936**, pp. 41–45.

[264] J. R. Campbell, R. J. H. Clark, W. P. Griffith, and J. P. Hall, *J. Chem. Soc., Dalton Trans.*, **1980**, *11*, 2228–2236.

[265] K. Gleu and W. Breuel, *Z. Anorg. Allg. Chem.*, **1938**, *237*, 350–358.

[266] C. Sterling, *Am. J. Bot.*, **1970**, *57*, 172–175.

[267] J. E. Earley, P. M. Smith, T. Fealey, and J. V. Silverton, *Inorg. Chem.*, **1971**, *10*, 1943–1947.

[268] A. M. Mathieson, D. P. Mellor, and N. C. Stephenson, *Acta Crystallogr.*, **1952**, *5*, 185–186.

[269] W. P. Griffith, *J. Chem. Soc. A*, **1969**, pp. 2270–2273.

[270] C. Clausen, R. Prados, and M. Good, *Inorg. and Nuc. Chem. Lett.*, **1971**, *7*, 485–489.

[271] F. E. Wagner, R. Wordel, W. P. Griffith, and N. T. McManus, *J. Chem. Soc., Dalton Trans.*, **1988**, pp. 1679–1682.

[272] S. A. Martynova, E. Y. Filatov, S. V. Korenev, N. V. Kuratieva, L. A. Sheludyakova, P. E. Plusnin, Y. V. Shubin, E. M. Slavinskaya, and A. I. Boronin, *J. Solid State Chem.*, **2014**, *212*, 42–47.

[273] J. D. Dunitz and L. E. Orgel, *J. Chem. Soc.*, **1953**, pp. 2594–2596.

[274] T. R. Weaver, T. J. Meyer, S. A. Adeyemi, G. M. Brown, R. P. Eckberg, W. E. Hatfield, E. C. Johnson, R. W. Murray, and D. Untereker, *J. Am. Chem. Soc.*, **1975**, *97*, 3039–3048.

[275] J. W. Jurss, J. J. Concepcion, J. M. Butler, K. M. Omberg, L. M. Baraldo, D. G. Thompson, E. L. Lebeau, B. Hornstein, J. R. Schoonover, H. Jude, J. D. Thompson, D. M. Dattelbaum, R. C. Rocha, J. L. Templeton, and T. J. Meyer, *Inorg. Chem.*, **2012**, *51*, 1345–1358.

[276] J. A. Baumann and T. J. Meyer, *Inorg. Chem.*, **1980**, *19*, 345–350.

[277] M. Yoshida, M. Kondo, T. Nakamura, K. Sakai, and S. Masaoka, *Angew. Chem. Int. Ed.*, **2014**, *53*, 11519–11523.

[278] J. S. Filippo, R. L. Grayson, and H. J. Sniadoch, *Inorg. Chem.*, **1976**, *15*, 269–274.

[279] R. J. H. Clark, M. L. Franks, and P. C. Turtle, *J. Am. Chem. Soc.*, **1977**, *99*, 2473–2480.

[280] J. R. Campbell and R. J. H. Clark, *J. Chem. Soc., Faraday Trans. 2*, **1980**, *76*, 1103–1118.

[281] D. E. Richardson and H. Taube, *Coord. Chem. Rev.*, **1984**, *60*, 107–129.

[282] H. J. Keller and K. E. Schwarzhans, *Angew. Chem. Int. Ed. Engl.*, **1970**, *9*, 196–205.

[283] N. S. Hush, A. Edgar, and J. K. Beattie, *Chem. Phys. Lett.*, **1980**, *69*, 128–133.

[284] Y. Lei and J. K. Hurst, *Inorg. Chem.*, **1994**, *33*, 4460–4467.

[285] J. A. Stull, R. D. Britt, J. L. McHale, F. J. Knorr, S. V. Lymar, and J. K. Hurst, *J. Am. Chem. Soc.*, **2012**, *134*, 19973–19976.

[286] J. A. Stull, T. A. Stich, J. K. Hurst, and R. D. Britt, *Inorg. Chem.*, **2013**, *52*, 4578–4586.

[287] B. S. Brunschwig, C. Creutz, and N. Sutin, *Chem. Soc. Rev.*, **2002**, *31*, 168–184.

[288] N. S. Hush in *Prog. Inorg. Chem.;* John Wiley & Sons, Inc., 1967; pp. 391–444.

[289] M. I. Webb and C. J. Walsby, *Metallomics*, **2013**, *5*, 1624–1633.

[290] A. Das, T. M. Scherer, S. M. Mobin, W. Kaim, and G. K. Lahiri, *Inorg. Chem.*, **2012**, *51*, 4390–4397.

[291] G. Metzker, I. de Aguiar, S. C. Martins, M. S. Schultz, L. C. Vasconcellos, and D. W. Franco, *Inorg. Chim. Act.*, **2014**, *416*, 142–146.

[292] M. J. Cleare and W. P. Griffith, *Chem. Comm.*, **1968**, pp. 1302–1302.

[293] M. J. Cleare and W. P. Griffith, *J. Chem. Soc. A*, **1970**, pp. 1117–1125.

[294] W. P. Griffith and D. Pawson, *J. Chem. Soc., Dalton Trans.*, **1973**, pp. 1315–1320.

[295] W. P. Griffith, N. T. McManus, and A. C. Skapski, *J. Chem. Soc. Chem. Commun.*, **1984**, pp. 434–435.

[296] W. P. Griffith, M. J. Mockfrod, and A. C. Skapski, *Inorg. Chim. Act.*, **1987**, *126*, 179–186.

[297] M. Haukka, T. Venäläinen, M. Ahlgren, and T. A. Pakkanen, *Inorg. Chem.*, **1995**, *34*, 2931–2936.

[298] M. Haukka, M. Ahlgren, and T. A. Pakkanen, *J. Chem. Soc., Dalton Trans.*, **1996**, pp. 1927–1933.

[299] D. Sellman, T. Gottschalk-Gaudig, and F. W. Heinemann, *Inorg. Chim. Acta*, **1998**, *269*, 63–72.

[300] T. Jüstel, J. Bendix, N. Metzler-Nolte, T. Weyhermller, B. Nuber, and K. Wieghardt, *Inorg. Chem.*, **1998**, *37*, 35–43.

[301] L. Bonomo, E. Solari, R. Scopelliti, and C. Floriani, *Angew. Chem. Int. Ed.*, **2001**, *40*, 2529–2531.

[302] S. Matsumura, K. Shikano, T. Oi, N. Suzuki, and H. Nagao, *Inorg. Chem.*, **2008**, *47*, 9125–9127.

[303] X. Yi, H. Ng, W. Cheung, H. H. Y. Sung, I. D. Williams, and W. Leung, *Inorg. Chem.*, **2012**, *51*, 10529–10535.

[304] H. Ng, W. Cheung, E. Kwan Huang, K. Wong, H. H. Y. Sung, I. D. Williams, and W. Leung, *Dalton Trans.*, **2015**, *44*, 18459–18468.

[305] W. Cheung, W. Chiu, M. de Vere-Tucker, H. H. Sung, I. D. Williams, and W. Leung, *Inorg. Chem.*, **2017**, *56*, 5680–5687.

[306] J. Durig, W. McAllister, J. Willis, and E. Mercer, *Spectrochim. Acta*, **1966**, *22*, 1091–1100.

[307] M. Mukaida, *Bull. Chem. Soc. Jpn.*, **1970**, *43*, 3805–3813.

[308] R. Zarhloul, R. Faure, and J. P. Deloume, *J. Crystallogr. Spectrosc. Res.*, **1992**, *22*, 601–606.

[309] M. Ciechanowicz and A. C. Skapski, *J. Chem. Soc. D*, **1969**, pp. 574–575.

[310] M. Ciechanowicz and A. C. Skapski, *J. Chem. Soc. A*, **1971**, pp. 1792–1794.

[311] E. E. Mercer, W. A. McAllister, and J. R. Durig, *Inorg. Chem.*, **1966**, *5*, 1881–1886.

[312] K. Sakai, M. Takeshita, Y. Tanaka, T. Ue, M. Yanagisawa, M. Kosaka, T. Tsubomura, M. Ato, and T. Nakano, *J. Am. Chem. Soc.*, **1998**, *120*, 11353–11363.

[313] J. J. Wilson and S. J. Lippard, *Polyhedron*, **2013**, *58*, 71–78.

[314] K. A. Jensen, *Inorg. Chem.*, **1970**, *9*, 1–5.

[315] P. C. Ford, D. P. Rudd, R. Gaunder, and H. Taube, *J. Am. Chem. Soc.*, **1968**, *90*, 1187–1194.

[316] M. L. Good, M. D. Patil, L. M. Trefonas, J. Dodge, C. J. Alexander, R. J. Majeste, and M. A. Cavanaugh, *J. Phys. Chem.*, **1984**, *88*, 483–488.

[317] C. A. Bessel, J. A. Margarucci, J. H. Acquaye, R. S. Rubino, J. Crandall, A. J. Jircitano, and K. J. Takeuchi, *Inorg. Chem.*, **1993**, *32*, 5779–5784.

[318] M. Hirahara, T. Hakamata, A. B. League, M. Z. Ertem, K. Takahashi, S. Nagai, K. Inaba, H. Yamazaki, K. Saito, T. Yui, C. J. Cramer, and M. Yagi, *Eur. J. Inorg. Chem.*, **2015**, *2015*, 3892–3903.

[319] R. D. Feltham and R. G. Hayter, *J. Chem. Soc.*, **1964**, pp. 4587–4591.

[320] R. A. Robinson and R. H. Stokes, *Electrolyte Solutions*, Butterworths, 2nd ed., 1965.

[321] J. A. Broomhead, F. Basolo, and R. G. Pearson, *Inorg. Chem.*, **1964**, *3*, 826–832.

[322] G. K. Gransbury, P. Kappen, C. J. Glover, J. N. Hughes, A. Levina, P. A. Lay, I. F. Musgrave, and H. H. Harris, *Metallomics*, **2016**, *8*, 762–773.

[323] L. Gu, X. Li, Q. Ran, C. Kang, C. Lee, and J. Shen, *Cancer Med*, **2016**, *5*, 2850–2860.

[324] A. Bergamo, T. Riedel, P. J. Dyson, and G. Sava, *Invest. New Drugs*, **2015**, *33*, 53–63.

[325] S. Leijen, S. A. Burgers, P. Baas, D. Pluim, M. Tibben, E. van Werkhoven, E. Alessio, G. Sava, J. H. Beijnen, and J. H. M. Schellens, *Invest. New Drugs*, **2015**, *33*, 201–214.

[326] R. Trondl, P. Heffeter, C. R. Kowol, M. A. Jakupec, W. Berger, and B. K. Keppler, *Chem. Sci.*, **2014**, *5*, 2925–2932.

[327] L. S. Flocke, R. Trondl, M. A. Jakupec, and B. K. Keppler, *Invest. New Drugs*, **2016**, *34*, 261–268.

[328] M. Cocchietto, S. Zorzet, A. Sorc, and G. Sava, *Invest. New Drugs*, **2003**, *21*, 55–62.

[329] G. Suss-Fink, *Dalton Trans.*, **2010**, *39*, 1673–1688.

[330] C. S. Allardyce, P. J. Dyson, D. J. Ellis, and S. L. Heath, *Chem. Commun.*, **2001**, pp. 1396–1397.

[331] W. Han Ang and P. J. Dyson, *Eur. J. Inorg. Chem.*, **2006**, *2006*, 4003–4018.

[332] P. J. Dyson, *Chimia*, **2007**, *61*, 698–703.

[333] S. J. Dougan and P. J. Sadler, *Chimia*, **2007**, *61*, 704–715.

[334] M. Miyamae, S. A. Camacho, M. W. Weiner, and V. M. Figueredo, *Am. J. Physiol.*, **1996**, *271*, H2145–H2153.

[335] T. Mosmann, *J. Immunol. Methods*, **1983**, *65*, 55–63.

[336] R. I. Freshney, *Culture of Animal Cells*, John Wiley & Sons, Inc., Hoboken, NJ, USA, 5th ed., 2005.

[337] S. Spreckelmeyer, C. Orvig, and A. Casini, *Molecules*, **2014**, *19*, 15584–15610.

[338] E. Alessio, *Eur. J. Inorg. Chem.*, **2017**, *2017*, 1549–1560.

[339] M. I. Webb and C. J. Walsby, *Dalton Trans.*, **2015**, *44*, 17482–17493.

[340] A. Levina, A. Mitra, and P. A. Lay, *Metallomics*, **2009**, *1*, 458–470.

[341] A. R. Timerbaev, C. G. Hartinger, S. S. Aleksenko, and B. K. Keppler, *Chem. Rev.*, **2006**, *106*, 2224–2248.

[342] C. G. Hartinger, W. H. Ang, A. Casini, L. Messori, B. K. Keppler, and P. J. Dyson, *J. Anal. At. Spectrom.*, **2007**, *22*, 960–967.

[343] S. W. Chang, A. R. Lewis, K. E. Prosser, J. R. Thompson, M. Gladkikh, M. B. Bally, J. J. Warren, and C. J. Walsby, *Inorg. Chem.*, **2016**, *55*, 4850–4863.

[344] M. L. Wallander, E. A. Leibold, and R. S. Eisenstein, *Biochim. Biophys. Acta*, **2006**, *1763*, 668–689.

[345] K. M. Mayle, A. M. Le, and D. T. Kamei, *Biochim. Biophys. Acta*, **2012**, *1820*, 264–281.

[346] M. Pongratz, P. Schluga, M. A. Jakupec, V. B. Arion, C. G. Hartinger, G. Allmaier, and B. K. Keppler, *J. Anal. At. Spectrom.*, **2004**, *19*, 46–51.

[347] D. R. Frasca, L. E. Gehrig, and M. J. Clarke, *J. Inorg. Biochem.*, **2001**, *83*, 139–149.

[348] A. Levina, J. B. Aitken, Y. Y. Gwee, Z. J. Lim, M. Liu, A. M. Singharay, P. F. Wong, and P. A. Lay, *Chem. Eur. J.*, **2013**, *19*, 3609–3619.

[349] M. I. Webb and C. J. Walsby, *Dalton Trans.*, **2011**, *40*, 1322–1331.

[350] N. Cetinbas, M. I. Webb, J. A. Dubland, and C. J. Walsby, *J. Biol. Inorg. Chem.*, **2010**, *15*, 131–145.

[351] L. Messori, F. Kratz, and E. Alessio, *Metal-Based Drugs*, **1996**, *3*, 1–9.

[352] A. Levina and P. A. Lay, *Inorg. Chem. Front.*, **2014**, *1*, 44–48.

[353] A. Bijelic, S. Theiner, B. K. Keppler, and A. Rompel, *J. Med. Chem.*, **2016**, *59*, 5894–5903.

[354] M. Henke, H. Richly, A. Drescher, M. Grubert, D. Alex, D. Thyssen, U. Jaehde, M. Scheulen, and R. Hilger, *Int. J. Clin. Pharmacol. Ther.*, **2009**, *47*, 58–60.

[355] W. Guo, W. Zheng, Q. Luo, X. Li, Y. Zhao, S. Xiong, and F. Wang, *Inorg. Chem.*, **2013**, *52*, 5328–5338.

[356] A. E. Egger, C. Rappel, M. A. Jakupec, C. G. Hartinger, P. Heffeter, and B. K. Keppler, *J. Anal. At. Spectrom.*, **2009**, *24*, 51–61.

[357] M. Groessl, O. Zava, and P. J. Dyson, *Metallomics*, **2011**, *3*, 591–599.

[358] C. A. Puckett, R. J. Ernst, and J. K. Barton, *Dalton Trans.*, **2010**, *39*, 1159–1170.

[359] M. Crul, H. J. G. D. van den Bongard, M. M. Tibben, O. van Tellingen, G. Sava, J. H. M. Schellens, and J. H. Beijnen, *Fresenius J. Anal. Chem.*, **2001**, *369*, 442–445.

[360] S. S. Aleksenko, *J. Anal. Chem.*, **2016**, *71*, 711–716.

[361] E. E. M. Brouwers, M. Tibben, H. Rosing, J. H. M. Schellens, and J. H. Beijnen, *Mass Spectrom. Rev.*, **2008**, *27*, 67–100.

[362] M. Sulyok, S. Hann, C. G. Hartinger, B. K. Keppler, G. Stingeder, and G. Koellensperger, *J. Anal. At. Spectrom.*, **2005**, *20*, 856–863.

[363] K. E. Prosser and C. J. Walsby, *Eur. J. Inorg. Chem.*, **2017**, *2017*, 1573–1585.

[364] A. N. Murphy, D. E. Bredesen, G. Cortopassi, E. Wang, and G. Fiskum, *Proc. Natl. Acad. Sci.*, **1996**, *93*, 9893–9898.

[365] S. E. Boggs, R. E. Clarke, and P. C. Ford, *Inorg. Chim. Act.*, **1996**, *247*, 129–130.

[366] D. W. Jung, P. C. Bradshaw, M. Litsky, and D. R. Pfeiffer, *Anal. Biochem.*, **2004**, *324*, 258–268.

[367] M. Bonora, C. Giorgi, A. Bononi, S. Marchi, S. Patergnani, A. Rimessi, R. Rizzuto, and P. Pinton, *Nat. Protocols*, **2013**, *8*, 2105–2118.

[368] K. Mallilankaraman, C. Cárdenas, P. J. Doonan, H. C. Chandramoorthy, K. M. Irrinki, T. Golenár, G. Csordás, P. Madireddi, J. Yang, M. Müller, R. Miller, J. E. Kolesar, J. Molgó, B. Kaufman, G. Hajnóczky, J. K. Foskett, and M. Madesh, *Nature Cell Biology*, **2012**, *14*, 1336.

[369] D. Chaudhuri and D. E. Clapham, *Biochem. Biophys. Res. Commun.*, **2014**, *449*, 367–369.

[370] A. D. Allen and C. V. Senoff, *Can. J. Chem.*, **1967**, *45*, 1337–1341.

[371] G. M. Sheldrick, *Acta Crystallogr. Sect. C Struct. Chem*, **2015**, *71*, 2–8.

[372] G. M. Sheldrick, *Acta Crystallogr. Sect. A Found. Crystallogr.*, **2008**, *64*, 112–122.

[373] P. Müller, *Crystallogr. Rev.*, **2009**, *15*, 57–83.

[374] A. L. Spek, *Acta Crystallogr. Sect. C Struct. Chem.*, **2015**, *71*, 9–18.

[375] N. G. Connelly and W. E. Geiger, *Chem. Rev.*, **1996**, *96*, 877–910.

[376] V. V. Pavlishchuk and A. W. Addison, *Inorg. Chim. Act.*, **2000**, *298*, 97–102.

[377] *CrysAlisPro*, Rigaku OD, The WoodLands, TX, 2015.

[378] APEX2, Bruker AXS Inc., Madison, Wisconsin, USA, 2012.

[379] O. V. Dolomanov, L. J. Bourhis, R. J. Gildea, J. A. K. Howard, and H. Puschmann, *J. Appl. Crystallogr.*, **2009**, *42*, 339–341.